

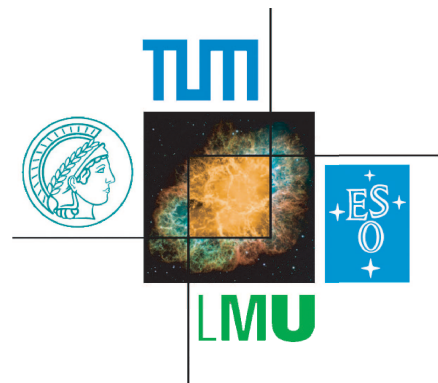
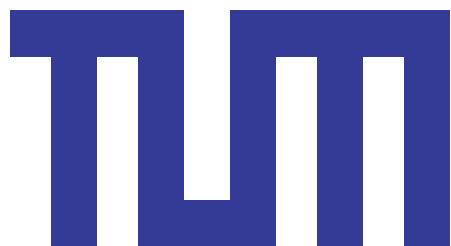
TECHNISCHE UNIVERSITÄT MÜNCHEN

Physik-Department E12 - Dense and strange hadronic matter

**The Production of  $K^0$  in p+p Reactions at 3.5 GeV**

**Inclusive and Exclusive Studies with the HADES Detector**

Jia-Chii Berger-Chen





# TECHNISCHE UNIVERSITÄT MÜNCHEN

Physik-Department E12 - Dense and strange hadronic matter

## The Production of $K^0$ in p+p Reactions at 3.5 GeV

—

### Inclusive and Exclusive Studies with the HADES Detector

Jia-Chii Berger-Chen

Vollständiger Abdruck der von der Fakultät für Physik der Technischen Universität München zur Erlangung des akademischen Grades eines

Doktors der Naturwissenschaften (Dr. rer. nat.)

genehmigten Dissertation.

Vorsitzende: Univ.-Prof. Dr. Nora Brambilla

Prüfer der Dissertation: 1. Univ.-Prof. Dr. Laura Fabbietti

2. Univ.-Prof. Dr. Elisa Resconi

Die Dissertation wurde am 19.03.2015 bei der Technischen Universität München eingereicht und durch die Fakultät für Physik am 09.04.2015 angenommen.



## Zusammenfassung

Eines der brennendsten Themen in der Physik gilt der Untersuchung der starken Wechselwirkung. Da die Vektorbosonen der starken Wechselwirkung (Gluonen) eine Farb-Antifarb-Kombination tragen, treten Effekte wie *Confinement* (*to confine* = einsperren) im niederen Energiebereich auf. Diese "eingesperrte" Hadronenphase kann mit dem HADES Aufbau [A<sup>+</sup>09] erforscht werden, der am GSI Helmholtzzentrum für Schwerionenforschung in Darmstadt stationiert ist. Versorgt durch das SIS18 Synchrotron kann die nukleare Zustandsgleichung bis zu Dichten von  $3\rho_0$  untersucht werden. Dabei betrifft eines der offenen Fragen das  $KN$  Potential, dessen repulsives Verhalten von mehreren Experimenten bestätigt wurde. Die beobachtete Stärke jedoch, ermittelt mit Hilfe von Transportmodellen, unterscheidet sich ( $U^{KN} = 20 - 40$  MeV) [B<sup>+</sup>04, B<sup>+</sup>09, A<sup>+</sup>10]. Folglich ist eine wiederholte Messung dieser Observablen und eine Validierung der Transporttheorien notwendig.

Zu diesem Zweck wurden p+p Daten, welche bei einer kinetischen Energie von 3,5 GeV aufgenommen wurden, analysiert, sowohl als Referenz für komplexere Systeme wie p+A und Schwerionenkollisionen als auch als Gegenprobe für Transportmodelle. In dieser Arbeit wird eine inklusive Analyse der  $K^0$  Ausbeute präsentiert, welche als Funktion von zwei-dimensionalen Observablen ( $p_t$ - $y_{cm}$  und  $p_{cm}$ - $\cos\Theta_{cm}$ ) ausgeführt wurde. Dadurch konnte eine modell-unabhängige Korrektur der HADES Akzeptanz und Effizienz und die ein-dimensionale Winkelverteilung  $dN/d\cos\Theta_{cm}$  gewonnen werden, welche eine leichte anisotrope  $K^0$  Produktion aufzeigt. Weiterhin konnte die Rapiditätsverteilung  $dN/dy_{cm}$  abgeleitet und der gesamte  $K^0$  Produktionsquerschnitt extrahiert werden ( $\sigma_{K^0}^{tot} = 113.5 \pm 2.7(stat)_{-10.2}^{+16.6}(sys) \mu b$ ). Der Vergleich der Transportmodelle (HSD [CB99], UrQMD [B<sup>+</sup>98] and GiBUU [B<sup>+</sup>12]) mit den Ergebnissen zeigte allerdings keine zufriedenstellende Übereinstimmung, weder in Bezug auf die Kinematik noch in Bezug auf die Ausbeute.

Da eines der Hauptbestandteile von Transportmodellen experimentelle Wirkungsquerschnitte sind, wurde ebenso eine exklusive  $K^0$  Analyse durchgeführt. Der p+p Datensatz ist dabei energetisch besonders gut geeignet, um die Relevanz von Resonanz- im Vergleich zu String-Fragmentierungs-Modellen zu beurteilen. Dazu wurden Reaktionen, welche Resonanzen zusammen mit einem  $K^0$  erzeugen ( $p + p \rightarrow K^0 + R + X$  mit  $R = \Delta(1232)^{++}$  oder  $\Sigma(1385)^+$ ), explizit mit einer Vierteilchen-Ereignisselektion ( $p, \pi^+, \pi^+$  und  $\pi^-$ ) ausgewählt. Dabei konnte jeder Kanalbeitrag zusammen mit dem Untergrundmodell bestimmt werden. Die Ergebnisse zeigen einen vorherrschenden Beitrag an resonanten  $\Delta^{++}$  Reaktionen, welcher 6-10 mal höher ist als der von den nicht-resonanten Äquivalenten. Außerdem konnte die Winkelverteilung der  $\Delta^{++}$  Produktion in dieser Analyse extrahiert werden.

Letztendlich konnten diese Erkenntnisse erfolgreich im GiBUU-Modell [B<sup>+</sup>12] implementiert werden, so dass die inklusiven  $K^0$  Spektren beschrieben wurden und es für die Bestimmung des  $KN$  Potentials in p+Nb Kollisionen bei der gleichen Strahlenergie verwendet werden konnte [A<sup>+</sup>14c]. Indem die übrigen unsicheren Modellparameter systematisch variiert wurden, war es möglich ein  $KN$  Potential von  $40 \pm 5$  MeV anzugeben. Darüber hinaus sind die extrahierten Ergebnisse auch für die zukünftigen Experimente von HADES und CBM an der FAIR Einrichtung in Darmstadt, die Messungen bei einer Strahlenenergie von 2-50 AGeV durchführen werden [F<sup>+</sup>11, FSS12], von essentieller Bedeutung.

## Abstract

One of the hot topics in physics is devoted to the study of strong interaction. Since the gauge bosons of the strong force (gluons) carry a combination of color–anti-color, effects such as color confinement prevail in the low-energy regime. This confined hadron phase can be explored by the HADES setup [A<sup>+</sup>09] located at the GSI Helmholtzzentrum für Schwerionenforschung in Darmstadt, Germany. Supplied by the SIS18 synchrotron it is possible to study the nuclear equation of state (EOS) up to densities of  $3\rho_0$ . One of the open questions is, thereby, related to the  $KN$  potential, whose repulsive behavior has been confirmed by several experiments. The observed strength, however, obtained with help of transport models differ ( $U^{KN} = 20 - 40$  MeV) [B<sup>+</sup>04, B<sup>+</sup>09, A<sup>+</sup>10]. As a consequence, a re-measurement of this observable and a validation of the transport theories is needed.

For this purpose, p+p data recorded at a kinetic beam energy of 3.5 GeV were analyzed as a reference for more complex systems like p+A and heavy ion collisions as well as for a cross-check of transport models. In this work an inclusive analysis of the  $K^0$  yield is presented, which was carried out as a function of two-dimensional observables ( $p_t$ - $y_{cm}$  and  $p_{cm}$ - $\cos\Theta_{cm}$ ). Thus, a model independent correction of the HADES acceptance and efficiency and the one-dimensional angular distribution  $dN/d\cos\Theta_{cm}$  could be retrieved, which shows a slight anisotropic  $K^0$  production. Furthermore, the rapidity density distribution  $dN/dy_{cm}$  could be deduced and the total  $K^0$  production yield could be extracted ( $\sigma_{K^0}^{tot} = 113.5 \pm 2.7(stat)_{-10.2}^{+16.6}(sys) \mu b$ ). The cross-check of the transport models (HSD [CB99], UrQMD [B<sup>+</sup>98] and GiBUU [B<sup>+</sup>12]) with the results, however, showed no satisfactory agreement both in terms of kinematics and yield.

Since one of the main ingredients of transport models are experimental cross sections, an exclusive  $K^0$  analysis was performed as well. The p+p dataset is, thereby, very good suited to evaluate the relevance of resonance compared to string fragmentation models. For this purpose, reactions producing resonances together with a  $K^0$  ( $p + p \rightarrow K^0 + R + X$  with  $R = \Delta(1232)^{++}$  or  $\Sigma(1385)^+$ ) were chosen explicitly by a four-particle event selection ( $p$ ,  $\pi^+$ ,  $\pi^+$  and  $\pi^-$ ). Thereby, each channel contribution could be determined together with the background model. The results show a predominant contribution of the resonant  $\Delta^{++}$  reactions, which is 6-10 times larger than that of the non-resonant equivalents. Moreover, the angular distributions of the  $\Delta^{++}$  production could be extracted in this analysis.

Finally, these findings were implemented successfully into the GiBUU model [B<sup>+</sup>12], so that the inclusive  $K^0$  spectra were reproduced and so that it could be used for the determination of the  $KN$  potential in p+Nb collisions at the same beam energy [A<sup>+</sup>14c]. By systematically varying the remaining uncertain parameters of the model, it was possible to state a  $KN$  potential of  $40 \pm 5$  MeV. These extracted results are, furthermore, of essential importance for future experiments of HADES and CBM at the FAIR facility in Darmstadt, Germany, which will perform measurements at beam energies of 2-50 AGeV [F<sup>+</sup>11, FSS12].

# Contents

<b>1</b>	<b>Introduction</b>	<b>1</b>
1.1	The Standard Model of Particle Physics . . . . .	1
1.2	Strong Interaction, QCD and EOS . . . . .	2
1.3	The Generation of Hadron Masses . . . . .	6
1.4	In-Medium Modification of Kaons . . . . .	8
1.4.1	Anti-Kaons in Matter - Experimental Observables . . . . .	9
1.4.2	Kaons in Matter - Experimental Observables . . . . .	11
1.5	The Role of Baryon Resonances in the Study of Kaons . . . . .	14
1.6	Transport Model Calculations . . . . .	15
<b>2</b>	<b>The HADES Experiment</b>	<b>21</b>
2.1	Detector Systems . . . . .	22
2.1.1	The Target . . . . .	22
2.1.2	The RICH Detector . . . . .	22
2.1.3	The Magnet . . . . .	23
2.1.4	The Multi-Wire-Drift Chambers . . . . .	24
2.1.5	The META System . . . . .	24
2.1.6	The Beam Detectors . . . . .	25
2.1.7	The Forward Wall . . . . .	26
2.1.8	Trigger and DAQ . . . . .	26
2.2	Particle Identification . . . . .	27
2.3	The p+p Beam Time . . . . .	30
2.3.1	Primary Vertex Calculation . . . . .	30
2.3.2	Beam Shift Studies . . . . .	32
2.3.3	Absolute Normalization . . . . .	34
2.4	Simulations . . . . .	34
2.4.1	Simulation Tools . . . . .	35
2.4.1.1	Pluto Event Generator . . . . .	35
2.4.1.2	HGeant . . . . .	36
2.4.1.3	SimDST . . . . .	36
2.4.2	The $K_S^0$ Pluto Cocktail . . . . .	37
<b>3</b>	<b>The Inclusive <math>K_S^0</math> production in p+p @ 3.5 GeV</b>	<b>43</b>
3.1	Analysis Procedure . . . . .	43
3.1.1	$K_S^0$ Reconstruction . . . . .	44
3.1.2	Acceptance and Efficiency Correction . . . . .	47
3.1.3	Systematical Uncertainties . . . . .	50

3.2	Results and Discussion . . . . .	51
3.2.1	$P_t$ - $y$ Distributions . . . . .	51
3.2.2	Rapidity Density Distribution . . . . .	52
3.2.3	Angular Distributions . . . . .	54
3.3	Self-Consistency Checks . . . . .	56
3.4	Comparison to the Pluto Cocktail . . . . .	58
3.5	Comparison to Transport Calculations . . . . .	60
3.5.1	Comparison to HSD . . . . .	60
3.5.2	Comparison to UrQMD . . . . .	62
3.5.3	Comparison to GiBUU . . . . .	62
3.6	Summary of the Inclusive $K_S^0$ Analysis . . . . .	67
<b>4</b>	<b>The Exclusive <math>K_S^0</math> production in p+p @ 3.5 GeV</b>	<b>69</b>
4.1	Analysis Procedure . . . . .	70
4.1.1	Event and Track Selection . . . . .	71
4.1.2	Missing Mass, Invariant Mass and Angular Distributions . . . . .	73
4.1.3	Background Determination . . . . .	76
4.1.4	Simulation Cocktail . . . . .	78
4.1.5	Angular Anisotropy . . . . .	82
4.2	Results and Discussion . . . . .	85
4.2.1	Exclusive Contributions . . . . .	85
4.2.2	Exclusive Cross Sections . . . . .	90
4.3	Implementation of the Exclusive Cross Sections in Models . . . . .	93
4.4	Summary of the Exclusive $K_S^0$ Analysis . . . . .	98
<b>5</b>	<b>Summary and Outlook</b>	<b>101</b>
<b>A</b>	<b>Appendix to the Particle Identification</b>	<b>107</b>
A.1	Energy Loss in TOF and TOFino . . . . .	107
A.2	Energy Loss in MDC with Pion Preselection in TOF . . . . .	108
	<b>Bibliography</b>	<b>109</b>
	<b>Danksagung</b>	<b>121</b>

# 1 Introduction

## 1.1 The Standard Model of Particle Physics

Up to the present date the standard model (SM) of particle physics has not been proven wrong. In fact its validity has been shown in a multitude of experiments. The standard model formulated in the 1970s predicted the fundamental spin  $\frac{1}{2}$  particles (fermions), from which all matter is made of, and describes the basic particle interactions known today. Hence, beside the six leptons, which can exist freely, six further elementary particles, namely the quarks, were found in bound systems, the hadrons. Hadrons either consist of three constituent quarks and are called baryons or of a quark–anti-quark–pair and are called mesons. However, only the lightest baryons (e.g. protons) are stable in the sense of having longer lifetimes than our solar system, all other hadrons decay within a shorter time. A detailed scheme showing all fermions with their properties (charge, color charge, mass and spin) is depicted in Figure 1.1.

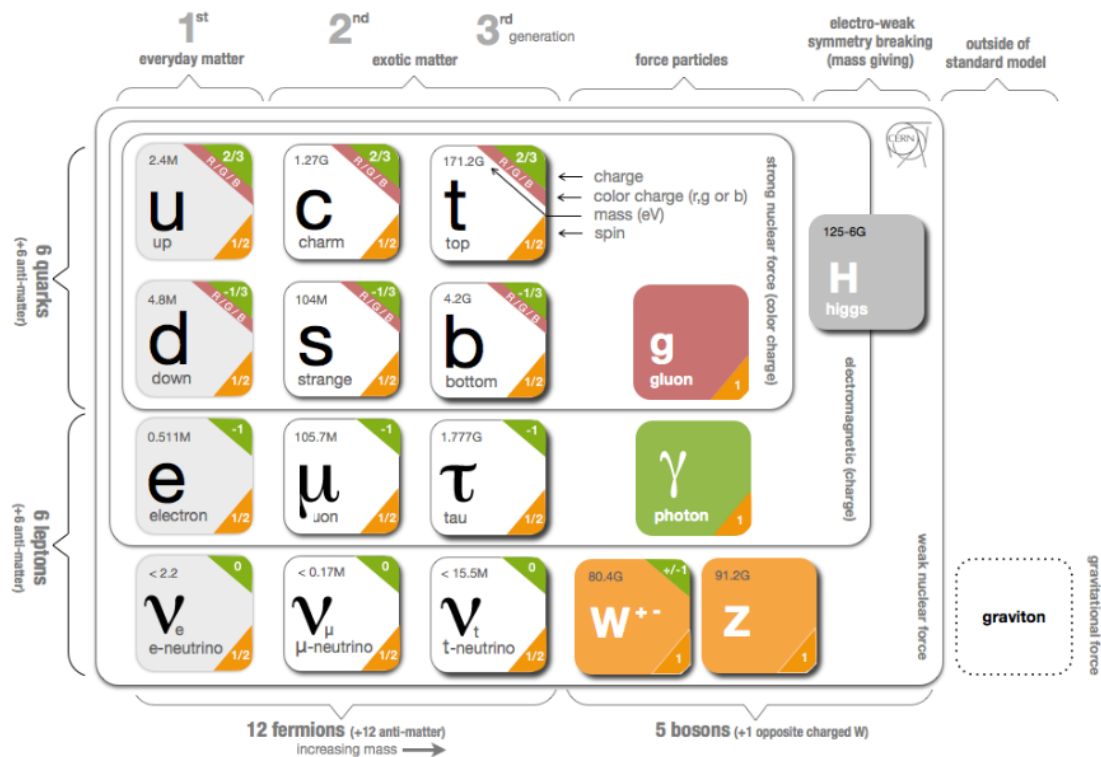


Figure 1.1: Diagram of the standard model particles taken from [isg14].

The standard model, furthermore, addresses the fundamental forces that act between the particles. These interactions are described by the exchange of gauge bosons, which are also illustrated in Figure 1.1. The probably best-known but at the same time least understood interaction is the gravitational force, which operates between all massive particles. Taking into account the mass range, with which particle physics deals with, gravitation is, however, the weakest interaction and can be neglected on the microscopic scale. The exchange boson is supposed to be a so-called graviton with spin 2, which has not yet been discovered experimentally. The second force, which comes along with the charge of the particles, is the electromagnetic interaction and is mediated by the exchange of photons. It is for example responsible for the bounding of electrons and nuclei or the intermolecular forces in liquids and solids. More important for this work is the strong interaction, which will be addressed in more detail in the next section. It is the force, which accounts for the binding of quarks within hadrons and of the protons and neutrons within nuclei. The strong force is mediated by the massless gluon. Finally, a fourth force is known, which is the so-called weak interaction. It is typically involved in the slow process of a nuclear  $\beta$ -decay and is described by the exchange of the rather heavy  $W^+$ ,  $W^-$  and  $Z^0$  bosons with masses in the order of 80-90 GeV/c<sup>2</sup>. Ultimately, it seems quite unsatisfying to have four forces or fields, which are completely independent from each other. That is why, studies are being carried out to find a more fundamental underlying theory, from which all four forces might originate.

## 1.2 Strong Interaction, QCD and EOS

The strong interaction introduced above has been successfully described by the theoretical framework of quantum chromodynamics (QCD), which is a non-abelian gauge theory with SU(3) symmetry. Similar like in quantum electrodynamics (QED), in which the charge defines a local symmetry, in QCD the color charge was introduced as internal degree of freedom as already implied by the word “chromo”. There are six types of color charges, whereby a quark carries one of the three primary colors (usually denoted as red, green and blue) and an anti-quark carries one of the three anti-colors. However, not only quarks hold color properties, but also the exchange bosons of the strong interaction, namely the gluons, which carry a combination of color–anti-color. This feature allows the gluons to self-interact and leads to effects such as color confinement and asymptotic freedom, which are reflected in the form of the QCD potential  $V_s(r)$ :

$$V_s(r) = -\frac{4}{3} \frac{\alpha_s(r)}{r} + kr \quad (1.1)$$

with

$\alpha_s$  : strong coupling constant

$r$  : distance between quark and anti-quark

$k \approx 1$  GeV/fm

The linear term  $kr$  is related to confinement and dominates at large distances equivalent to low-energy scales. Due to confinement quarks and gluons can never be observed as free particles in the normal environmental conditions. Instead, the strong force of the gluon-field increases with growing distances coupling the quarks together to confined objects of three quarks or quark–anti-quark pairs, the colorless hadrons. Hence, if a quark gets separated far enough from its bound system, at some point it will be energetically more favorable to generate a new quark–anti-quark pair than to put more energy into pulling the quark away and thus lead to spontaneous hadronization.

The first term of the quark–anti-quark potential (Eq. 1.1) is the relevant term at small distances and has the same  $\frac{\alpha}{r}$  behavior as the coulomb force. Small distances correspond to very high  $q^2$  (transfer momentum), where the energy dependent running coupling  $\alpha_s$  decreases drastically ( $\alpha_s \ll 1$ ). Therefore, the strong interaction becomes weak in this energy regime and the quarks might be even freed thus allowing theory to treat the QCD Lagrangian perturbatively with the quarks being the relevant degrees of freedom [Sch03]. Consequently, if going to very high temperatures or densities, one can think of a state, in which quarks and gluons are not bound in hadrons anymore, but move freely in a kind of plasma. Indeed, this phase is called a Quark-Gluon-Plasma (QGP).

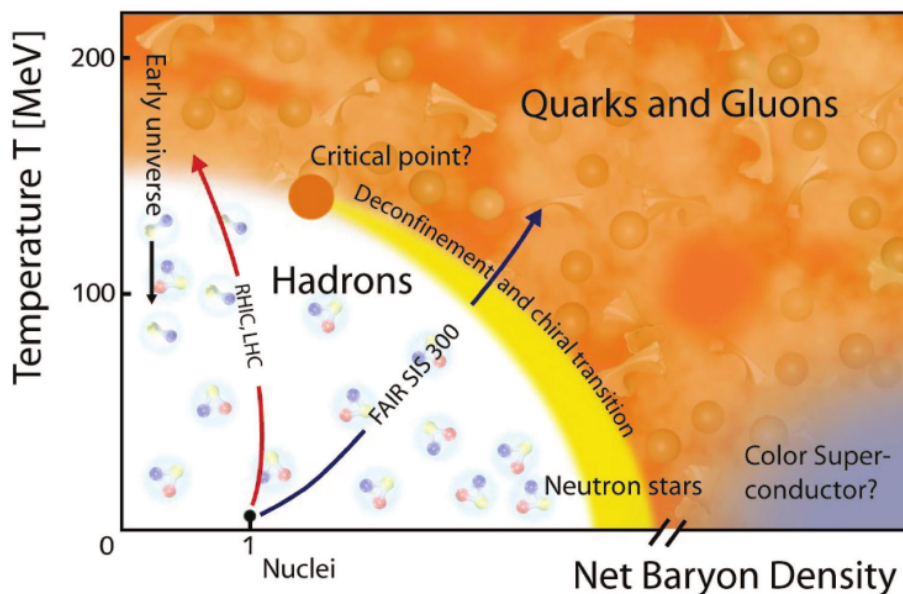


**Figure 1.2:** An example of the QCD phase diagram taken from [BCC11].

The phenomena described above can be summarized in a so-called QCD phase diagram, which is illustrated in Figure 1.2. The confined hadron phase can be found at low temperatures and rather low net baryon densities  $\mu_B$ , whereas a Quark-Gluon-Plasma will be located at high temperatures and densities. Theories predict a first order transition when moving from the hadron phase to the QGP at larger net baryon densities than at the critical point, while the needed temperature decreases with larger densities. At the critical point ( $T_c \approx 170$  MeV) a second order transition is expected. And when going to even lower densities

a smooth crossover should appear between the hadron gas and the Quark-Gluon-Plasma, which has been confirmed by lattice QCD calculations [Dan01, FH11, AEF<sup>+</sup>06].

In fact, this phase diagram is the outcome of the nuclear equation of state (EOS) implemented in the theory model, which for example connects parameters such as temperature  $T$ , pressure  $p$  and baryon density  $\rho$  with each other ( $p(\rho, T)$ ). The form of the EOS does not only depend on the properties of hadron interactions and defines the QCD phase diagram, but also explains the features of the early Universe ( $t \gtrsim 1 \mu\text{s}$  after the Big Bang), of supernovae explosions and of the stability of neutron stars [Dan01]. Therefore, the nuclear EOS connects different fields of physics putting their results into a global context. However, a lot of different EOS are on the market varying in their assumptions and so experimental input is in demand to constrain the EOS.

The EOS of the hadronic matter is rather well understood at normal nuclear density ( $\rho_0 = 0.16 \text{ fm}^{-3}$ ). At higher densities the properties are not so clear anymore, but can be experimentally investigated through heavy ion reactions, for example via the  $K^+$  yields measured at subthreshold energies in C+C and Au+Au collisions as it was done by the KAOS Collaboration in the beam energy range of 0.8 to 1.5 GeV per incoming nucleon [S<sup>+</sup>01]. Thereby, the correlation between the production mechanism of the kaons and the density reached in the heavy ion collision, which is dependent on the nuclear EOS, was exploited. This direct connection comes from the fact that the  $K^+$  at subthreshold energies can only be formed by secondary processes (e.g.  $\pi + N \rightarrow K^+ + A$ ), which probabilities enhance with increasing baryon densities [Fuc06, S<sup>+</sup>01]. In that study a rather soft EOS (high compressibility of the nuclear matter) was found to be compatible with the data in the studied density regions. Further heavy ion experiments probing the low temperature and high density sector ( $1-3\rho_0$ ) of the QCD phase diagram were carried out by the FOPI [Lei13] and the HADES Collaboration [Gal14], both located at the GSI Helmholtzzentrum für Schwerionenforschung (Darmstadt, Germany) and provided by the SIS18 synchrotron (1-2 AGeV). In couple of years a new facility, namely FAIR (Facility for Antiproton and Ion Research) with SIS100 and SIS300, will be available and allow measurements of the dense nuclear matter at higher temperatures as indicated in Figure 1.2. Even higher temperatures but less dense matter were and are studied at RHIC, the Relativistic Heavy Ion Collider in Brookhaven (U.S.), within the beam energy scan (BES) program ( $\sqrt{s_{NN}} = 7.7, 11.5, 19.6, 27, 39, 62.4, 130$  and  $200 \text{ GeV}$ ) with different colliding systems from U+U to p+p, which is a dedicated program to explore the strong interaction phase diagram searching for example for the softest point in the EOS equal to the first order transition and the critical point [Kum13, Sch13, Sah14, O'B13]. By analyzing various observables like the elliptic flow  $v_2$ , the chemical freeze out parameters ( $T_{ch}$  and  $\mu_B$ ), particle ratios and others it was found that at lower energies ( $\sqrt{s_{NN}} \leq 11.5 \text{ GeV}$ ) the system did not undergo phase transition [Kum13], whereas at higher energies ( $\sqrt{s_{NN}} \geq 11.5 \text{ GeV}$ ) evidence was seen for a QGP by studying the anisotropic flow and the nuclear modification factor  $R_{AA}$  of the  $\pi^0$  and of the  $J/\Psi$  [O'B13]. The region of very high energy densities equivalent to very high temperatures and nearly zero net baryon density can be studied at the Large Hadron Collider (LHC) at CERN to test perturbative QCD. Thereby, conditions like in the early Universe can be reached, where quarks and gluons are supposed to be in the deconfined QGP phase.

Various probes have been used to carry out this research such as heavy quarks, the formation of jets and quarkonia ( $J/\Psi$ ) suppression [DMR09, Mis13, Spo13, Shu14, Sco13, MS86].

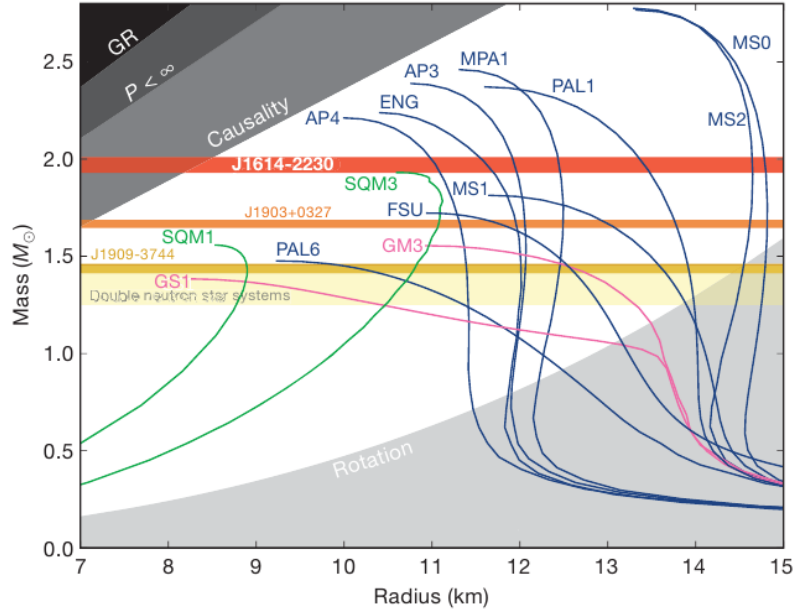


**Figure 1.3:** Relation of the neutron star mass and its radius taken from [DPR<sup>+</sup>10]. The colored lines are related to EOS including nucleons in blue, nucleons and exotic matter in pink and strange quark matter in green. The horizontal bands are mass constraints from measurements of neutron stars.

Not only is it possible to constrain the nuclear EOS by accelerator experiments but also by astrophysical observables like the neutron star. These extremely dense objects with densities of several times normal nuclear density ( $5\text{-}6\rho_0$  [SB08]) are not yet understood in detail including the possible composition of the inner core of a neutron star. A variety of EOS were discussed in the past years, which incorporate different assumptions on the interior of a neutron star. For example there are theories, that only consider nucleons, but also such, that operate with strange quark matter or exotic matter. Interesting for this work is the idea of a kaon condensate as one of the ingredients of the inner core next to protons, which are needed to neutralize the charge of the  $K^-$  mesons [LLB97], as it was already suggested by Kaplan and Nelson in 1986 [KN86, NK87]. Since then many investigations were driven in that direction. Thereby, a kaon condensate could form first of all due to the attractive  $K^-$  potential to nucleons increasing with density and secondly, when the kaon chemical potential  $\mu_K$  becomes equal to the electron and nucleon chemical potentials ( $\mu_K = \mu_e = \mu_p + \mu_n$ ) via the reactions  $n \leftrightarrow p + e^- + \bar{\nu}_e$  and  $n \leftrightarrow p + K^-$ . Depending on the model parameters, this situation typically sets in at a density of  $\approx 2\text{-}4\rho_0$  [LLB97, KK99, EKP95]. However, this hypothesis has begun to totter, since the EOS would be considerably softened and thus might not match the high mass neutron stars anymore, which have been recently discovered ( $1.97 \pm 0.04 M_\odot$  [DPR<sup>+</sup>10],  $2.01 \pm 0.04 M_\odot$  [AFW<sup>+</sup>13]). A bunch of EOS predicting a certain neutron star mass to radius relation

are plotted in Figure 1.3, in which the blue lines correspond to the theories using only nucleons, the pink lines to models with nucleons and exotic matter including hyperons and kaon condensates and the green lines to those with strange quark matter. The gray regions are forbidden due to various theoretical or observational limitations as the speed of light and others. Only those EOS crossing the horizontal bands, which indicate the mass measurements of neutron stars, in the white area are verified. That is not the case for the two shown models, which include exotic matter (GS1 and GM3). Nevertheless, some theoreticians claim that a soft EOS as measured in heavy ion reactions at  $1-3\rho_0$  might become stiff at higher densities and by that allow the involvement of strangeness at lower densities [SB08, WCSB12]. Also other concepts exist trying to bring together heavy ion measurements, theoretical calculations and the constraints by the observation of heavy neutron stars [MCS13, GA12]. However, for a more conclusive picture further investigations have to be made experimentally on the strange sector to understand better in-medium effects and the resulting modifications of hyperon and kaon interactions, which can be exhibited in theoretical models.

### 1.3 The Generation of Hadron Masses

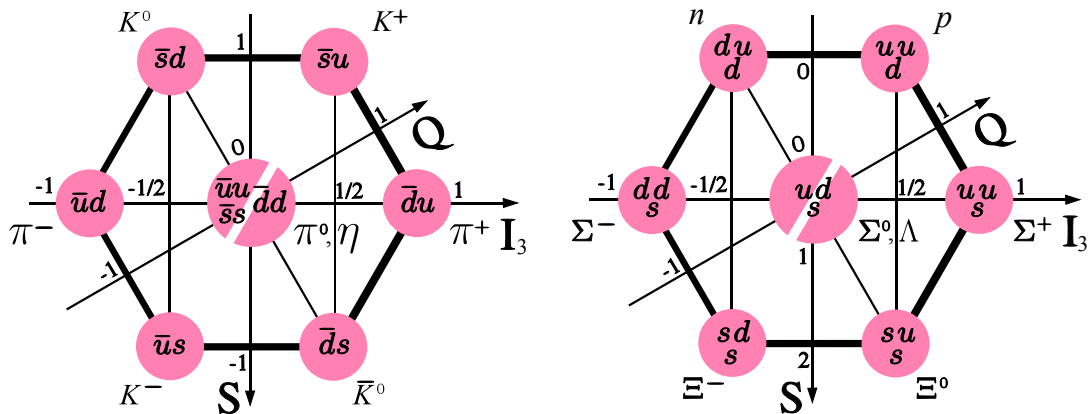


**Figure 1.4:** The octet of the pseudoscalar mesons with  $J^P = 0^-$  (left) and the baryon octet with  $J^P = 1/2^+$  (right) taken from [Wik14].

Thinking of the masses of the quarks one notices that they are very small compared to hadron masses. A proton of about  $938 \text{ MeV}/c^2$  for instance consists of one  $d$ -quark of only  $4.8 \text{ MeV}/c^2$  and two  $u$ -quarks with each only  $2.3 \text{ MeV}/c^2$  [O<sup>+</sup>14]. Thereby, one has to mention that the quark masses themselves and also those of the other fermions and of the gauge bosons  $W^+$ ,  $W^-$  and  $Z^0$  can be explained in the context of the recently discovered Higgs boson [A<sup>+</sup>12a, C<sup>+</sup>12] and the so-called Higgs mechanism incorporated in the standard model [Daw94]. The rest of the hadron mass can be derived for example in the framework of the chiral perturbation theory (ChPT), which is an effective field theory of QCD with the hadrons treated as the relevant degrees of freedom. A simple perturbation theory is not applicable in these low-energy regimes due to the large strong

coupling constant  $\alpha_s$ . Besides the local  $SU(3)_{color}$  symmetry, the ChPT exhibits other global symmetries like the  $U(1)$  symmetry, that yields the conservation of baryon numbers [Sch03]. The basic symmetry in ChPT is, however, the symmetry of  $SU(3)_L \times SU(3)_R$  in the chiral limit, when the quark masses (u, d and s) go to zero, and is responsible for the conservation of the handedness (= chirality) of left- and right-handed hadrons in strong interaction processes. This symmetry is spontaneously broken and dynamically generates the eight massless Nambu-Goldstone bosons [Nam09], which are associated to the octet of pseudoscalar mesons ( $K$ ,  $\pi$ ,  $\eta$ ) depicted in Figure 1.4 on the left, and leads to an absence of parity doublets [RW00]. The finite masses of the hadrons and their divergency originate in a so-called explicit symmetry breaking of the chirality on the quantum level, when loops are taken into account, and thus is a consequence of the finite masses of the quarks [Sch03, Bor05].

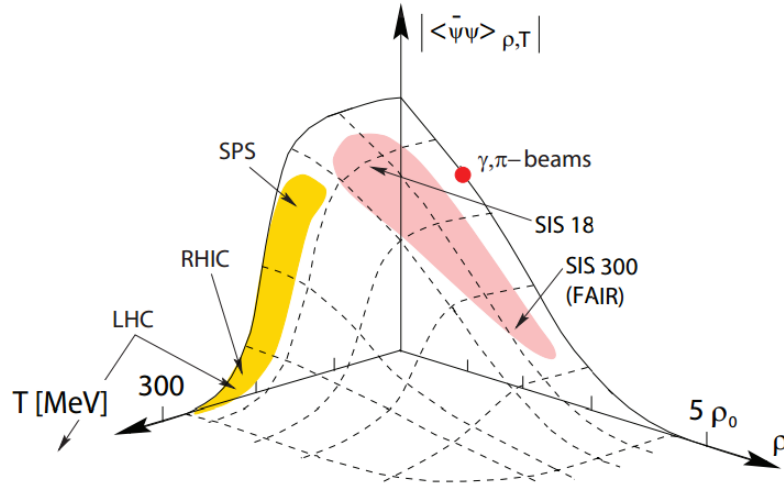


**Figure 1.5:** Expectation value of the chiral condensate plotted against temperature  $T$  and nuclear density  $\rho$  as calculated with the Nambu-Jona-Lasinio model [KLW90]. Indicated are the experimentally accessible regions by various accelerators. Figure taken from [Dah08].

Through the Gell-Mann–Oakes–Renner relation (GOR) for the pion case [GMOR68, Koc95]:

$$m_\pi^2 f_\pi^2 = -\frac{m_u + m_d}{2} \langle 0 | \bar{u}u + \bar{d}d | 0 \rangle \quad (1.2)$$

with

$m_\pi$  : mass of the pion

$f_\pi$  : pion decay constant

$m_u$  and  $m_d$  : masses of the current quarks u and d

$\langle 0 | \bar{u}u + \bar{d}d | 0 \rangle$  : quark condensate

one can find the connection of the pion mass, the pion decay constant  $f_\pi$  and the quark condensate  $\langle q\bar{q} \rangle$ , where the latter two can be seen as the order parameters of the spontaneous

symmetry breakdown. However, only few model independent calculations are available for the in-medium changes of  $f_\pi$  [F<sup>+</sup>11]. More widely-used is the scalar quark condensate  $\langle q\bar{q} \rangle$ , which has a non-vanishing vacuum expectation value and thus implies the presence of a spontaneous broken symmetry. The quark condensate or chiral condensate decreases with growing temperature and density, which is often related to a restoration of chiral symmetry and a significant change of hadron mass spectra [BR91, RW00, Fuc06]. Nevertheless, one has to keep in mind that although a vanished quark condensate is a necessary requirement for a restored chiral symmetry, at the same time chiral symmetry can still be partially broken [F<sup>+</sup>11, Bir96]. The development of this expectation value with temperature and nuclear density was for example calculated with the Nambu-Jona-Lasinio model [KLW90] and is illustrated in Figure 1.5. The experimentally accessible regions by the various accelerators are depicted as well and so one can find that already at SIS18 energies the quark condensate has dropped by up to 80% leading to the presence of modified hadron properties.

## 1.4 In-Medium Modification of Kaons

Since the presented work deals mainly with kaon production, this section is focused on the in-medium properties of these Goldstone bosons. As explained above, their mass of around 500 MeV/c<sup>2</sup> is generated through the explicit breaking of the chiral symmetry. In the vacuum these mesons are degenerated and differ only in their strangeness content, whereby kaons have  $S = 1$  and anti-kaons  $S = -1$ . In nuclear matter kaons split into  $K^+$  and  $K^0$  and anti-kaons into  $K^-$  and  $\bar{K}^0$  and therefore are additionally distinguishable through their charge, isospin and mass [Fuc06].

The interaction of kaons with the nuclear medium can be treated in the framework of the ChPT, which was first performed by Kaplan and Nelson [KN86, NK87]. As mentioned above, the degrees of freedom in the chiral Lagrangian are not anymore the fermions, but the baryon octet and the pseudoscalar meson octet depicted in Figure 1.4. For the study of kaon properties, this Lagrangian can be reduced to an effective chiral kaon-nucleon Lagrangian [Fuc06, HOL<sup>+</sup>12, LLB97], which reads as follows:

$$\begin{aligned} \mathcal{L} = & \bar{N}(i\gamma^\mu\partial_\mu - m_N)N + \partial^\mu\bar{K}\partial_\mu K - \left(m_K^2 - \frac{\Sigma_{KN}}{f_\pi^2}\bar{N}N\right)\bar{K}K \\ & - \frac{3i}{8f_\pi^2}\bar{N}\gamma^\mu N\bar{K}\overset{\leftrightarrow}{\partial}_\mu K \end{aligned} \quad (1.3)$$

with

- $N$  and  $K$  : nucleon and kaon field
- $m_N$  and  $m_K$  : nucleon and kaon mass
- $\Sigma_{KN}$  : kaon-nucleon sigma term
- $f_\pi$  : pion decay constant

This Lagrangian includes the Weinberg-Tomozawa term, which is attractive for anti-kaons and repulsive for kaons, and the scalar interaction, also called Kaplan-Nelson term, which is equal for the two types of kaons, but depends on the strength of the kaon-nucleon sigma term  $\Sigma_{KN}$ . The latter term  $\Sigma_{KN}$ , that is related to the strangeness content of the nucleon, is, however, only loosely fixed and can vary within 300 MeV and 450 MeV depending on the calculation model. By applying the above Lagrangian in the mean field approximation, it is possible to deduce the kaon energy in the medium [Fuc06, HOL<sup>+</sup>12, LLB97]:

$$E(\vec{k}, \rho_N) = \left[ m_K^2 + \vec{k}^2 - \frac{\Sigma_{KN}}{f_K^2} \rho_S + \left( \frac{3 \rho_N}{8 f_K^2} \right)^2 \right]^{1/2} \pm \frac{3 \rho_N}{8 f_K^2} \quad (1.4)$$

with

$m_K$  : kaon mass

$\vec{k}$  : three-momentum of the kaon

$\Sigma_{KN}$  : kaon-nucleon sigma term

$f_k$  : kaon decay constant

$\rho_S$  and  $\rho_N$  : scalar and nuclear density

Here, the upper sign in front of the last term is related to kaons, whereas the lower negative sign is to anti-kaons. As mentioned above, this so-called Weinberg-Tomozawa term is the origin for the opposite behavior of kaons and anti-kaons in medium. As a consequence of the repulsive or attractive kaon-nucleon (KN) potential the effective energy of the kaon or anti-kaon increases or decreases, which can be interpreted as a mass shift either to higher masses or to lower masses, respectively. For this very reason Kaplan and Nelson [KN86, NK87] came up with the idea of a possible kaon condensate within very dense objects like neutron stars. Due to the dropping anti-kaon mass with increasing nuclear density  $K^-$  production processes as described in Section 1.2 can occur, to form such compositions. However, neither are the in-medium properties of anti-kaons nor the ones for kaons settled to prove or disprove such scenarios as can be seen in Figure 1.6, in which a rather wide band of possible kaon and anti-kaon energies as a function of the normalized density  $\rho/\rho_0$  is visible depending on the theoretical model. Even a variation of the kaon-sigma term influences the dependency of the kaon energy on the nuclear density, which should be kept in mind. However, several possibilities exist to study the kaon-nucleon interaction experimentally, of which some are discussed in the next sections.

### 1.4.1 Anti-Kaons in Matter - Experimental Observables

The study of anti-kaons is a rather complicated story due to various reasons. For instance anti-kaons, which contain a  $s$ -quark, interact via strangeness exchange with the surrounding nucleons through the process  $K^- + N \rightarrow Y + \pi$  ( $Y = \Lambda/\Sigma$ ) and hence can be absorbed [SBM97], which has to be understood on top of other phenomena. In addition, the  $K^-$  yield is strongly coupled to the  $K^+$  production, which is dominantly formed through the reaction  $p + p \rightarrow \Lambda + p + K^+$  allowing the generation of  $K^-$  mesons through the reverse strangeness

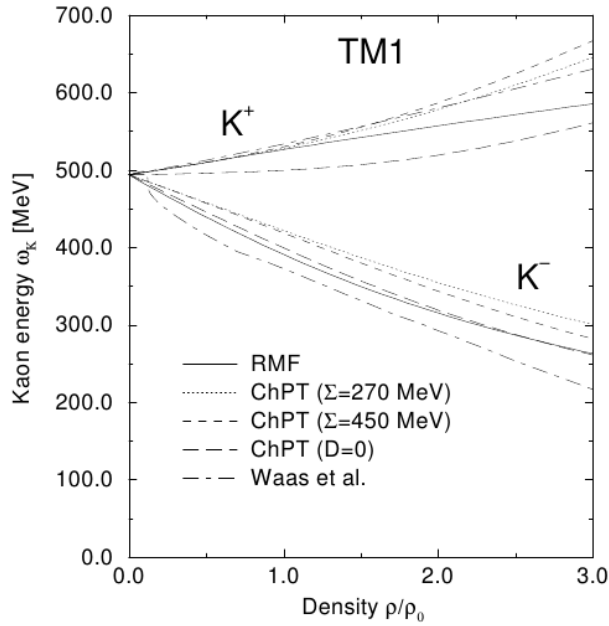


**Figure 1.6:** The kaon and anti-kaon energies as a function of the nuclear density  $\rho/\rho_0$  resulting from various theoretical calculations for a soft EOS (parameter set TM1 according to [SBM97]). Figure from [SBM97].

exchange reaction using the produced hyperon [FUB<sup>+</sup>07, Fuc06]. This factor makes it difficult to extract direct information from  $\bar{K}$  yields and links the study of anti-kaons to the study of kaons. The main complication, however, is related to the presence of resonances close to the  $\bar{K}N$  interaction threshold ( $\approx 1432$  MeV), which hamper the application of perturbative approaches. Instead, non-perturbative calculations like the coupled channel approach have to be employed. One of these resonances is the  $\Lambda(1405)$ , which can be explained as a quasibound state of  $\bar{K}N$  and a resonance of  $\Sigma\pi$ . The other one also lying close enough to the  $\bar{K}N$  threshold is the  $\Sigma(1385)$ , which couples to the  $\Lambda\pi$  resonance. Detailed studies on these states have been performed in several scattering experiments and in different production systems, amongst others using the presented data sample [A<sup>+</sup>12b, A<sup>+</sup>13] to retrieve information on the pole mass, yield, line shape and production dynamics. The description of the experimental results in a conclusive picture is, however, still a big challenge, that has to be faced by theory, especially in the case of the  $\Lambda(1405)$ .

A further method to investigate  $\bar{K}N$  interactions is to form kaonic atoms. These objects can be produced for example with stopped  $K^-$  in a light target such as hydrogen, which in particular allows to study  $K^-p$  interactions, or helium [B<sup>+</sup>11, BBB<sup>+</sup>11, IHI<sup>+</sup>97, IHN<sup>+</sup>98, B<sup>+</sup>05] and probe strong interaction at threshold. Once they are captured by the atom through the replacement of an orbital electron, the anti-kaon cascades down to the 1s ground state, while emitting X-rays with specific transition energies. The transition energy of the ground state and actually also of the higher lying states is then a mixture of the electromagnetic and the strong interaction. Since the QED part is rather well understood,

it is possible to obtain the pure information from QCD, which first of all shifts the energy spectrum relative to the electromagnetic value (e.g.  $\varepsilon_{1s}$ ) and second broadens the energy state (e.g.  $\Gamma_{1s}$ ). With these measured observables one can almost directly obtain the  $K^-p$  scattering length  $a_{K^-p}$  for example through the Deser-Trueman formula [IHN<sup>+</sup>98], which is sensitive to the chiral and isospin symmetry breaking in QCD. In the last decade high precision experiments established a rather solid picture showing that the  $\bar{K}N$  interaction is repulsive at threshold, which corresponds to a negative energy shift of around -200 eV [Zme08]. This, however, contradicts at first glance the earlier statement of an attractive anti-kaon nucleon potential and the dropping  $K^-$  mass with density, but can be explained by the  $\Lambda(1405)$ , which introduces a repulsive contribution to the scattering amplitude at very low densities [RBW05, SBM97]. As a consequence, a large range of attractive  $\bar{K}N$  potentials were predicted, which range from -200 MeV to -50 MeV at normal nuclear matter density, depending on the theory and therefore also on the inclusion of the influence by the  $\Lambda(1405)$  [BEF<sup>+</sup>14, SBM97].

Another interesting way to learn about the kaon-nucleon interaction is to study kaonic bound states, of which the simplest and smallest one is a quasibound state of two nucleons and an anti-kaon ( $ppK^-$  or  $nn\bar{K}^0$ ). This configuration was predicted by theory because of the strong attractive  $\bar{K}N$  potential allowing the  $K^-$  to act like a glue between the nucleons and was intensively searched for by several experiments. However, the situation for experimentalists is quite complicated, since a rather wide range of binding energies ( $BE_{ppK^-} = 16 - 100$  MeV) and widths ( $\Gamma_{ppK^-} = 20 - 100$  MeV) were obtained for this kaonic cluster in different theories using for example a phenomenological Ansatz [AY02, YA02], variational calculations [DHW09, DHW08] or other approaches. A summary of the theories and their predictions can be found in [Mün14]. Under these conditions some experiments have claimed to have observed the  $ppK^-$ , for example using absorbed  $K^-$  mesons in very thin nuclear targets measured by the FINUDA Collaboration ( $BE_{ppK^-} = 115^{+6}_{-5}(\text{stat})^{+3}_{-4}(\text{syst})$  MeV,  $\Gamma_{ppK^-} = 67^{+14}_{-11}(\text{stat})^{+2}_{-3}(\text{syst})$  MeV) [A<sup>+</sup>05] or from the DISTO Collaboration, which have searched for the kaonic bound state in the reaction  $p + p \rightarrow \Lambda + p + K^+$  at 2.85 GeV assuming the decay of the  $ppK^-$  into a  $p\Lambda$ -pair ( $BE_{ppK^-} = 103 \pm 3(\text{stat}) \pm 5(\text{syst})$  MeV,  $\Gamma_{ppK^-} = 118 \pm 8(\text{stat}) \pm 10(\text{syst})$  MeV) [YMK<sup>+</sup>10]. Others did not find a signal for this state, but were able to set an upper limit for its production in the particular collision systems partially using modern techniques like the Partial Wave Analysis (PWA) to take into account interference effects [A<sup>+</sup>15, T<sup>+</sup>14]. Overall, no clear evidence and consistent picture was obtained by the experiments, which is why the issue of the kaonic bound states remains as a hot topic in the strangeness physics.

### 1.4.2 Kaons in Matter - Experimental Observables

The situation for kaons ( $K^+$  and  $K^0$ ) is a lot easier than for anti-kaons, since they cannot be absorbed due to strangeness conservation. That means that the kaon, which contains an  $\bar{s}$ -quark, cannot turn for example into a hyperon via strangeness exchange like an anti-kaon. Furthermore, no resonance states are located in the vicinity of the  $KN$  interaction threshold allowing the usage of perturbative calculations. Thus, a rather clear picture is delivered by

theory on the behavior of kaons in matter, which for instance all agree on a  $KN$  potential, which stays repulsive over the whole density range, in the order of  $U_{opt} = 20 - 40$  MeV at normal nuclear matter density [SBM97, BEF<sup>+</sup>14]. This situation allows to derive direct information from the study of kaon yields, which are reduced by about 30-50% in the presence of a repulsive potential depending on the potential magnitude, the system size and the energy of the reaction. From such studies it was found that the reduction increases with the system size and with decreasing energy, which is attributed to the influence of the repulsive in-medium potential [Fuc06, FUB<sup>+</sup>07].

Moreover, observables on the kaon production dynamics can offer further insight into the properties of  $KN$  interactions. For example, the same reduction of the kaon yield was found by comparing the rapidity density distributions in Ni+Ni and Ar+KCl to transport calculations and the suggestion by theory was confirmed that the impact of the repulsive potential is most pronounced at mid-rapidity [Fuc06, A<sup>+</sup>10, M<sup>+</sup>00, B<sup>+</sup>97]. This effect was explained by the fact that kaons are produced close to threshold, while subthreshold particles are generated mainly around mid-rapidity.

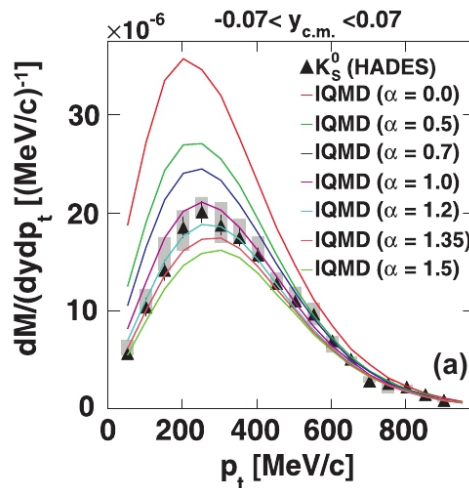


**Figure 1.7:**  $P_t$  distribution of  $K_S^0$  at mid-rapidity measured with HADES in Ar+KCl at 1.756 AGeV (black triangles) taken from [A<sup>+</sup>10]. The colored curves correspond to IQMD simulations with different values for the parameter  $\alpha$ , which directly couples to the strength of the  $KN$  potential.

Furthermore, the investigation of the kaon momentum distribution can help in the understanding of in-medium effects and is one of the objectives, on which the presented work focuses on. In-medium interactions are supposed to act especially on low momentum kaons, which spend more time inside the nucleus and are accelerated by the repulsive  $KN$  potential. This leads on average to a shifted momentum distribution towards higher values and involves the suppression of kaons with low momenta. Several experiments have exploited this feature. One of them is the measurement of the transverse momentum of  $K_S^0$  mesons as a function of rapidity in the heavy ion reaction Ar+KCl at 1.756 AGeV beam energy [A<sup>+</sup>10] shown in Figure 1.7. By studying the neutral kaon no Coulomb effects needed to be taken into account, which somewhat simplified the situation. Furthermore,

the transverse component of the momentum was supposed to be more sensitive to eventual in-medium forces, since the boost introduced by the beam should only appear in the longitudinal term. The resulting  $p_t$  spectrum at mid-rapidity (Fig. 1.7) was compared to the transport calculation IQMD, which incorporated a linear Ansatz for the effective mass  $m^* = m_\rho + U(\alpha)\rho/\rho_0$  with  $U(\alpha) \simeq U_0 + U'\alpha$  ( $U_0 \approx 0.8$  MeV,  $U' \approx 38$  MeV). The plot shows the measured data (black triangles) with a set of IQMD simulations (colored curves), which differ in the  $\alpha$  parameter and hence in the potential strength. First of all, one can see that the yield is reduced due to the repulsion and second, also the shift to higher momenta is visible. Ultimately, the magnitude of the  $KN$  potential was found to be about 40 MeV.

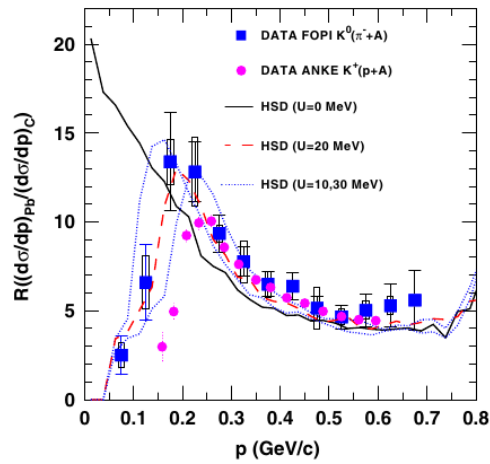


**Figure 1.8:** Ratio of the  $K^0$  yield in Pb to C as a function of the total momentum in pion-induced reactions at 1.15 GeV/c measured with FOPI (blue squares). The pink circles depict the ratio of the  $K^+$  cross section in Au to C in proton-induced reactions at 2.3 GeV with ANKE [B<sup>+</sup>04]. Overlaid are curves from HSD calculations with four different assumptions on the magnitude of the  $KN$  potential. Figure taken from [B<sup>+</sup>09].

Already previous experiments by the FOPI and the ANKE Collaborations have made use of kaon momentum spectra to retrieve information on the  $KN$  potential. In these measurements elementary reactions ( $\pi^-$  [B<sup>+</sup>09] and p-induced [B<sup>+</sup>04]) on targets of different sizes (Pb and C) were investigated. Thereby, a more intense in-medium modification is expected from the Pb reaction due to the higher density of the system. By building the ratio of the measured yields in Pb and C as a function of momentum one obtains then a suppression of the ratio at low momenta, which was indeed observed in the experiments (Fig. 1.8). The blue squares in this figure correspond to the  $K^0$  data from  $\pi^-+A$  reactions and the pink circles to  $K^+$  measurements in p+A collisions. The difference between the two ratios can be attributed to the influence of Coulomb interaction, which shifts the  $K^+$  distribution to higher values. The  $K^0$  data was compared to the HSD transport calculation, which also includes a linear dependence of the  $KN$  potential on the nuclear density. The model demonstrates that the absence of potential effects would not lead to any suppression of the momentum ratio shown as black solid line, whereas its presence does (dashed and dotted

curves). Ultimately, a repulsive  $KN$  potential of  $20\pm 5$  MeV was found to fit the data in the best way. A similar value ( $U^{KN} = 20\pm 3$  MeV) was obtained from the  $K^+$  study in  $p+A$  reactions using CBUU transport calculations. These values, however, disagree with the results determined in Ar+KCl collisions. Hence, a re-measurement of this observable and a deeper understanding of the kaon-nucleon/nucleus interaction starting from kaon production in  $p+p$  reactions is required and is addressed in this work.

## 1.5 The Role of Baryon Resonances in the Study of Kaons

Especially in the low energy regime kaon production is strongly coupled to resonance formation, which should be taken into account in the discussion of kaon physics. The easiest way to produce kaons in baryon induced reactions is through the channel  $B+B \rightarrow B+Y+K$ . In this notation  $B$  either stands for a nucleon or a nucleon resonance ( $N$ ,  $N^*$  or  $\Delta^*$ ) and  $Y$  for a  $\Lambda$  or a  $\Sigma$  hyperon. Therefore, one can find  $N^*$  and  $\Delta^*$  resonances, which decay into  $YK$ -pairs and hence are directly influencing kaon kinematics, as well as the associated formation of a  $\Delta^*$  resonance with the kaon. From theoretical point of view, a precise knowledge of such elementary cross sections is needed to validate and adjust the models as it is commonly done for all kinds of transport models [Fuc06, HOL<sup>+</sup>12], which differ amongst others in the implemented cross section parametrization. As an example, the parametrization derived from the resonance model of Tsushima et al. [TST99] is widely used. Nevertheless, experimental data are not yet described by the model to complete satisfaction. This topic is addressed in Section 1.6 in more detail. Experimentally, it is not possible to study directly  $B + N^*/\Delta^*$  processes due to the very short lifetime of the resonances in the order of  $10^{-24}$  s [O<sup>+</sup>14]. The only way is to derive information through the formation of an intermediate resonance and its subsequent decay (e.g.  $p+p \rightarrow p+N^{*+} \rightarrow p+\Lambda+K^+$ ). Surely, the main decay channel of baryon resonances is the breakup into  $N\pi$ -pairs. Nevertheless, the Particle Data Group (PDG) quotes a bunch of  $N^*$ s and  $\Delta^*$ s with strange decays based on theoretical and as well experimental work [O<sup>+</sup>14], although their properties (mass, width and branching ratios into  $\Lambda K$  and  $\Sigma K$ ) are still not well known. Indeed, already early measurements have found evidence of intermediate baryon resonances in  $p+p$  reactions, that produce strangeness in the final states [BCN66, FAG<sup>+</sup>68]. Also recent studies of the reactions  $p + p \rightarrow p + \Lambda/\Sigma^0 + K^+$  have shown the importance of intermediate resonances [AB<sup>+</sup>10, A<sup>+</sup>15, F<sup>+</sup>13], while the contribution of the resonances seems to be more dominant in the  $\Lambda$  channel. Here, a description of the data without considering  $N^*$  resonances is failing, when it comes to the attempt to reproduce Gottfried-Jackson as well as helicity angles of the reaction [F<sup>+</sup>13, AB<sup>+</sup>10]. One has to mention that  $\Delta^*$  resonances are not taken into account in the study of the  $p\Lambda K$ -final states, since its decay into a  $\Lambda K$ -pair is forbidden due to isospin considerations. A further study on the properties of the  $\Sigma(1385)^+$  resonance in  $p+p$  reactions using the same data sample as in the presented work also suggested the need of a considerable baryon resonance contribution [A<sup>+</sup>12b]. There, the inclusion of the  $\Delta(2035)^{++}$  resonance, which decays into  $\Sigma(1385)^+K^+$ , into the model

helped to reproduce the data, if a quite large amount of 33% of the total  $\Sigma(1385)^+$  yield was assumed to contribute. The role of baryon resonances in p+A and in heavy ion reactions is crucial as well, especially in the subthreshold kaon production. Besides the possibility to produce kaons with extra energy originating from the Fermi momentum of the nucleons inside the nucleus, a  $\Delta$  resonance might be created in the first collision and act as an energy storage for the formation of a kaon through a second collision with another target nucleon [HOL<sup>+</sup>12].

As mentioned above, resonances might not only influence the kaon properties through their decay, but can also affect kaon production kinematics indirectly, if they are produced associated with the kaon. One of these reactions is the following:  $p + p \rightarrow \Lambda + \Delta^{++} + K^0$ , which ends up in the four particle final state  $\Lambda p \pi^+ K^0$  due to the quasi instant decay of the  $\Delta(1232)^{++}$ . Exactly this channel has formerly been studied at different beam momenta  $p_{beam} = 3.65$  GeV/c [N<sup>+</sup>07] and  $p_{beam} = 6$  GeV/c [K<sup>+</sup>70]. Thereby, considerable fractions of the total reaction yield were attributed to the resonant production involving a  $\Delta^*$ . At the higher energy even a contribution of an intermediate  $\Sigma(1385)^+$  resonance was found, which leads to the same four particle final states via its decay into  $\Lambda$  and  $\pi^+$ . Thus, these studies confirm the importance of associated resonance-kaon productions in p+p reactions, which is also crucial for the understanding of heavy ion and p+A collision systems. Another study performed with the same data as analyzed in this work has shown that nearly the whole yield of the  $\Sigma^\pm \pi^\mp p K^+$  final states in p+p reactions at 3.5 GeV are generated together with an intermediate baryon resonance [A<sup>+</sup>12e]. These resonances can be amongst those, that have already been mentioned, the  $\Lambda(1405)$ ,  $\Sigma(1385)^0$  and  $\Lambda(1520)$ . Therefore, it could be assumed that also the  $K^0$  production, which is the key aspect in this work, is strongly influenced by resonance contributions. This topic is addressed in Chapter 4, in which exclusive  $K_S^0$  channels were investigated to determine the role of accompanying resonances at intermediate beam energies.

## 1.6 Transport Model Calculations

Nowadays microscopic<sup>1</sup> transport models are widely-used for the description of all kinds of nuclear reactions, which include hadron-, photon-, electron- and neutrino-induced reactions as well as heavy ion reactions. Thereby, many different production mechanisms need to be taken into account, for example deep inelastic scattering, particle and resonance production at intermediate energies and string excitation and fragmentation at relativistic energies. Since these processes are dominated by many-body effects, which develop dynamically, they need to be described in time-dependent frameworks, in which the particles are simulated including sequential propagations, collisions and decays. That way, transport models naturally take care of rescattering processes, production and absorption of the particles. Such microscopic models are not only appropriate for the interpretation of experimental

---

<sup>1</sup> microscopic models: string, transport, cascade models etc.  
macroscopic models: statistical and hydrodynamical models

data as in the case mentioned above, in which the magnitude of the  $KN$  potential was derived with help of such calculations, but also offer some predictive power. However, these models are strongly dependent on the input of potential energies, elementary inelastic cross sections and decay widths. Especially, there are relatively few available experimental cross sections, if one considers the huge amount of possible hadron-hadron collisions, that need to be included. In case of the unmeasured cross sections, the models have then to rely on extrapolations of known processes. That means that every additional experimental information can help to decrease the number of free parameters in the models and by that reduce uncertainties of the calculations. This is one of the motivations for the exclusive study of  $K^0$  production channels, which is presented in Chapter 4. Moreover, experimental data is often used to cross-check and verify transport calculations, which supports further development of the models. Such cross-checks were carried out in this work for the inclusive  $K^0$  production in p+p reactions (Sec. 3.5), which is important, since even the modeled strangeness production in p+A and heavy ion reactions is influenced by the implementation of such elementary collisions. Three different transport models are focused on in the following, which are cross-checked in the inclusive analysis. These approaches are the HSD (Hadron String Dynamics) [CB99, GCG98, EC96], the UrQMD (Ultra-relativistic Quantum Molecular Dynamics) [B<sup>+</sup>98, BZS<sup>+</sup>99] and the GiBUU (Gießen Boltzmann-Uehling-Uhlenbeck) [B<sup>+</sup>12, WvHM12] models.

**Table 1.1:** Default transition energies  $\sqrt{s}$  between the two internal models, hadron/resonance model and string fragmentation model, for the transport calculations HSD [GCG98], UrQMD [BZS<sup>+</sup>99] and GiBUU [WvHM12] separated with respect to the collision type. The “ $\pm$ ” sign in the GiBUU case indicates a transition window, in which the two models are merged linearly into each other.

	baryon-baryon	meson-baryon
HSD	2.65 GeV	2.1 GeV
UrQMD	5 GeV	3 GeV
GiBUU	$2.6 \pm 0.2$ GeV	$2.2 \pm 0.2$ GeV

In practice, most of the transport simulations incorporate two different models according to the covered energy regime. At low and intermediate energies reactions are described in terms of hadrons or resonances and at higher energies the quarks and gluons become the degrees of freedom, which are specified by so-called strings. These strings, which interact in the prehadronic phase, are characterized by the incoming quarks (baryonic strings:  $qq - q$ , mesonic strings:  $q - \bar{q}$ ), while a tube of color flux is spanned between them. They can be excited and subsequently fragmented to create new particles through virtual  $q\bar{q}$ - and  $qq\bar{q}\bar{q}$ -pairs in the uniform color field. The hadronization of the strings is then supposed to happen independently. Here, the HSD model incorporates the FRITIOF framework [AGP93] and both the models UrQMD and GiBUU use the PYTHIA event generator [SMS06], which in addition includes perturbative QCD effects like multiple minijets. The transport calculations, furthermore, differ in the treatment of strange hadrons at low energies. In HSD reaction channels like  $NN \rightarrow NYK$  and  $\pi N \rightarrow NK\bar{K}$  are explicitly parametrized

according to a previous study, in which the HSD model was used to fit experimental data [CBM<sup>+</sup>97], other reactions like  $\pi N \rightarrow YK$  and  $\pi\Delta \rightarrow YK$  were embedded with respect to the parameterizations of a resonance model developed by Tsushima et al. [THF95, THF94]. Also the GiBUU model applies cross section parameterizations in the strangeness sector but only according to the resonance model of Tsushima et al. [TST99]. In the GiBUU approach, however, resonances are not explicitly propagated, instead only the final non-resonant reactions are implemented (when the resonance has decayed). In contrast, resonances including their decay are explicitly generated in the UrQMD model even in the strangeness sector. Also in this calculation, cross section parameterizations are implemented based on simple phase space considerations, while the free parameters are tuned to experiment. Finally, all the transport approaches take care of a smooth transition between the low and high energy models, although the change from one model to the other takes place at different transition energies, which corresponds to the string threshold. In Table 1.1 the different default thresholds of the models HSD [GCG98], UrQMD [BZS<sup>+</sup>99] and GiBUU [WvHM12] are quoted according to the collision type, baryon-baryon or meson-baryon. Thereby, the GiBUU model features a transition window, in which the two models are merged linearly into each other to ensure a smooth transition. The string thresholds are set in the transport models quite similarly assuming that already at rather low energies the relevant degrees of freedom are the quarks and gluons. The HADES experiment is nicely suited to validate this assumption, since its operating energy regime lies exactly in this transition region and so it is also the case for the studied data sample, which was recorded at  $\sqrt{s} = 3.18$  GeV.

The common underlying transport equation implemented in the models is the BUU (Boltzmann-Uehling-Uhlenbeck) equation (Eq. 1.5). A coupled set of this equation describes the space-time evolution of a many-particle system through a mean-field potential including a collision term. Thereby, each particle species is represented by one differential equation of a single-particle phase space distribution  $f(\vec{r}, \vec{p}, t)$ , which can be written in its non-relativistic form as follows [BDG88]:

$$\frac{df}{dt} = \frac{\partial f(\vec{r}, \vec{p}, t)}{\partial t} + \frac{\vec{p}}{m} \vec{\nabla}^{(r)} f(\vec{r}, \vec{p}, t) - \vec{\nabla} U(r) \vec{\nabla}^{(p)} f(\vec{r}, \vec{p}, t) = I_{coll} \quad (1.5)$$

with

$f(\vec{r}, \vec{p}, t)$  : single particle phase space distribution

$U(r)$  : mean field potential

$I_{coll}$  : collision term

The left hand side of the equation corresponds to the so-called ‘‘Vlasov term’’ and incorporates the propagation of stable, non-interacting particles under the influence of mean-field hadronic and electromagnetic potentials. At the right hand side of the BUU equation one can find the collision term, which includes gain and loss terms according to scattering and decay processes and the associated hadron production and absorption rates. Usually only two-body collisions are implemented so that for example an intermediate step needs to be added to obtain the final three-body reaction (e.g.  $NN \rightarrow N\Delta \rightarrow NYK$ ). An exception is the GiBUU model, from which also three-body collisions are available. Furthermore, Pauli

blocking is considered in the collision term, which suppresses the collision, if the phase space is already occupied by another particle. An explicit formulation of that term can be found in [BDG88].

There are two different strategies to solve the coupled transport equations numerically. The semi-classical models HSD and GiBUU incorporate the so-called “test-particle” ansatz. In this approach the continuous phase space distribution  $f(\vec{r}, \vec{p}, t)$  is replaced by a large number  $N$  of test-particles each forming a  $\delta$ -function in coordinate and momentum space:

$$f(\vec{r}, \vec{p}, t) \rightarrow \sum_r^N \delta(\vec{r} - \vec{r}_i(t)) \delta(\vec{p} - \vec{p}_i(t)). \quad (1.6)$$

Thereby, the assumption is made that the many-body system behaves like a classical fluid on “macroscopic” space-time scales. This is, furthermore, possible in the quasi-particle limit. Since the spectral functions of many particles are quite narrow, it is allowed to assume that the particles are on the energy shell. On the other hand, particles with broad spectral functions like short-lived mesons, require the solution of the full transport equations and the consideration of nontrivial energy-momentum dependent spectral functions. The classical way to solve the transport equations is the implementation of QMD like in UrQMD. This theory is a many-body theory, which translates the soft part of the effective interaction in the medium into a classical but density and momentum dependent two-body interaction. Thereby, quantum effects like Pauli blocking and quantum mechanical scattering must be supplemented [B<sup>+</sup>98]. A striking difference to the test-particle ansatz can be identified in the representation of particles. Here, a nucleon for example is not represented by a  $\delta$ -function, but by a coherent state in the form of a Gaussian wave packet formulated in the following way:

$$\phi_i(\vec{x}; \vec{q}_i, \vec{p}_i, t) = \left( \frac{2}{L\pi} \right)^{3/4} \exp \left\{ -\frac{2}{L} (\vec{x} - \vec{q}_i(t))^2 - i\vec{p}_i(t)\vec{x} \right\} \quad (1.7)$$

with

$\vec{q}_i$  and  $\vec{p}_i$  : six time-dependent parameters

$L$  : extension of the wave packet in phase space

The nucleus is then represented as the direct product of the single nucleon wave functions:

$$\Phi = \prod_i \phi_i(\vec{x}; \vec{q}_i, \vec{p}_i, t) \quad (1.8)$$

This ansatz can, therefore, account for particle states of different widths and smooths at the same time the boundaries of the spectral functions. The collision criterion in this case is dependent on the total cross section:

$$d \leq d_0 = \sqrt{\frac{\sigma_{tot}}{\pi}}, \sigma_{tot} = \sigma(\sqrt{s}, type) \quad (1.9)$$

with

$d$  : distance between the two particles in their CMS frame

$d_0$  : maximum distance for a collision

$\sigma_{tot}$  : energy and collision type dependent total cross section

According to this criterion, two particles collide, if their distance (e.g. centers of the Gaussians) drops below a certain  $d_0$ , which is related to the energy dependent total cross section of the specific collision type. Thereby, the cross section corresponds to the free cross section, which is often parametrized from experimental data if available. If the cross section of a process is not known, isospin symmetry and the principle of detailed balance are assumed. The detailed balance is based on the time reversibility of a reaction leading to two assumptions:

1. Each resonance produced via a meson-baryon or meson-meson annihilation may as well decay again into the two hadron species, which had formed it.
2. The cross section for a baryon-resonance excitation is also valid for its reverse reaction, which is often not measured.

In the end, experimentalists and theorists are interdependent. The measured data need to be interpreted by theoretical calculations, on the other hand, the models require experimental input in terms of potential strengths and cross sections at various energies. These two sectors are, therefore, bound together and can only develop in parallel.



## 2 The HADES Experiment

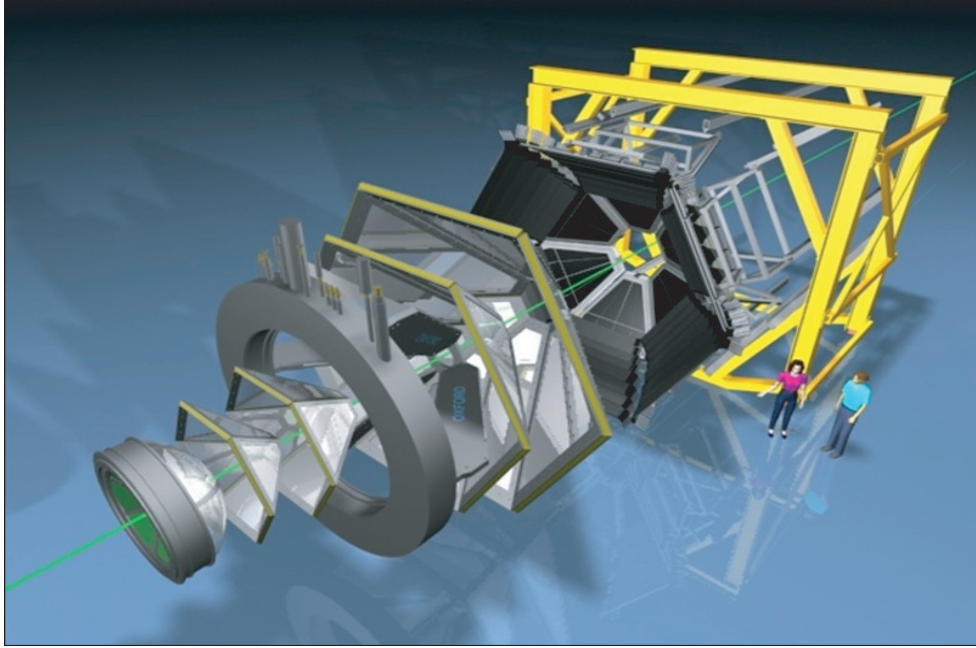


**Figure 2.1:** The HADES detector setup shown in an exploded view. The beam indicated by the green line comes from the lower left corner.

The **H**igh **A**cceptance **D**i-**E**lectron **S**pectrometer is a fixed target experiment located at the GSI Helmholtzzentrum für Schwerionenforschung in Darmstadt, Germany [A<sup>+</sup>09]. The detector setup operates at the SIS18 (**S**chwer**I**onen **S**ynchrotron) accelerator, which can deliver ion beams with kinetic beam energies in the range of 1-2 AGeV for nucleus-nucleus reactions. For proton-induced reactions energies up to 3.5 GeV can be achieved. The experiment was developed such to optimize the study of dilepton pairs, which could stem from light vector mesons such as  $\rho$ ,  $\omega$  or  $\phi$ . These particles are very suitable for the investigation of possible in-medium modifications, since their short lifetimes are comparable to the duration of the compression phase of relativistic heavy ion collisions at the SIS18 energies and thus usually decay within the nuclear matter. Furthermore, the electromagnetic  $e^+e^-$ -decay of the vector mesons is not influenced by strong final-state interactions, which allows an undistorted extraction of the in-medium informations like the vector meson masses and widths. Recent results from these measurements in various colliding systems like Ar+KCl, C+C, p+Nb, d+p and p+p can be found in [Gal14, ABB<sup>+</sup>14, A<sup>+</sup>12c, A<sup>+</sup>12d, A<sup>+</sup>11, A<sup>+</sup>08, L<sup>+</sup>09] and others.

However, the HADES setup is also applicable for the study of hadrons. The excellent performance of hadron identification has been exploited in several analyses especially in the field of strangeness physics. And so various topics were addressed regarding for example the  $KN$  potential [A<sup>+</sup>10] in Ar+KCl collisions,  $\Lambda$ -polarization [A<sup>+</sup>14b] in p+Nb reactions, the search for the existence of the kaonic cluster ( $ppK^-$ ) [F<sup>+</sup>13, A<sup>+</sup>15], the production of the  $\Lambda(1405)$  [A<sup>+</sup>13] and  $\Sigma(1385)$  [A<sup>+</sup>12b] resonances in p+p reactions and others.

In the following, the description of the HADES detector systems will be found in Section 2.1, the method applied for particle identification will be explained in Section 2.2, informations concerning the beam time of the presented p+p data will be available in Section 2.3 and the simulation tools used in this analysis will be addressed in Section 2.4.

## 2.1 Detector Systems

The HADES setup is constructed by six identical sectors (Fig. 2.1), which are arranged in the azimuthal plane such to achieve a coverage as large as possible with around 85%, which is reduced mainly due to mechanical supporting structures. The polar angle acceptance ranges from  $\Theta = 18^\circ$  to  $\Theta = 85^\circ$  for single particles. For reconstructed particles decaying into two particles with opposite charge (e.g.  $K_S^0 \rightarrow \pi^+ + \pi^-$ ) the acceptance is even higher starting already at  $\Theta = 0^\circ$ . The overall momentum resolution integrated over all particle tracks was determined from the p+p data and found to be  $\approx 4\%$ . A cross section through the HADES setup shown from the side is depicted in Figure 2.2. The shown detector components will be explained briefly in the next sections including the Forward Wall, which is not shown in the figure. A more detailed description of the detectors can be found in [A<sup>+</sup>09]. The colored curves indicate possible particle tracks through the detector system, which are bend more or less by the toroidal magnetic field depending on their charge and momentum.

### 2.1.1 The Target

The target for the HADES experiment is positioned in an environment free of magnetic field, which is important for the study of the light dileptons. This could be accomplished by using a toroidal magnetic field (see Sec. 2.1.3). Various target materials can be mounted in the setup, which can be solid materials in form of a single block or segmented into thin disks to reduce scattering in the target or liquid materials like liquid hydrogen (LH<sub>2</sub>) for the study of p+p or d+p reactions.

### 2.1.2 The RICH Detector

The **R**ing-**I**maging **C**herenkov detector is the first detector traversed by the particles after the collision in the target. It is located still in front of the superconducting magnet and requires an almost field-free region for the detection of  $e^+e^-$ -pairs. The whole HADES

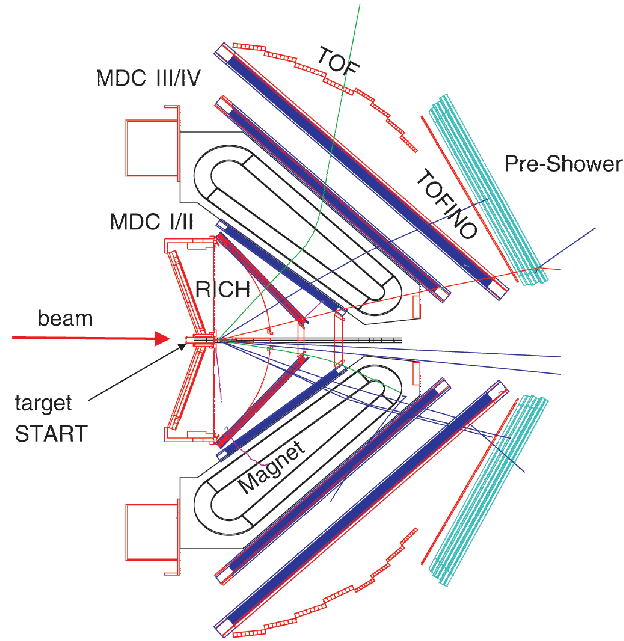


**Figure 2.2:** Cross section of the HADES system illustrated from the side. All detector systems and the magnet are depicted except the Forward Wall. The colored curves indicate possible particle tracks through the spectrometer.

acceptance is covered by the RICH detector, which basically consists of two separate gas volumes. The volume seen by the particles is filled with  $C_4F_{10}$  and acts as the radiator gas with a characteristic Lorentz factor for Cherenkov light of  $\gamma_{thresh} = 18$ , which enables electrons and positrons to produce Cherenkov light, but suppresses Cherenkov light emission from muons and hadrons at SIS18 energies. In that sense, the RICH detector is hadron-blind and therefore did not deliver relevant information for the presented  $K_S^0$  analysis. Nevertheless, the Cherenkov photons are then reflected by a aluminum coated carbon mirror through a  $CaF_2$  window, which separates the  $C_4F_{10}$  gas from the  $CH_4$  filled photon detector volume, and finally hit the CsI photo cathode. To amplify the knocked out photo electrons six Multi-Wire Proportional Chambers (MWPC) are installed in front of the readout pad plane. Since the geometry of the RICH detector was designed in a way that the Cherenkov rings hitting the pad plane have an almost constant diameter, an online ring search could be implemented for the LVL2 trigger used for dilepton analysis (Sec. 2.1.8).

### 2.1.3 The Magnet

Charged particles flying through a magnetic field are bend according to the Lorentz force. By measuring the bending of the particles and knowing their charge from the bending direction one can directly derive the momentum information. The HADES magnet consists of six electromagnetic coils, which generate a toroidal field providing a nearly field-free region around the target and the active volume of the RICH detector. Although the field

strength required by the magnet is rather low, superconducting magnets were installed to enable a compact design of the spectrometer keeping the magnetic field low in the surrounding detector systems (e.g.  $B \approx 0.08$  T in MDC I). The maximum field is reached in the forward arc of the coil with 3.6 T at the sector edge and 0.9 T in the midplane between two adjacent coils.

### 2.1.4 The Multi-Wire-Drift Chambers

In the closest vicinity of the magnet four planes of **Multi-Wire Drift Chambers** (MDC I-IV) were mounted, two upstream of the coils and two downstream. Each of these planes consists of six identical chambers with trapezoidal shape following the sectioned HADES geometry. Each chamber is continuously flushed with a helium-based counting gas ( $\text{He}:\text{C}_4\text{H}_{10} = 60:40$ ) and is made of six planes of sense/field wires oriented in six different stereo angles, e.g.  $\pm 0^\circ$ ,  $\pm 20^\circ$ ,  $\pm 40^\circ$ , which allows to maximize spatial resolution (e.g.  $\sigma_x \approx 140 \mu\text{b}$ ). In total about 1100 drift cells are formed by this construction. The particles traversing through the drift chambers ionize the gas along their trajectory producing electrons amongst ions, which are multiplied by avalanche effects in the electric field. The electric field causes a drift of the electrons to the sense wires, where they induce an electric signal that can be read out. Thereby, a precise measurement of the hit positions in the individual MDC planes can be obtained. For the Runge-Kutta tracking algorithm the two nearly straight hit points in the MDC I and MDC II planes are combined to an inner track segment and the hit points in MDC III and MDC IV to an outer track segment, which is inclined due to the magnetic field between plane II and III. Together with the precisely known magnetic field map and eventually the hit points in the META system (see next section), the equation of motion can be solved in a numeric way and delivers particle track points, the path length and the momentum with a momentum resolution of 1-4%.

A further information that can be retrieved from the MDCs is the energy loss information  $\Delta E$ . Since no ADCs were foreseen for the readout, the correlation of the energy loss to the Time over Threshold (ToT) was exploited. The ToT is the duration in which the electric signal overshoots an adjusted threshold and is connected to the drift time of a particle and therefore to its energy loss in the given gas mixture. A rather complicated calibration procedure to entangle dependencies on the reduced electric field, on the track geometry, on the drift cell size and others was carried out and is explained in [A<sup>+</sup>09]. Ultimately, an energy loss resolution could be obtained in the order of 7% for minimum ionizing particles and for stronger ionizing particles an even better resolution of around 4% could be achieved. This feature is a very important information for the hadron analysis, since it can be used for particle identification as explained in Section 2.2.

### 2.1.5 The META System

The **Multiplicity and Electron Trigger Array** (META) consists of the time-of-flight scintillators **TOF** and **TOFino** and the electromagnetic shower detector (**Pre-Shower**). They

are located behind the MDC plane IV and are mainly used for triggering and particle identification purposes.

- The **TOF** detector is sectioned into the usual six trapezoidal shapes and consists in total of 384 scintillator rods, which are arranged per sector into eight planes with each eight rods. The polar angle coverage of this time-of-flight detector ranges from  $44^\circ$  to  $88^\circ$ . Particles that fly through the scintillators induce photon emission, which is detected on both sides of the rods with help of Photo-Multiplier-Tubes (PMTs). In that way the arrival time of the photons and the signal height are measured, from which the particle time-of-flight and energy loss information can be determined. Due to the double sided readout of the scintillator rods, an intrinsic time resolution of  $\sigma_t \approx 150$  ps can be reached.
- The **TOFino** detector also follows the six-folded geometry of the HADES setup, but covers a smaller polar angle range  $\Theta = 18^\circ - 45^\circ$ . With its four scintillator paddles per sectors, which are arranged radially with respect to the beam axis, a rather low granularity is provided by the detector enhancing the double hit probability per scintillator. The readout is carried out only on one side of the paddle with PMTs, which results in a worse intrinsic time resolution of  $\sigma_t \approx 420$  ps.
- The **Pre-Shower** detector is installed right behind the TOFino detector covering the same azimuthal and polar angles. Each Pre-Shower sector is composed of three wire chambers filled with an isobutane-based gas mixture, which are separated by Pb converter plates. Electrons and positrons produce electromagnetic showers in the Pb plates, when hitting them. Although also hadrons can generate showers, they will leave different signal characteristics in the detector, so that a separation of the leptons from hadrons is possible complementing the abilities of the RICH detector. The high granularity of the Pre-Shower pad readout (942 pads per wire chamber), which is optimized for a minimal double hit probability in one single pad (below 5% in Au+Au collisions), compensates the poor position resolution of the TOFino.

Since 2009 major improvements were undertaken to upgrade the HADES setup. In the course of this upgrade not only the new electronic readout systems were installed, but also the TOFino detectors were replaced by a **R**esistive **P**late **C**hambers (RPCs) that feature a much higher granularity and an intrinsic time resolution of  $\approx 66$  ps on average [AP<sup>+</sup>04, BFG<sup>+</sup>13]. These improvements were necessary for the operation at the future Facility for Antiproton and Ion Research (FAIR). The functionality of the upgraded system has been proven in 2012 during a Au+Au beam time at 1.25 AGeV.

### 2.1.6 The Beam Detectors

Beam detectors in the HADES setup are used for various purposes like beam monitoring, beam-profile, time structure analysis and for the time-of-flight measurement by delivering the start time. In pion-induced experiments they are also exploited to measure the momentum of the incoming pions, as the pion beam is a so called secondary beam. In heavy ion reactions the common material employed for the START detector is polycrystalline

diamond, which show high-rate capability, radiation hardness, a fast signal collecting time and low noise with a time resolution of about 30 ps. However, these diamond detectors positioned in front of the target cannot be used for light projectiles like pions, protons or deuterons, since the deposited energy is too small. In addition, it is not possible to run a start detector for high intensity proton beams ( $\geq 10^7$  particles/s) due to the induced background, which would hinder the stable operation of the RICH detector.

### 2.1.7 The Forward Wall

The deuteron beam time in 2007 required the possibility to detect the spectator protons, which is why an additional detector was build to cover very forward angles. Therefore, the Forward hodoscope Wall (FW) located 7 m downstream from the target has an acceptance in  $\Theta$  of  $0.33^\circ - 7.17^\circ$  and a full azimuthal coverage. It consists of about 300 scintillator modules each with a thickness of 2.54 cm read out by individual PMTs providing sensitivity on the hit position. The time resolution is in the order of 500 ps [K<sup>+</sup>11, L<sup>+</sup>09]. Since no other detectors are overlapping with the acceptance of the FW, no information can be deduced on the particle momentum. However, the FW was successfully commissioned in the p+p beam time at 3.5 GeV and indeed could deliver additional information in the analysis shown in [EF12]. Furthermore, it allows to reconstruct the event reaction plane in heavy ion reactions (e.g. Au+Au), which can be used to study flow observables.

### 2.1.8 Trigger and DAQ

To reduce the dead time of the **Data Acquisition (DAQ)** an efficient trigger logic has to be implemented, which does not introduce a bias on the recorded physics data, but at the same time decrease the probability to collect fake data from electronic noise. For the dilepton studies a multi-step trigger process is applied leading to the two trigger levels, level-1 (LVL1) and level-2 (LVL2), which are distributed via a Central Trigger Unit (CTU) to the individual subsystems:

- The digital **LVL1** trigger generated by the CTU depends on the input settings such as multiplicity trigger, minimum bias or calibration trigger. With help of the multiplicity trigger, which requires more than one hit in the META system (e.g.  $\geq 3$  in p+p @ 3.5 GeV), inelastic reactions are enhanced in the recorded data sample. The multiplicity trigger can also be used to select certain centralities in heavy ion reactions. However, to further reduce the number of events written to disk a downscaling factor can be implemented, if necessary. The LVL1 trigger signal is transmitted to the sub-detectors within 500-600 ns, which means that the HADES trigger system is not dead time free. Nevertheless, it ensures that only complete events are recorded.
- The **LVL2** trigger decision is essential for the dilepton study, since the algorithm is programmed to select events with electron candidates. The search for electron candidates is based on the electron signatures in the data provided by relevant detectors: Cherenkov rings in the RICH, fast particles in the TOF or electromagnetic

shower in the Pre-Shower. The informations are combined and depending on the trigger decision, the event is stored into a separate memory.

If the trigger decisions are positive, the informations are send to the Event Builder (EB), then the data are combined into complete events and finally saved to disk. For hadron analysis and also to study the LVL2 trigger algorithm, additionally events passing only the LVL1 trigger are stored with a certain downscaling factor.

## 2.2 Particle Identification

The HADES detector setup allows for particle identification either via energy loss or via time-of-flight measurements in combination with the determination of the particle's momentum. The energy loss ( $dE/dx$ ) information can be extracted from the multi-wire drift chambers (MDCs), from the TOF or the TOFINO detectors. This particle identification method exploits the effect as predicted by Bethe-Bloch [Bet30]. The Bethe-Bloch-formula can be written as follows:

$$-\left\langle \frac{dE}{dx} \right\rangle = 4\pi N_A r_e^2 m_e c^2 z^2 \frac{Z}{A} \frac{1}{\beta^2} \left[ \frac{1}{2} \ln \left( \frac{2m_e c^2 \beta^2 \gamma^2 T_{max}}{I^2} \right) - \beta^2 - \frac{\delta}{2} \right] \quad (2.1)$$

with

- $z$  : charge of the incident particle
- $Z, A$  : atomic and mass number of the traversed medium
- $m_e$  : mass of the electron
- $r_e$  : Bohr electron radius
- $N_A$  : Avogadro number
- $I$  : mean excitation potential of the material
- $\delta$  : density correction

The maximal transferred kinetic energy  $T_{max}$  is limited to:

$$T_{max} = \frac{2m_e c^2 \beta^2 \gamma^2}{1 + 2\gamma m_e/M + (m_e/M)^2} \quad (2.2)$$

with

- $M$  : mass of the incident particle

If the mass of the incident particle has a much larger mass than the electron ( $M \gg m_e$ ), its energy loss in a certain medium defined by  $Z, A$  and  $I$  only depends on its velocity  $\beta$  and its charge  $z \cdot e$ . Since the velocity is related to the momentum and the mass via  $p = c\beta\gamma m$ , the energy loss as a function of the momentum is specific for each particle type.

The theoretical Bethe-Bloch curves are plotted in the MDC  $dE/dx$  distributions (Fig. 2.3) as a function of the momentum for various particles, in which one can see a clear separation of the  $\pi^+$  from the protons up to a momentum of 1000 MeV/c for experimental data (panel (a)). Graphical two-dimensional cuts were used to assign the tracks with a PID (particle ID). In this work only the  $dE/dx$  information of the MDCs were used, as the  $dE/dx$  distribution from the TOFino only allows for a separation of the  $\pi^+$  from the protons below 500 MeV/c (see Appendix A.1, panel (b)). The energy loss distribution from the TOF detectors does not deliver more information, but rather show a contamination of the few hundred MeV/c momentum pions by stopped protons (Appendix A.1, panel (a)).

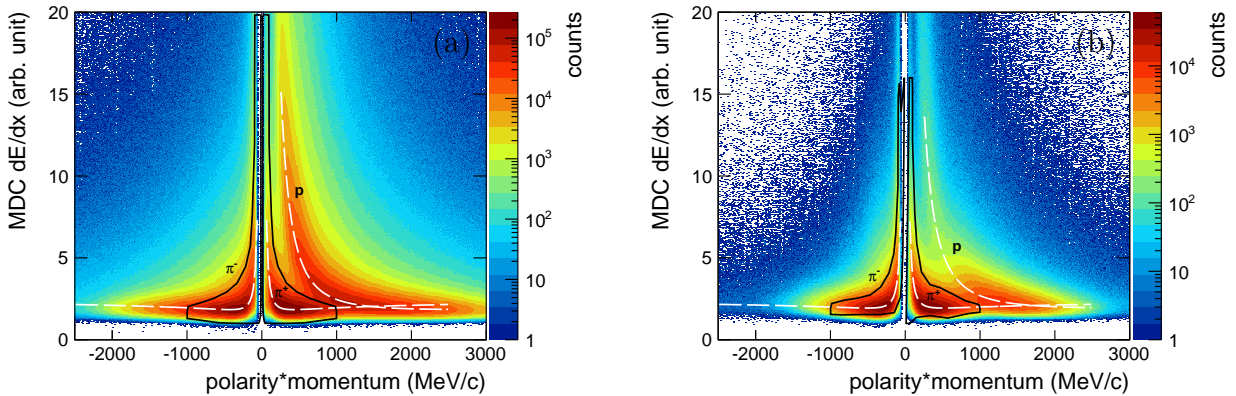


**Figure 2.3:** Energy loss  $dE/dx$  in the MDCs as a function of the momentum times charge of the track. Panel (a) shows the experimental distribution and panel (b) the simulated Pluto/Monte Carlo cocktail made of 13 different reactions containing a  $K_S^0$  in the final state. The white dashed lines indicate the specific energy loss functions according to Bethe-Bloch (Eq. 2.1). The black lines correspond to the applied  $\pi^+$  and  $\pi^-$  graphical cuts.

For later efficiency corrections, simulated data were analyzed the same way as the experimental data, meaning that also the particle identification was performed as described. However, the selection efficiency of the graphical cuts needed to be equal for simulated and experimental data. By default the application of the same energy loss cuts to the simulations did not meet this requirement. The reason for that is that the energy loss resolution as a function of the momentum is not implemented correctly for simulations. As demonstrated in Figure 2.3 the simulated resolution is better than the experimental one, where a wider spread of the data is visible with respect to the theoretical Bethe-Bloch curves. (The simulation contains a cocktail of different reactions with a  $K^0$  in the final state. More details can be found in Section 2.4.) Therefore, a procedure was developed to modify the experimental energy loss cut such to guarantee the same selection efficiency. In this procedure the energy loss distributions were sliced in 18 MeV/c momentum bins and projected onto the energy loss axis. By a Landau fit of these projected spectra the width and the mean of the experimental and the simulated data were obtained, so that the graphical cut for the simulations could be adjusted according to the differences in width and mean per momentum bin. As a result the graphical cut was narrowed, since the simulated resolution is better. This is also visible in Figure 2.3 for positive and negative pions.

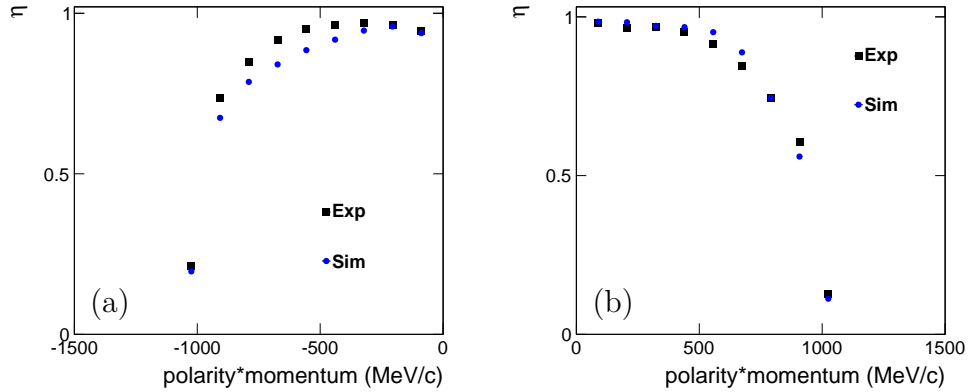


**Figure 2.4:** Track selection efficiency of the two-dimensional graphical cuts on the MDC  $dE/dx$  for experimental data and simulation. Panel (a) shows the efficiency for  $\pi^-$  and panel (b) the corresponding plot for  $\pi^+$ .

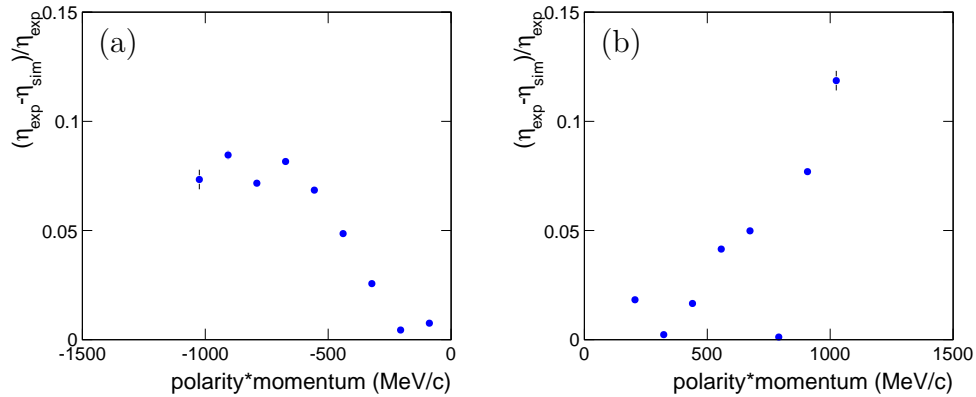


**Figure 2.5:** Relative difference of the track selection efficiency (Figure 2.4) between experiment and simulation for  $\pi^-$  (panel (a)) and  $\pi^+$  (panel (b)).

To verify this PID cut moving procedure, a simple check was performed, in which the selection efficiencies for pions were determined. For this purpose, a preselection of the particle species was applied making use of the TOF  $dE/dx$  information. The MDC  $dE/dx$  distribution of the remaining tracks is illustrated in Appendix A.2. The selection efficiency  $\eta$  for a specific particle species was then obtained for momentum slices of 117 MeV/c, which was defined as follows:  $\eta(p) = N_{Au}(p) / N_{InCut}(p)$ . Here,  $N_{Au}(p)$  corresponds to the number of counts in a certain momentum bin, whereas  $N_{InCut}(p)$  stands for the number of counts lying inside the PID cut of the same momentum region. In the ideal case the selection efficiency for simulated data should not differ from the one of experimental data. An absolute comparison for  $\pi^+$  and  $\pi^-$  is depicted in Figure 2.4. A more meaningful presentation is shown in Figure 2.5, where the relative differences of the efficiencies are

plotted. Both for the  $\pi^+$  and for the  $\pi^-$  the relative difference stays well below 15%, which is sufficient, but also shows the limitation of this method.

## 2.3 The p+p Beam Time

In the current work an analysis was performed on data of p+p reactions at a kinetic beam energy of 3.5 GeV ( $\sqrt{s} = 3.176$  GeV), which were collected in April 2007. The proton beam with an average intensity of  $1 \cdot 10^7$  particles/s was impinging on a cylindrical target cell, which was filled with liquid hydrogen. The dimensions of the target cell were 15 mm in diameter and 44 mm in length. This corresponds to the total interaction probability of 0.7%. All detector systems of HADES as described in Section 2.1 were running except for the start detector and the recently installed RPCs. With this configuration around  $1.14 \cdot 10^9$  minimum bias events were recorded. Such events were detected with a LVL1 trigger, that required at least three hits inside the META system. Furthermore, a downscaling factor of three was used meaning that only every third LVL1 event was written to tape. The missing start detector during this beam time did not allow for the direct measurement of a particle's time of flight, which could be used for particle identification. Also it complicates the determination of the beam position on the target cell. As a consequence, a dedicated primary vertex calculation was developed and studies on possible shifts of the beam spot in the x-y plane (z-direction corresponds to beam direction) had to be carried out.

### 2.3.1 Primary Vertex Calculation

The calculation of the position of the primary vertex is necessary to find out, whether the beam spot has moved and if yes, how much it has moved during the beam time. This information is again needed for a more precise calculation of the primary vertex of events including particles, which are reconstructed via its decay particles. For the first application all tracks originating from the primary vertex were intersected with each other and the average coordinates of the intersections were assigned to the primary vertex position. Note that here and further on, the point of closest approach between two tracks is meant as intersection points. Thereby, those tracks were defined as primaries, that cross the target region, which is defined as a cubic volume around the target cell with the dimensions  $15 \times 15 \times 90$  mm<sup>3</sup>. Furthermore, only events with at least three primary tracks were used in this approach, so that no information of the actual beam position was needed. The so determined primary vertex distribution is visible in Figure 2.6.

For the second application, in which the primary vertex of an event was calculated for an analysis of short lived particles (here  $K_S^0$ ), the procedure was slightly different. First a  $K_S^0$  candidate was reconstructed from its charged decay pions ( $\pi^+$  and  $\pi^-$ ) and its track was supposed to traverse the target region as described above. This reconstructed track and the remaining primary tracks were then intersected with each other, without using the decay particles again. As explained before, the average coordinates of the intersections were then treated as the primary vertex. In the case, in which no other primary tracks than the

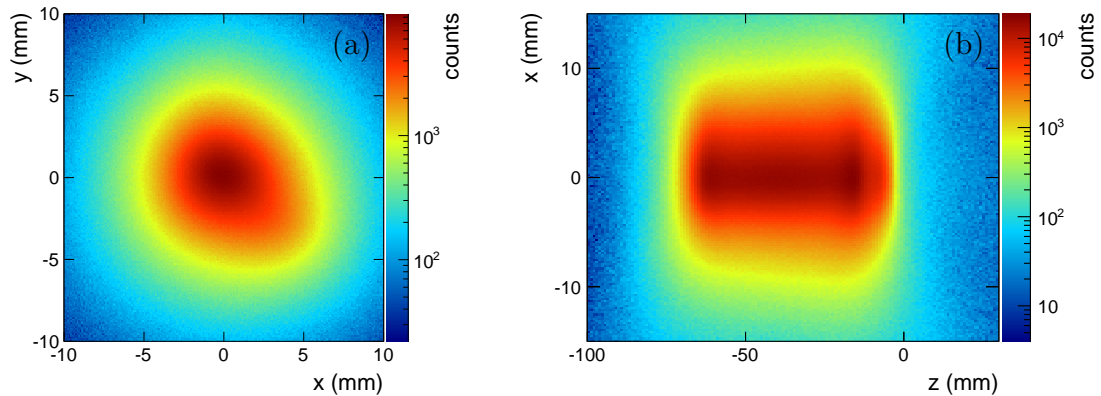


**Figure 2.6:** Primary vertex distributions in the x-y- (panel (a)) and in the x-z-plane (panel (b)) for events with at least three tracks crossing a predefined target region.

reconstructed  $K_S^0$  was present in the event, the reconstructed  $K_S^0$  track was intersected with the corrected beam axis (more details in Sec. 2.3.2) and this intersection point was stored as the primary vertex. The primary vertex distribution of events containing  $K_S^0$  candidates is visible in Figure 2.7. Spot-like maxima are observed in the x-y-plane and horizontal stripes along the z-axis, which are due to events with only two tracks or one reconstructed primary track, respectively. The precise knowledge of the primary vertex position was especially important for this analysis, as off-vertex cuts needed to be applied to distinguish between particles originating from the primary or the decay/secondary vertex. Details about applied off-vertex cuts are explained in Section 3.1.1.

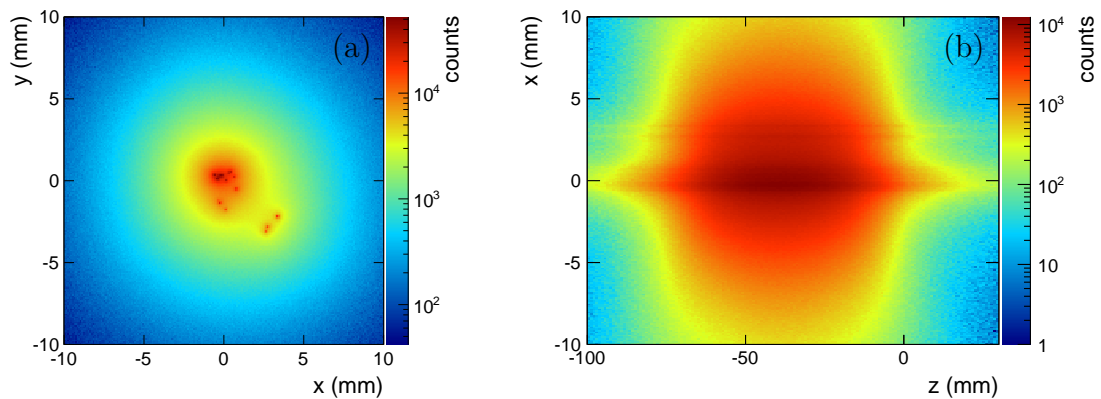


**Figure 2.7:** Primary vertex distributions in the x-y- (panel (a)) and in the x-z-plane (panel (b)) for events containing  $K_S^0$  candidates. The primary vertex was calculated with the shifted beam axis (see Section 2.3.2).

### 2.3.2 Beam Shift Studies

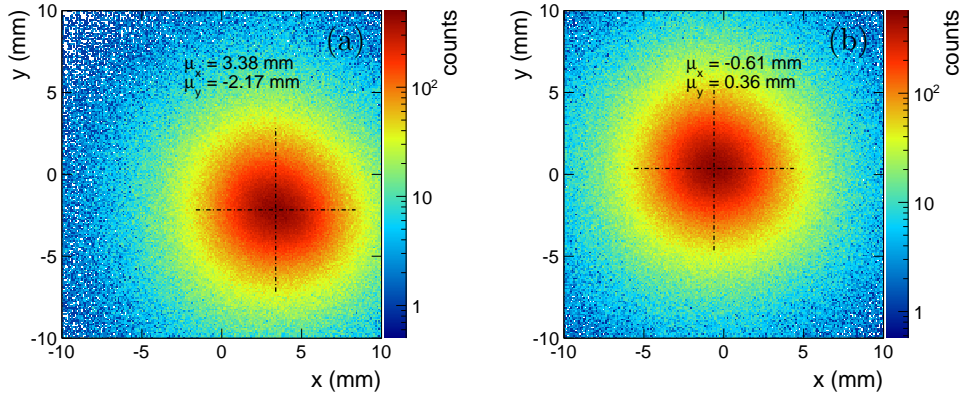


**Figure 2.8:** Primary vertex distribution in the x-y-plane for events with at least three tracks in a predefined target region shown for data taken on the calendar day 107 (panel (a)) and 122 (panel (b)).

As already mentioned, a possible shift of the beam spot on the target cell during the p+p beam time had to be quantified, because this information is needed for the primary vertex calculation involving decaying particles. A shift of the beam spot could have been introduced for example during beam tunings. Indeed, when plotting the primary vertex as discussed above integrated over the full beam time, one can see an oval, eccentric distribution in the x-y-plane (Fig. 2.6, panel (a)). It was found that a correction of the beam axis could be applied in time intervals of one day, except for one day, during which the beam was tuned leading to a considerable shift. As an example, Figure 2.8 shows the primary vertex distributions for two different beam days, in which a shift in x and y are clearly observed. This shift was quantified by fitting the x and y projections of the distribution with a Gaussian function. Figures 2.9 and 2.10 depict the mean values per day (half day), whereas the standard deviations from the fit are plotted as error bars from the mean. Slight changes but also jumps in the order of 3 – 4 mm of the mean are seen, which needed to be corrected, whereas the primary vertex resolution stays rather constant. In the beam/z-direction no shift was seen, which could have been caused by moving the target cell. Therefore, no correction was necessary in this dimension.

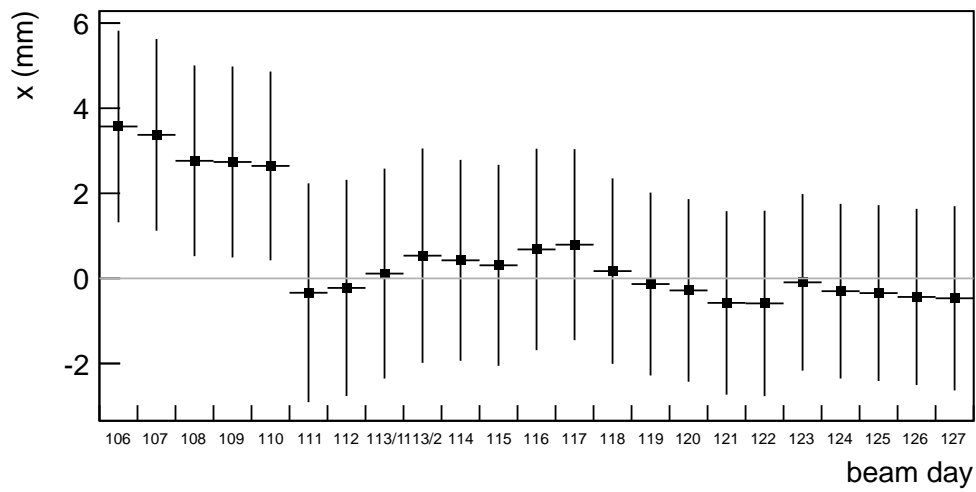


**Figure 2.9:** Gaussian mean of the primary vertex distribution along  $x$  for events with at least three tracks in a predefined target region per calendar day (half day). The error bars illustrate the Gaussian standard deviations.

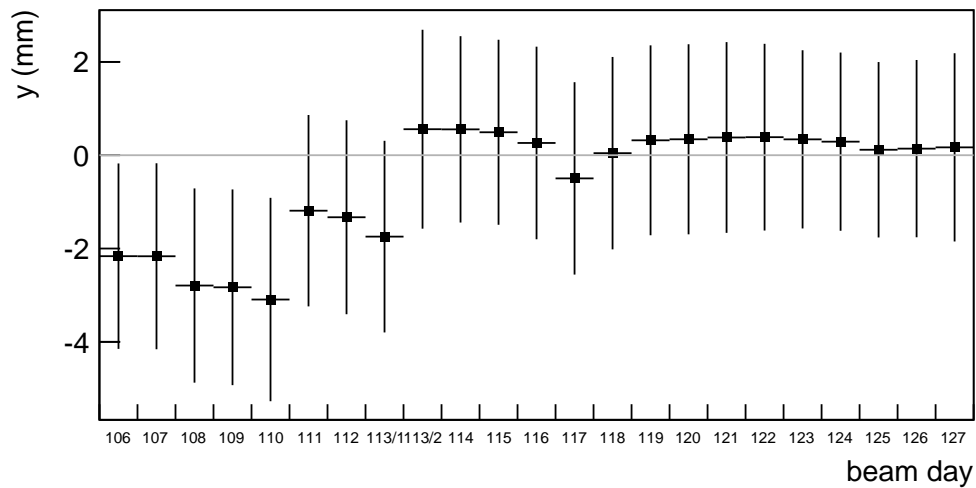


**Figure 2.10:** Gaussian mean of the primary vertex distribution along  $y$  for events with at least three tracks in a predefined target region per calendar day (half day). The error bars illustrate the Gaussian standard deviations.

### 2.3.3 Absolute Normalization

The results obtained in this work were absolutely normalized with help of the study of elastic p+p scattering in the same data set [Rus10]. Thereby, it was assumed that the ratio of measured elastic yield corrected for acceptance and efficiency to the elastic cross section will behave the same as for any other observable like in this case the  $K_S^0$ . With this, a factor  $F_{norm}^{exp}$  could be applied to obtain cross sections from the measured  $K_S^0$  yield  $N_{K_S^0}$  taking into account the mixing of the  $K^0$  (50%  $K_S^0$ , 50%  $K_L^0$ ):

$$\sigma_{exp}^{K^0} = 2 \cdot \sigma_{exp}^{K_S^0} = N_{K_S^0} \cdot F_{norm}^{exp}, \quad (2.3)$$

where the normalization factor  $F_{norm}^{exp}$  is defined as

$$F_{norm}^{exp} = \left( \frac{N_{el}^{acc}}{\sigma_{el}^{acc}} \cdot \frac{N_{exp}^{files}}{N_{el}^{files}} \cdot C_{el}^{acc-eff} \right)^{-1}, \quad (2.4)$$

with

$N_{el}^{acc}$  : number of elastic events in the HADES acceptance

$\sigma_{el}^{acc}$  : elastic cross section in the HADES acceptance

$N_{exp}^{files}$  : number of analyzed files

$N_{el}^{files}$  : number of analyzed files in the study of elastics

$C_{el}^{acc-eff}$  : acceptance and efficiency correction factor for elastic events

The numbers for the elastic parameters, which were obtained by a separate analysis [Rus10], and the number of files used in this analysis are summarized in Table 2.1 given that the number of events per file is constant. From the acceptance and efficiency correction of the elastic yield 7% of systematical uncertainties were found, which have to be considered in addition to the uncertainties determined in this work, when normalizing the data.

**Table 2.1:** Parameters for the absolute normalization of the HADES p+p data at 3.5 GeV kinetic beam energy. The numbers for the elastic events were determined in a separate analysis [Rus10].

$N_{el}^{acc}$	$\sigma_{el}^{acc}$ [mb]	$N_{exp}^{files}$	$N_{el}^{files}$	$C_{el}^{acc-eff}$
$2.321 \cdot 10^7$	0.16	12164	10417	1.6

## 2.4 Simulations

Apart from the transport models, that are also considered as simulations, but which have been already introduced in Section 1.6, this section will concentrate on the Monte Carlo

simulations generated with help of the Pluto event generator [F<sup>+</sup>07]. In general simulations are of great importance not only for the interpretation of the results, but they can also be used for the correction of the data to compensate losses due to limited detector acceptance and inefficiencies of the detector machinery, tracking algorithm and analysis procedure. The tools to perform these simulations are described in the next Section 2.4.1 and the simulated cocktail of reactions with a  $K_S^0$  in the final state for the mentioned acceptance and efficiency correction can be found in Section 2.4.2, which by the way allows to compare the data to different models and results of other experiments.

### 2.4.1 Simulation Tools

In the following the tools used to perform a full-scale simulation, which means the full chain of creating the simulation, processing it through HGeant, SimDST and the analysis, will be explained, which allows to correct the data for acceptance and efficiency effects. Thereby, the last two points obviously depend on the individual analyses applied for the experimental data and thus are discussed in the corresponding chapters 3 and 4.

#### 2.4.1.1 Pluto Event Generator

The Pluto framework is an event generator based on the Monte-Carlo algorithm and was designed for hadronic interactions at SIS and FAIR energy regimes (from pion production threshold to a few GeV per nucleon) [F<sup>+</sup>07, FGH<sup>+</sup>10]. The software package allows to simulate reactions according to build-in models, for example thermal models for heavy ion collisions, but it facilitates also the configuration of multi-reaction cocktails added up to an incoherent sum. The last option was deployed in this work to model elementary p+p reactions. Thereby, several parameters are adjustable by the user, which are amongst others individual cross sections, decay branching ratios and angular distribution models. Furthermore, the Pluto event generator offers the possibility to add particles and resonances with their properties (mass, width, decay) into the data base, if missing (e.g.  $K^*(892)$ ). The resonances included in Pluto such as  $\rho$ ,  $\Delta$ ,  $N^*$  and  $\Delta^*$  are described by a relativistic form of the Breit-Wigner distribution with a mass-dependent width:

$$g(m) = A \frac{m^2 \Gamma^{tot}(m)}{(M_R^2 - m^2)^2 + m^2 (\Gamma^{tot}(m))^2} \quad (2.5)$$

with

$m$  : running unstable mass

$M_R$  : static pole mass of the resonance

The mass-dependent width of the resonance is, thereby, calculated from the partial widths of each decay mode:

$$\Gamma^{tot}(m) = \sum_k^N \Gamma^k(m) \quad (2.6)$$

with

$\Gamma^{tot}(m)$  : mass-dependent width of the resonance

$\Gamma^k(m)$  : partial widths of the resonance

$N$  : number of decay modes

According to the user settings events are then generated with particles produced in the available phase space volume. Finally, the output of the Pluto framework delivers straight 3-vector information in the position space, which can be used for further analysis.

#### 2.4.1.2 HGeant

In order to simulate the interaction of the particles with the detector material, the events produced by the Pluto event generator were processed through the HGeant framework [HAD12], which is based on the Geant3 package developed at CERN [CER95]. To do so, all HADES detector components including mechanical structures and material properties were implemented in HGeant. Moreover, the framework allows to set the distribution of the event vertices within a defined target volume. In this work, since the experimental target was a cylindric tube filled with liquid hydrogen, a Gaussian distribution was chosen in the x-y-plane (perpendicular to the beam axis) to reflect the experimental beam profile, whereas in the z-axis, which is along the beam axis, a homogeneous distribution was required. During this step of the simulation, particles undergo scattering processes and secondary collisions and thereby lose energy on their way through the detector. They are, furthermore, bend in the magnetic field and eventually decay into secondary particles, which is the case for example for  $\Lambda$  or  $K_S^0$  particles. Ultimately, all interactions with the detector setup are stored providing automatically information on the geometrical acceptance.

#### 2.4.1.3 SimDST

At this point, the events have been produced with help of the Pluto event generator and passed through the HGeant framework to model the interaction of the particles with the detector material. However, also the electronic response of the detectors, their inefficiencies, noise and detector resolutions have to be simulated, which is done at this stage. The Geant information serve, thereby, as an input for this digitization process. The realistic particle hits are then treated the same way as the measured hits to form particle tracks meaning that the same track fitting algorithms are used and also the same track cuts. Finally, all the reconstructed track properties like the particle momentum, energy loss and others are stored in the SimDST (simulated data summary tape) according to the LVL1 trigger condition (Sec. 2.1.8). The simulated data are now in the same form as the stored experimental data and can be treated equally in the upcoming analysis steps to finalize the full-scale simulations.

### 2.4.2 The $K_S^0$ Pluto Cocktail

As already mentioned above, a Pluto simulation made out of a multi-reaction cocktail was used for comparison and for acceptance and efficiency correction in this work. Thereby, it was important to model also the LVL1 trigger efficiency, which required at least three hits detected in the META system to record the event. This is why, a simple simulation with help of the Geant particle gun generating single  $K_S^0$  mesons with random angle and momentum distributions was not applicable. Instead realistic reactions had to be simulated to account for the trigger efficiency. The cocktail is composed of 13  $K^0$  production channels, which are listed in Table 2.2 and cover the main sources of  $K_S^0$  formation in p+p collisions at the studied kinetic beam energy of 3.5 GeV with excess energies well above threshold.

**Table 2.2:** Simulated  $K^0$  production channels for the acceptance and efficiency correction. The cross sections  $\sigma_{ch}^{fit}$  at 3.5 GeV are determined by a fit with a cross section parametrization from [SC98] (Eq. 34) to experimental cross sections measured at other energies. The excess energies  $\varepsilon$  are calculated for p+p reactions at 3.5 GeV.

$K^0$ production channels	$\sigma_{ch}^{fit}$ [ $\mu\text{b}$ ]	$\varepsilon$ [MeV]
$p + p \rightarrow \Sigma^+ + p + K^0$	20.43	551
$p + p \rightarrow \Lambda + p + \pi^+ + K^0$	18.40	485
$p + p \rightarrow \Sigma^0 + p + \pi^+ + K^0$	12.38	408
$p + p \rightarrow p + n + K^+ + \bar{K}^0$	7.58	307
$p + p \rightarrow \Sigma(1385)^+ + p + K^0$	5.31	358
$p + p \rightarrow \Lambda + n + \pi^+ + \pi^+ + K^0$	5.08	344
$p + p \rightarrow \Sigma^+ + n + \pi^+ + K^0$	4.53	410
$p + p \rightarrow \Lambda + \Delta^{++} + K^0$	4.47	331
$p + p \rightarrow \Lambda + p + \pi^+ + \pi^0 + K^0$	4.46	350
$p + p \rightarrow \Sigma^+ + p + \pi^0 + K^0$	4.06	416
$p + p \rightarrow \Sigma^- + p + \pi^+ + \pi^+ + K^0$	3.75	264
$p + p \rightarrow \Sigma^+ + p + \pi^+ + \pi^- + K^0$	2.26	272
$p + p \rightarrow p + p + \pi^+ + K^- + K^0$	2.02	169

Although an analysis in two kinematical self-contained variables would permit a model independent acceptance correction, a realistic model was preferable, which could be compared to and thus allow for interpretations of the observed data. Therefore, the cross sections quoted for each reaction in Table 2.2 were implemented in the simulation. Since these cross sections were not measured at the presented beam energy, a parametrization by Sibirtsev and Cassing [SC98] was used to fit existing yield measurements of the individual channels and by that to estimate the expected cross sections at  $E_{kin} = 3.5$  GeV. After converting the parametrization from the dependency on the square of the invariant collision energy  $s$  to an equation of  $E_{kin}$  in p+p collisions, it reads as follows:

$$\sigma^{ch} = a \left( 1 - \frac{E_0^{ch} + 2m_p}{E_{kin} + 2m_p} \right)^b \left( \frac{E_0^{ch} + 2m_p}{E_{kin} + 2m_p} \right)^c \quad (2.7)$$

with

$\sigma^{ch}$  : cross section of a specific channel

$E_0^{ch}$  : channel dependent threshold of the kinetic beam energy

$E_{kin}$  : kinetic beam energy

$m_p$  : mass of the proton

$a, b$  and  $c$  : fit parameters

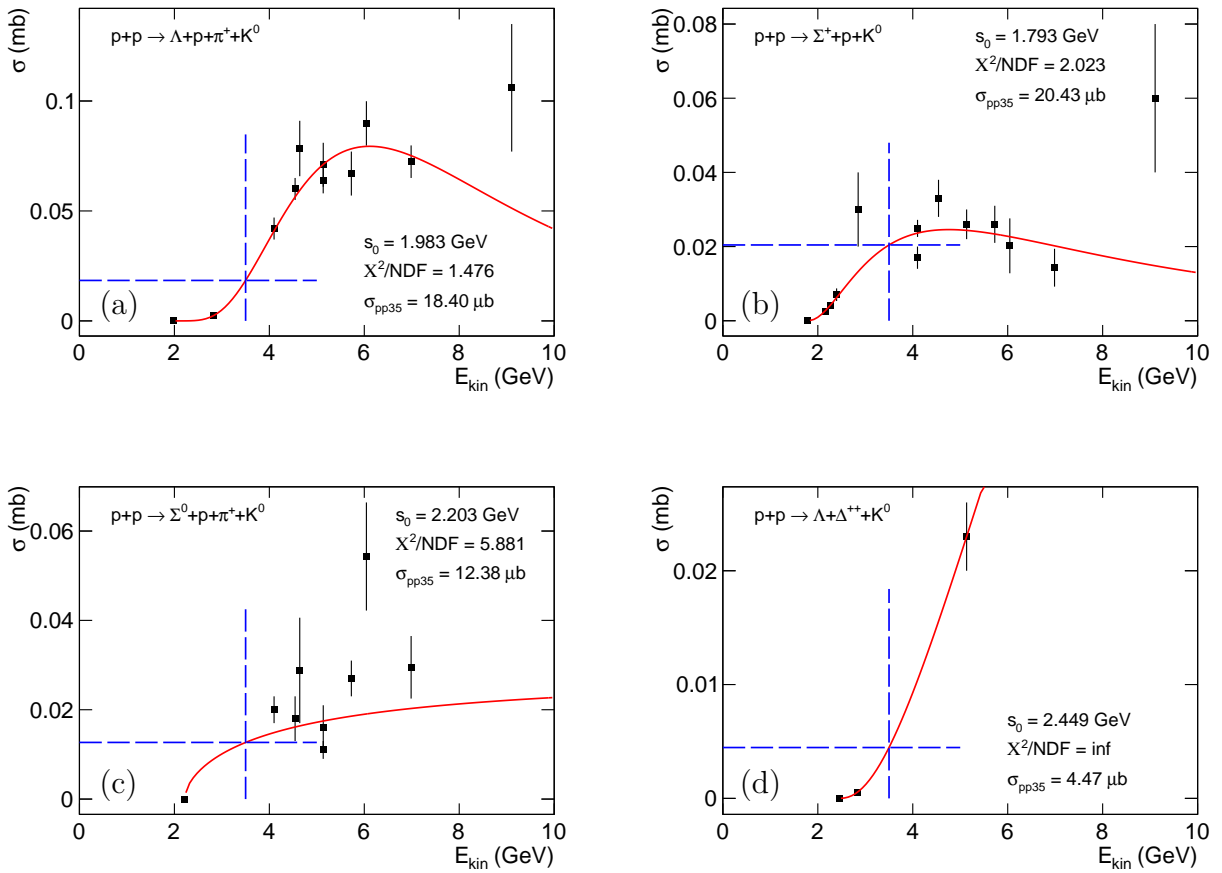


**Figure 2.11:** Cross sections measured by different experiments as a function of the kinetic energy of the incoming proton beam for the listed reactions. The data points are taken from Landolt-Börnstein [MS88] and complemented with recent data [N<sup>+</sup>07, AB<sup>+</sup>12]. The red solid curves are fits corresponding to a cross section parametrization (Eq. 2.7) derived from Equation 34 in [SC98]. The blue dashed lines indicate suggested cross sections by the fit at  $E_{kin} = 3.5$  GeV, which are quoted in the legends as  $\sigma_{pp35}$ .

The parametrization, which was fitted to experimental data, is shown as an example for four reactions in Figure 2.11. The measurements are plotted as black squares, whereas the fit function is depicted as a red curve. Moreover, the dashed blue lines mark the estimated cross sections for a kinetic beam energy of 3.5 GeV. One has to mention here, that the cross sections plotted for the reaction  $\Lambda/\Sigma^0 + p + \pi^+ + K^0$  include contributions of the direct non-resonant production as well as of resonant reactions like  $\Lambda/\Sigma^0 + \Delta^{++} + K^0$ , which in the end lead to the same final states. The reason for that can be deduced from the plot in panel (d), which contains only two measurements for the channel  $\Lambda + \Delta^{++} + K^0$ , because often the discrimination between non-resonant and resonant channels was not made or was not possible. For the reaction  $\Sigma^0 + \Delta^{++} + K^0$  the situation is even worse, as no experiment was performed exclusively for this channel before. From all four figures one can, furthermore, recognize the rather large uncertainties of the cross sections measured at higher beam energies, since most of these data stem from bubble chamber experiments with lower statistics (summarized in [MS88]). However, this circumstance results automatically in larger uncertainties of the fit, which need to be kept in mind. The low energy regime is mostly covered by the recent ANKE and COSY-TOF experiments and show much smaller error bars [N<sup>+</sup>07, AB<sup>+</sup>12].

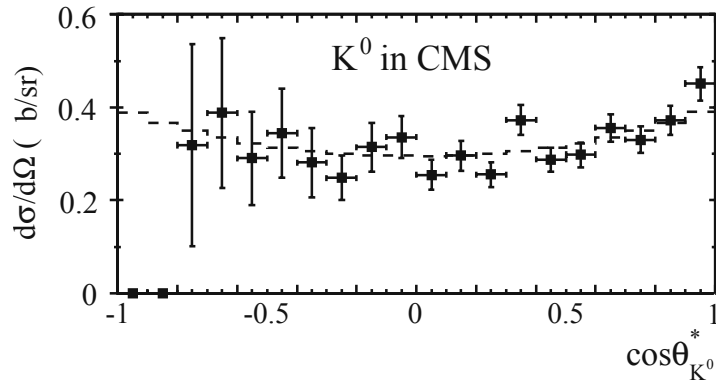


**Figure 2.12:**  $K^0$  angular distribution in the center-of-mass for the reaction  $p + p \rightarrow \Sigma^+ + p + K^0$  measured by the COSY-TOF Collaboration at  $p_{beam} = 3059$  MeV/c ( $E_{kin} = 2.26$  GeV). The dashed line shows a parametrization using a Legendre polynomial function, which was implemented in this analysis. The Figure is adopted from [AB<sup>+</sup>12].

In addition to the estimated cross sections, the angular distribution of the reaction  $p + p \rightarrow \Sigma^+ + p + K^0$  was adopted from [AB<sup>+</sup>12], even if that measurement was carried out at a lower beam momentum of  $p_{beam} = 3059$  MeV/c corresponding to  $E_{kin} = 2.26$  GeV. Such an angular distribution can be described by a Legendre polynomial function, which allows to express the anisotropy in few parameters. A more detailed explanation will follow in Section 3.2.3. The parameters extracted for the  $K^0$  in the aforesaid channel are:  $A_0 \approx 330$  nb/sr,  $A_1 \approx -10$  nb/sr and  $A_2 \approx 109$  nb/sr, while the ratio  $A_2/A_0 \approx 0.330$  points at a slight anisotropic production of the  $K^0$  mesons, which is also visible in Figure 2.12. Here, the angular distribution of the  $K^0$  is plotted in the center-of-mass together with the

Legendre polynomial parametrization (dashed line) as it was determined by the COSY-TOF Collaboration [AB<sup>+</sup>12].

The  $K^0$  Pluto cocktail with the settings described above covers the full available phase space in the given p+p reaction. That phase space distribution is illustrated in Figure 2.13 in terms of the  $K_S^0$  transverse momentum  $p_t$  and center-of-mass rapidity  $y_{cm}$ . Thereby, panel (a) contains the plot of the Pluto output without any further analysis and panel (b) the distribution after full-scale simulation including  $K_S^0$  secondary vertex cuts listed in Table 3.1. The red dotted lines correspond to the indicated momenta in the  $p_t$ - $y_{cm}$  plane. From the pure Monte Carlo simulation a very sharp cutoff is visible at  $p \approx 770$  MeV/c, which is related to the easiest accessible channel  $p + p \rightarrow \Sigma^+ + p + K^0$ . This limit is washed out by the full-scale analysis due to several effects like the detector resolution,  $K_S^0$  reconstruction efficiency, resolution of the primary vertex calculation, PID misidentification and others. Furthermore, the distribution, which is well centered around mid-rapidity ( $y_{cm} = 0$ ) in panel (a), is shifted slightly to backward rapidities ( $y_{cm} < 0$ ) in panel (b), while forward rapidities are limited to  $y_{cm} < 0.5$ , which is related to the acceptance of the HADES detector system. The spectrum showing the simulation processed through the full analysis chain is, in addition, not that homogeneous anymore, but rather looks like two oval shaped distributions, which overlap. This phenomenon is attributed to the fact that the reconstruction efficiency of the various channels are different, mainly because of the multiplicity of the final states. Thereby, the reactions with less final states populate higher  $p_t$  regions than many-body channels, which are easier to detect and lead to the enhancement at  $p_t \approx 100 - 300$  MeV/c.

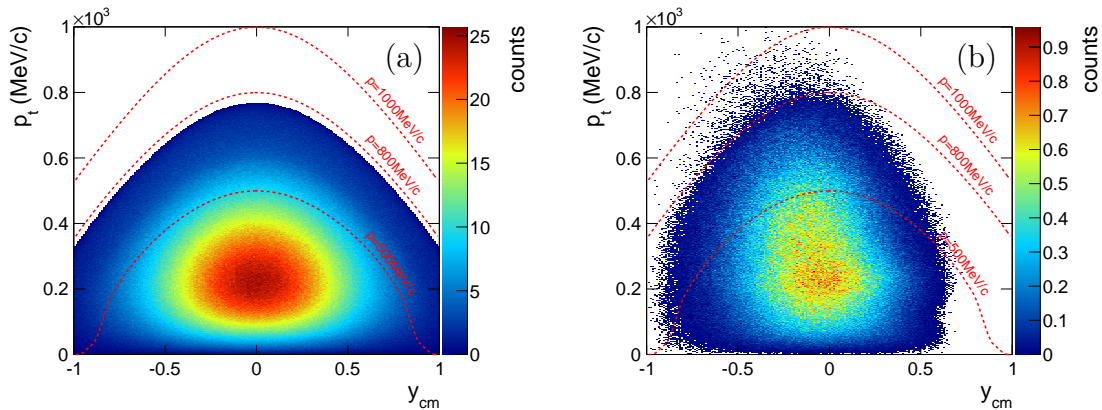


**Figure 2.13:**  $K_S^0$  transverse momentum  $p_t$  versus center-of-mass rapidity  $y_{cm}$  distribution of the simulated Pluto/Monte Carlo cocktail of 13  $K_S^0$  production channels weighted with the cross sections quoted in Table 2.2. Panel (a) shows the unfiltered simulation and panel (b) the full-scale simulation with  $K_S^0$  secondary vertex cuts (Table 3.1).

The reconstructed primary vertex of the  $K^0$  cocktail, which has went through the full analysis chain, is illustrated in Figure 2.14, once in the x-y-plane (panel (a)) and once in the x-z-plane (panel (b)). The primary vertex was calculated the way as it was described in Section 2.3.1 for  $K_S^0$  events. When comparing these distributions with the ones plotted for experimental data in Figure 2.7, quite similar spectra are observed despite the multiple

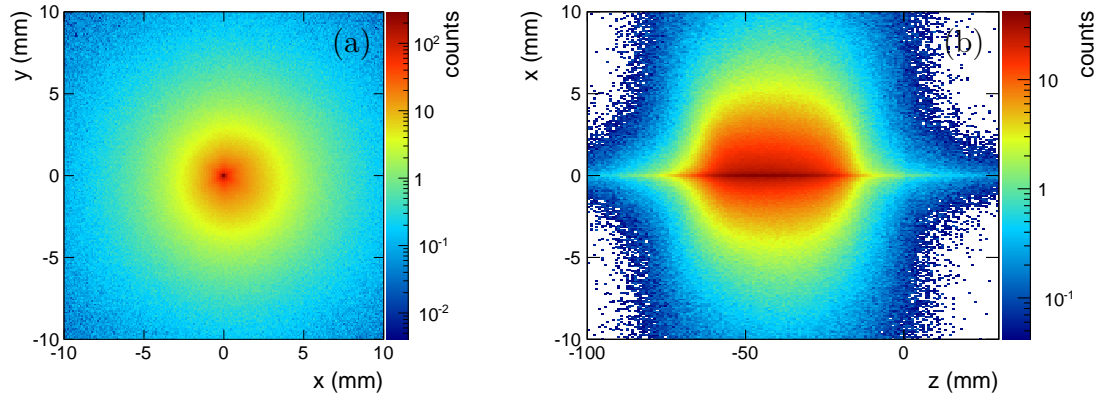


**Figure 2.14:** Primary vertex distributions in the x-y- (panel (a)) and in the x-z-plane (panel (b)) for  $\pi^+\pi^-$ -pairs of the full-scale simulation consisting of the 13 Pluto/Monte Carlo  $K_S^0$  channels listed in Table 2.2.

peaks in the measurement due to the beam shifts (see Sec. 2.3.2). Furthermore, the experimental distribution is more noisy, which is especially visible in the x-z-representation. This observation can be attributed to the presence of much more background events in the experimental data originating from non-strange reactions and wrong combinations of the  $\pi^+$  and the  $\pi^-$  to form a  $K_S^0$ . Nevertheless, the agreement is good enough to perform an acceptance and efficiency correction with this model.



# 3 The Inclusive $K_S^0$ production in p+p @ 3.5 GeV

The forthcoming chapter deals with the study of the inclusive  $K_S^0$  production in p+p reactions, which is not only interesting in terms of its total cross section at the measured kinetic energy of 3.5 GeV, but can also give insight in the particle production mechanism in an elementary system, where no effects such as nuclear scattering or potential effects are expected. For this reason, such elementary measurements can be used as a reference to understand the mentioned effects in more complicated systems as p+A or heavy ion collisions and, moreover, put up constraints for theoretical calculations or serve as a cross check.

To display the complete kinematics of a inelastic production process, the analysis has to be carried out in two kinematical independent observables, which can be for example  $p_{cm}-\cos\Theta_{cm}$  or  $p_t-y$ . In the following sections details of the analysis procedure are described to explain, how these distributions were obtained. Furthermore, a self-consistency check was performed with the aim to put this analysis on solid ground (Sec. 3.3). At the end of this chapter (Sec. 3.5) the results are presented in comparison to various transport models (HSD [CB99], UrQMD [B<sup>+</sup>98] and GiBUU [B<sup>+</sup>12]) in order to identify possible disagreements, which would point to missing experimental informations on kaon creation used as an input in the calculations and a need for a more detailed understanding of the exclusive  $K_S^0$  production in p+p reactions. The latter topic is addressed in the next Chapter (Chap. 4).

## 3.1 Analysis Procedure

The inclusive analysis of the  $K_S^0$  meson ( $p + p \rightarrow K_S^0 + X$ ) mainly exploits its nature of being a short-lived particle. This property allowed the reconstruction of the kaon via its charged decay mode ( $K_S^0 \rightarrow \pi^+ + \pi^-$  with  $BR = 69.20 \pm 0.05\%$ ) making use of the invariant mass technique, which was necessary, since the HADES setup is not suited for the detection of neutral particles. For the invariant mass technique all  $n$  decay products have to be detected, as the 4-momentum of the reconstructed mother particle ( $E, \vec{p}$ ) can be determined by the sum of the 4-momentum of the daughter particles ( $E_i, \vec{p}_i$ ), thus, allowing to calculate the mass of the mother particle:

$$m_{inv} = \frac{1}{c^2} \sqrt{E^2 - \vec{p}^2 c^2} = \frac{1}{c^2} \sqrt{\left( \sum_{i=1}^n E_i \right)^2 - \left( \sum_{i=1}^n \vec{p}_i \right)^2 c^2}. \quad (3.1)$$

Furthermore, the specific decay topology, which is explained in the following section, can be utilized to reject background events. Finally, the extraction of the  $K_S^0$  yield can be performed in terms of kinematical observables to learn about the  $K_S^0$  production mechanisms.

### 3.1.1 $K_S^0$ Reconstruction

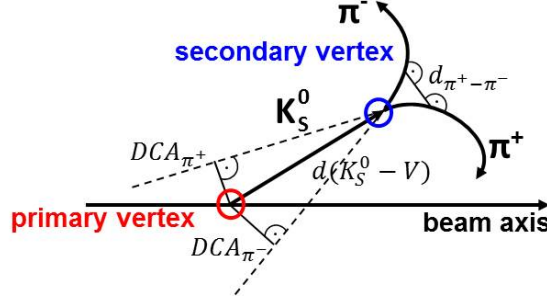


**Figure 3.1:** Sketch of the  $K_S^0$  decay topology for the breakup into  $\pi^+$  and  $\pi^-$  with the secondary vertex cut variables  $d_{\pi^+-\pi^-}$ ,  $d(K_S^0 - V)$ ,  $DCA_{\pi^+}$  and  $DCA_{\pi^-}$ .

For the reconstruction of short-lived neutral kaons only reactions were used, which survived a rough primary vertex cut of  $17 \times 17 \text{ mm}^2$  in the x-y-plane with respect to the corrected beam axis (see Section 2.3.2) and 60 mm in the direction of the beam. The calculation of the primary vertex is explained in Section 2.3.1. This cut should reject off-target events, for example from the beam pipe. Thanks to the charged decay of the  $K_S^0$ , a reconstruction via its daughter particles  $\pi^+$  and  $\pi^-$  was possible, which were identified through a PID cut on the MDC energy loss information (see Section 2.2).

**Table 3.1:** Final off-vertex cuts for the  $K_S^0$  reconstruction via its charged decay pions.

Off-vertex cut	d [mm]
$d_{\pi^+-\pi^-}$	< 7
$d(K_S^0 - V)$	> 25
$DCA_{\pi^+}$	> 7
$DCA_{\pi^-}$	> 7

In order to suppress combinatorial background, further cuts had to be applied on the decay topology of the  $K_S^0$ , which is sketched in Figure 3.1. Due to a considerable lifetime, which leads to a  $c\tau$  of around 2.68 cm, off-vertex or secondary vertex cuts were applicable. In particular, four topological cuts were defined:

1.  $d_{\pi^+-\pi^-}$ : distance between the two pion tracks
2.  $d(K_S^0 - V)$ : distance between the primary reaction and the secondary decay vertex

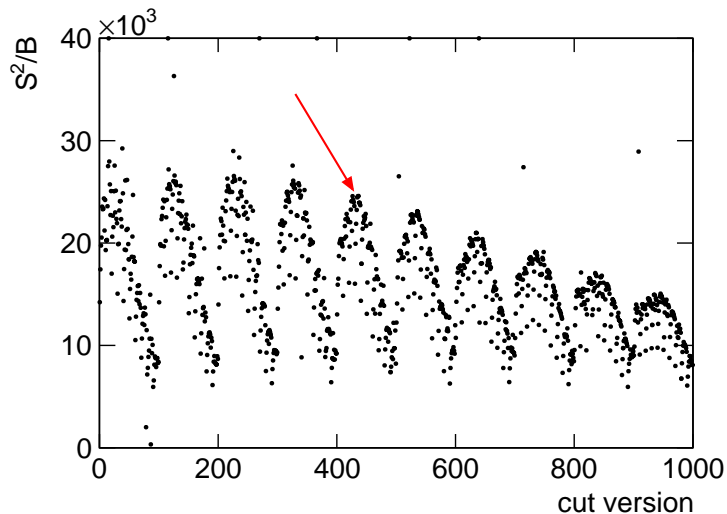


**Figure 3.2:**  $S^2/B$  ( $S$  = signal,  $B$  = background) ratio depending on the cut version, which stands for a specific off-vertex cut combination. The encoding of the cut version is realized according to Eq. 3.2. The red arrow points at the selected cut version.

3.  $DCA_{\pi^+}$ : distance of closest approach of the  $\pi^+$  track with respect to the primary vertex
4.  $DCA_{\pi^-}$ : distance of closest approach of the  $\pi^-$  track with respect to the primary vertex

While the first cut should enhance the probability that the two pions originate from one vertex, namely the  $K_S^0$  decay vertex, the second and third cuts should filter out pions coming from the primary vertex favoring displaced secondary vertices. The optimal combination of these cuts were determined by maximizing  $S^2/B$  in the invariant mass spectrum of the two pions, where  $S$  is related to the  $K_S^0$  signal and  $B$  to the background inside the  $3\sigma$  signal region. This observable was chosen on the one hand to achieve a good  $S/B$  ratio, while at the same time trying to keep as much signal as possible. For this purpose, the invariant mass spectra were fitted with the sum of two Gaussians for the signal and a third order polynomial and a Landau function for the description of the background. The additional Landau function was in particular needed to describe bump-like background shapes, when looking at the invariant mass distribution of specific kinematic regions. Moreover, due to scattering effects a single Gauss function was not sufficient for the reproduction of the signal and so, when speaking about  $\sigma$  (e.g.  $3\sigma$  signal region) the amplitude weighted average of the standard deviations from the two Gaussians is meant. In the end, around thousand cut combinations were checked leading to the  $S^2/B$  distribution shown in Figure 3.2. The x-axis in this plot contains the encoding of the cut versions according to following formula:

$$CV = 100 \cdot N_{DCA_{\pi}} + 10 \cdot N_{d(K_S^0-V)} + 1 \cdot N_{d_{\pi^+-\pi^-}} \quad (3.2)$$

with

$CV$  : cut version

$N_{DCA_{\pi}}$  : numbering of a specific  $DCA_{\pi^+}$  and  $DCA_{\pi^-}$  cut value

$N_{d(K_S^0-V)}$  : numbering of a specific  $d(K_S^0 - V)$  cut value

$N_{d_{\pi^+-\pi^-}}$  : numbering of a specific  $d_{\pi^+-\pi^-}$  cut value

Thereby, the numberings range from 0 to 9 and symbolize the variation over the particular cut variables. The numbering of the cuts  $DCA_{\pi^+}$  and  $DCA_{\pi^-}$  were combined, since the values for these two cuts were always kept equal. The argument for this originates in the very similar mass of the  $\pi^+$  and the  $\pi^-$ . Some scattered measurements, which do not follow the general trend, can be neglected, since they are related to cases, in which the invariant mass fits failed. The cuts were varied as follows:  $d_{\pi^+-\pi^-} = 3 - 12$  mm with  $\Delta d_{\pi^+-\pi^-} = 1$  mm,  $d(K_S^0 - V) = 10 - 55$  mm with  $\Delta d(K_S^0 - V) = 5$  mm and  $DCA_{\pi^+/-} = 3 - 12$  mm with  $\Delta DCA_{\pi^+/-} = 1$  mm. Ultimately, the cut conditions were chosen from the maximum in the peak between cut version 400 and 499 ( $DCA_{\pi^+/-} > 7$  mm) indicated by the red arrow in Figure 3.2, where all the fits were stable and successful. The values of the final cuts are summarized in Table 3.1, while the corresponding invariant mass spectrum is depicted in Figure 3.3 panel (a) together with the background subtracted distribution in panel (b).

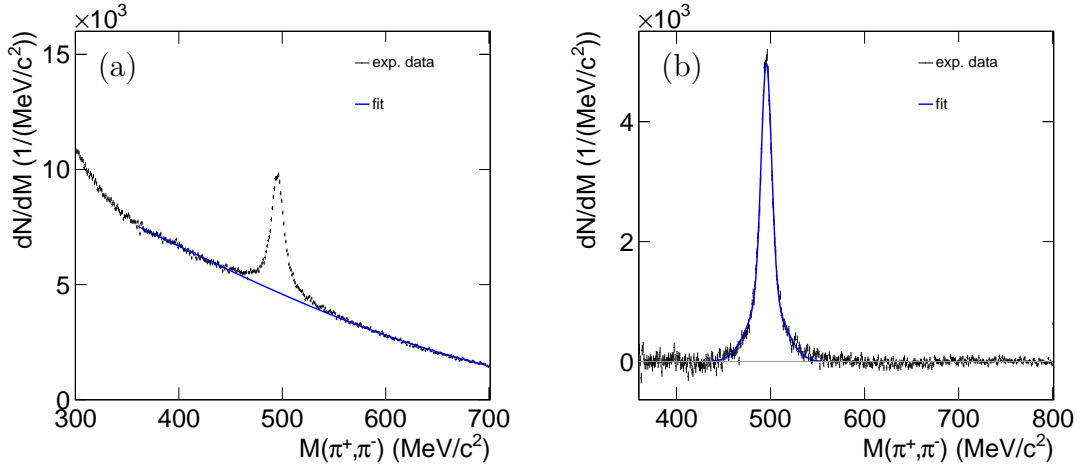


**Figure 3.3:** Invariant mass distribution of  $\pi^+$  and  $\pi^-$  candidates with the usage of primary vertex and secondary vertex cuts (Table 3.1). Panel (a) shows the spectrum fitted with the sum of two Gaussians (here, the amplitudes were set to zero for better visibility), a Landau and a polynomial of the third order (blue). Panel (b) shows the background subtracted spectrum fitted with two Gaussians (blue). The extracted quantities are:  $\langle m_{K_S^0} \rangle = 495.6 \pm 0.1$  MeV/ $c^2$ ,  $\langle \sigma_{K_S^0} \rangle = 8.3 \pm 0.2$  MeV/ $c^2$ ,  $N_{K_S^0} = 95226 \pm 574$  and  $S/B = 0.41$ .

From a fit as mentioned before (blue lines in Fig. 3.3), a signal of  $95226 \pm 574$  and a  $S/B$  ratio of 0.41 were obtained in the  $3\sigma$  region of the peak. The mass of the  $K_S^0$  was

determined to be  $\langle m_{K_S^0} \rangle = 495.6 \pm 0.1 \text{ MeV}/c^2$  with a  $\langle \sigma_{K_S^0} \rangle = 8.3 \pm 0.2 \text{ MeV}/c^2$ . With the rather large number of  $K_S^0$  also two-dimensional analyses are possible as roughly shown in Figure 3.4. Here, the phase space distribution of the  $K_S^0$  candidates is shown in terms of  $p_t$ - $y_{cm}$ . In panel (a) only the final secondary vertex cuts were applied, whereas in panel (b) additionally a  $3\sigma$   $K_S^0$  mass cut was used. A comparison to the corresponding simulated distributions in Figure 2.13 show that almost the entire  $K_S^0$  production phase space can be studied with the HADES setup. Only at very forward rapidities ( $y_{cm} > 0.6$ ) a cut-off is visible in the experimental spectra due to the HADES acceptance. Furthermore, one can see from the plotted momentum lines (red dashed) the maximum available momentum of around 770 MeV/c for the  $K_S^0$  production calculated from the easiest accessible channel  $p + p \rightarrow \Sigma^+ + p + K_S^0$ , when the  $K_S^0$  mass cut is applied, although still more than half of that statistics can be attributed to background. Since the maximum available momentum of the  $K_S^0$  is rather low, one can, furthermore, assume that no bias was introduced by the limited PID cuts of pions with  $p < 1000 \text{ MeV}/c$ .

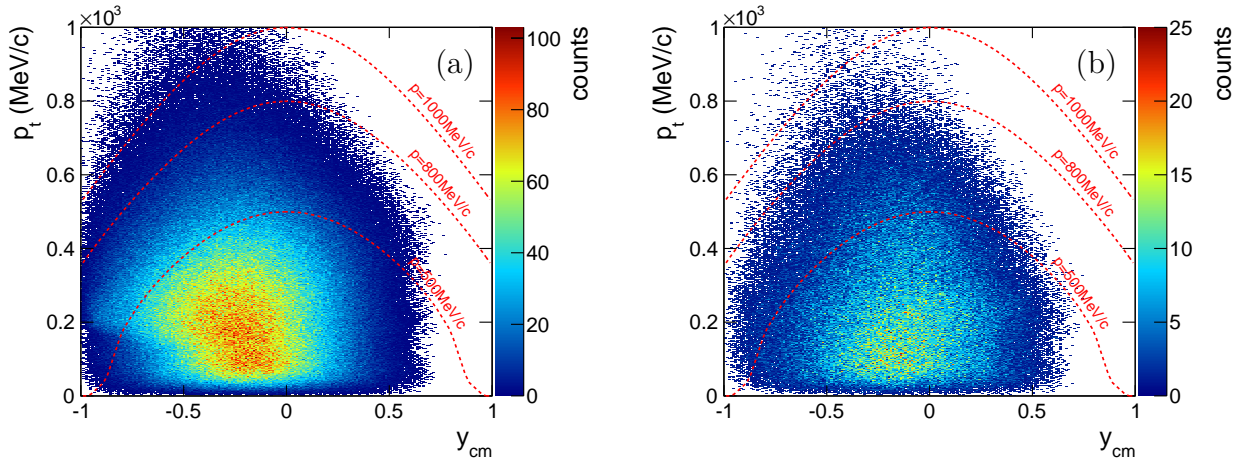


**Figure 3.4:** Transverse momentum  $p_t$  versus center-of-mass rapidity  $y_{cm}$  spectra for  $\pi^+\pi^-$  pairs. The red dotted lines indicate the  $\pi^+\pi^-$ -momentum at 500, 800 and 1000 MeV/c. Panel (a) shows the distribution only with primary vertex and secondary vertex cuts (see Table 3.1). The spectrum in panel (b) includes a cut on the  $K_S^0$  mass within  $3\sigma$  (from the fit in Fig. 3.3).

### 3.1.2 Acceptance and Efficiency Correction

As already indicated above, the measurement was limited by the geometrical acceptance of the HADES setup (Sec. 2.1). This confined acceptance is caused not only by construction considering for instance the uncovered region in the forward direction ( $\Theta < 15^\circ$ ) but includes also the influence by the detector material, that might cause particle scattering in the mechanical structures. For the inclusive analysis of the short-lived  $K_S^0$  exploiting its decay into  $\pi^+$  and  $\pi^-$ , the losses at small polar angles are not that pronounced, since the pions have opposite charge and might be bent back into the detection region by the magnetic field. Nevertheless, there is still some probability that one of the pions or even

both pions could not be detected, because they flew into the forward hole or to polar angles larger than  $85^\circ$  or they have been stopped or scattered too much in the detector material. In the case of an exclusive measurement as discussed in Chapter 4 the acceptance for an event drops drastically, since besides the two decay pions additionally further final state particles of the reaction of interest have to be detected.

Furthermore, losses need to be taken into account, which originate in the inefficiency of the detector electronics or the analysis procedure. This implies sources like the detector response, the trigger decision, the tracking algorithm and also the final analysis procedure including the particle identification (PID) and the applied cuts on the primary and secondary vertex distributions. All these inefficiencies perturb and modify the resulting experimental spectra in such a way that hardly any physics can be drawn from them. A correction of the data in terms of acceptance and efficiency is, therefore, crucial and allows not only to interpret the experimental findings but also to perform comparisons with other experiments and theoretical predictions.

The correction for the effects explained above were carried out with help of simulations and specific simulation tools. The simulation consists of a Monte Carlo cocktail of 13  $K^0$  production channels, which was introduced in Section 2.4.2, and covers the complete available phase space in the studied p+p reaction at  $E_{kin} = 3.5$  GeV. To minimize statistical fluctuations a large amount of events (10 million per channel) was generated, which basically allowed to ignore this kind of uncertainties. The influences of the detector acceptance and the various efficiencies were modeled by means of the simulation tools, which were explained in Section 2.4.1. Thereby, acceptance issues were treated within the HGeant framework and efficiency effects caused by the detector response, tracking and trigger decision were considered in the SimDST production step. In addition, the particle identification for the simulation was adjusted such to select a particle species as efficient as in the experimental case. A detailed description on this method can be found in Section 2.2. All other efficiencies were taken into account by processing the simulation through the same analysis procedure as foreseen for the experimental data. This way, a full-scale simulation was obtained, which suffered the same experimental losses. Since the correction should be model independent, to avoid the need of a perfectly real simulation, this operation had to be carried out in two kinematical independent observables (e.g.  $p_t$ - $y_{cm}$  or  $\cos\Theta_{cm}$ - $p_{cm}$ ). Thus, knowing the kinematical distributions of the initial unfiltered simulation and of the final full-scale simulation it was possible to calculate a correction matrix for the experimental spectra according to:

$$D_{corr}(v_1, v_2) = \frac{D_{fin}(v_1, v_2)}{D_{in}(v_1, v_2)} \quad (3.3)$$

with

$D_{corr}$  : acceptance and efficiency correction matrix

$D_{in}$  : distribution of the initial unfiltered simulation

$D_{fin}$  : distribution of the final full-scale simulation

$v_1$  and  $v_2$  : two kinematical independent variables

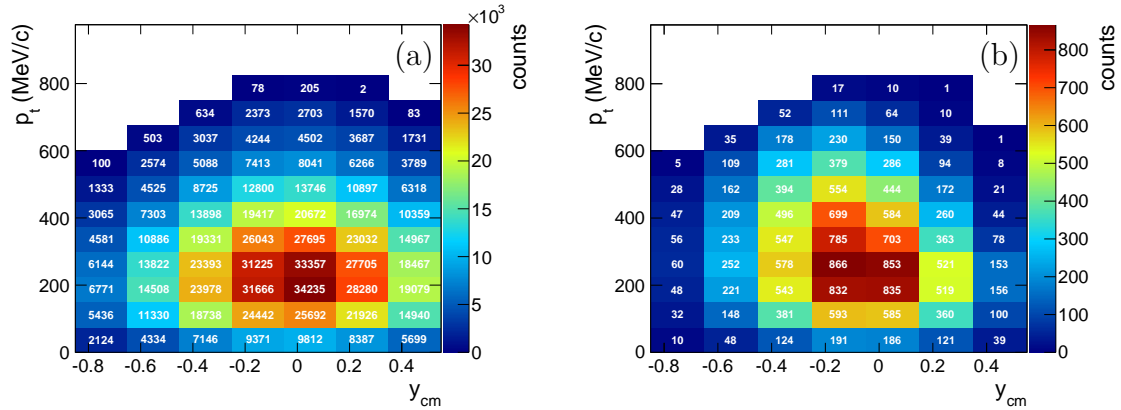


**Figure 3.5:**  $K_S^0$   $p_t$ - $y_{cm}$  distribution of the  $K_S^0$  Pluto/Monte Carlo simulation (Table 2.2) binned for acceptance and efficiency correction. Panel (a) shows the unfiltered simulation and panel (b) the full-scale simulation.

As an example the simulated distributions are depicted in Figure 3.5 in the two-dimensional  $p_t$ - $y_{cm}$  representation. Panel (a) shows the unfiltered distribution of the  $K^0$  cocktail, whereas panel (b) contains the spectrum after the full-scale analysis. The binning visible in the plots corresponds to the chosen binning in the experimental analysis. Moreover, the distributions are only shown for the measured kinematical regions, since the correction can only take place inside the acceptance.

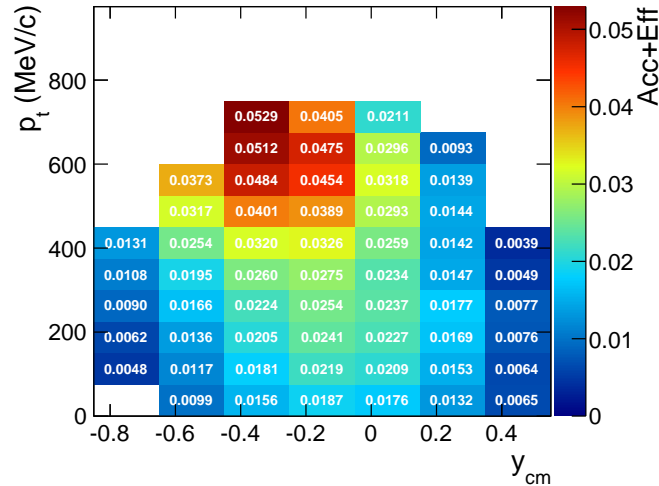


**Figure 3.6:**  $K_S^0$   $p_t$ - $y_{cm}$  acceptance and efficiency correction matrix of the  $K_S^0$  Pluto/Monte Carlo simulation (Table 2.2) derived from the ratio of the distributions in Figure 3.5, panel (b) divided by panel (a).

By comparing the numbers for each bin or even just the z-scales, one can already recognize a huge drop of the yield, when going from the initial to the final distribution. This observation is reflected in the acceptance and efficiency correction matrix, which was obtained through the division of the final by the initial spectrum and is illustrated in Figure 3.6. Here, one can see that the maximal acceptance and efficiency for a measured  $K_S^0$  is of the order of 5.3%, while the average is around 2.2%. As expected a quite large correction is needed. Furthermore, the matrix is not flat or homogeneous over the measured phase space, but  $K_S^0$  mesons with larger transverse momenta and rather negative center-of-mass rapidities have a higher chance to be reconstructed, which is mainly due to the HADES acceptance. Finally, by multiplying this correction matrix to the experimental distribution an unbiased spectrum is obtained, which can be used for physics interpretations.

**Table 3.2:** The six off-vertex cut combinations resulting from a variation of each cut by  $\pm 20\%$  for the determination of systematic uncertainties.

Cut combination	$d_{\pi^+\pi^-}$ [mm]	$d(K_S^0 - V)$ [mm]	$DCA_{\pi^+}$ & $DCA_{\pi^-}$ [mm]
	<	>	>
1	8.4	25.0	7.0
2	5.6	25.0	7.0
3	7.0	30.0	7.0
4	7.0	20.0	7.0
5	7.0	25.0	8.4
6	7.0	25.0	5.6

### 3.1.3 Systematical Uncertainties

Every result of experimental measurements comes along with systematic uncertainties, which can be minimized by calibrating the measurement system as precise as possible and in our case also by choosing analysis methods that are less sensitive to perturbations. With the given calibration precision of the HADES setup the analysis was left with the uncertainties related to the fitting procedure of the  $K_S^0$  invariant mass spectra for the different cuts on the displaced decay vertex of the  $K_S^0$  candidate. This procedure was not automated, since the unstable background shape, which could change from a bump structure to a valley-like shape depending on the selected kinematic region, required a manual adjustment of the fitting parameters. Here, mainly the fit limits were tuned, but also the allowed range of the standard deviations from the two Gaussians. The extent of the systematic uncertainties from these sources were evaluated by a variation of the off-vertex cuts and by refitting the resultant invariant mass spectra. In the variation of the above introduced secondary vertex cuts every cut was modified by  $\pm 20\%$  while keeping the other cuts at the standard value quoted in Table 3.1. In this way, six additional cut combinations were tested, that are listed in Table 3.2. By correcting the data with the help of simulations, also the systematic uncertainties stemming from the model were taken into account. In total around 9%-15% of the  $K_S^0$  yield could be attributed to systematical uncertainties.

## 3.2 Results and Discussion

### 3.2.1 $p_t$ - $y$ Distributions

As mentioned above the statistics of reconstructed  $K_S^0$  is large enough to perform double differential analyses, thus, covering the full kinematics of the  $K_S^0$  production and allowing a model independent acceptance and efficiency correction of the data. One possibility is to study the yield as a function of transverse momentum  $p_t$  and of rapidity  $y$ , which is defined in the following equation:

$$y = \frac{1}{2} \ln \frac{E + p_l}{E - p_l}, \quad (3.4)$$

with  $E$  being the energy of the considered particle and  $p_l$  being the momentum component parallel to the beam direction. The transverse momentum reflects the momentum component perpendicular to the  $z$ -axis ( $p_t^2 = p_x^2 + p_y^2$ ), which is usually defined as the beam direction. Therefore, this momentum component is decoupled from the boost transferred by the beam itself. This is of particular importance in the study of in-medium effects, which take place in the MeV regime and hence are very small compared to the analyzed beam energy of 3.5 GeV.

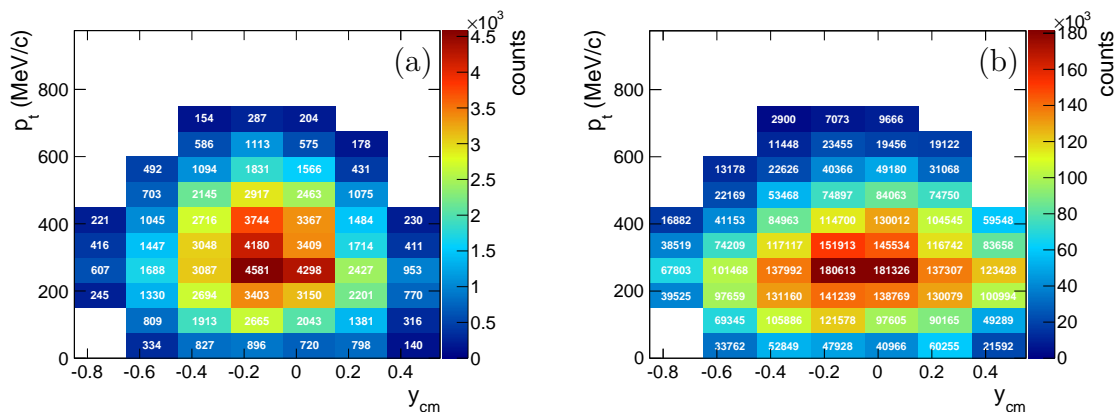


**Figure 3.7:** Uncorrected  $p_t$  versus  $y_{cm}$  distribution of  $K_S^0$  in panel (a). Acceptance and efficiency corrected distribution in panel (b).

Here,  $p_t$  was studied in the range 0–750 MeV/c in a binning of 75 MeV/c, which corresponds to ten bins, and  $y_{cm}$  (rapidity in the center-of-mass) was investigated from  $-0.65$  to  $0.55$  with a bin width of 0.20 (six bins). The kinematic ranges were chosen such to cover the whole HADES reconstruction acceptance as depicted in Figure 3.4 panel (b), while the binning was adjusted in that way that the statistics per bin was sufficient for the analysis. To retrieve the  $p_t$ - $y$  distributions,  $\pi^+\pi^-$ -invariant mass spectra were plotted for the specific  $p_t$ - $y$  bins and fitted with the same function as explained in Section 3.1.1 to determine the  $K_S^0$  yields. Figure 3.7 panel (a) shows the uncorrected yields in the chosen binning. These  $p_t$ - $y$  yields were then corrected for acceptance and efficiency with the help of Monte Carlo

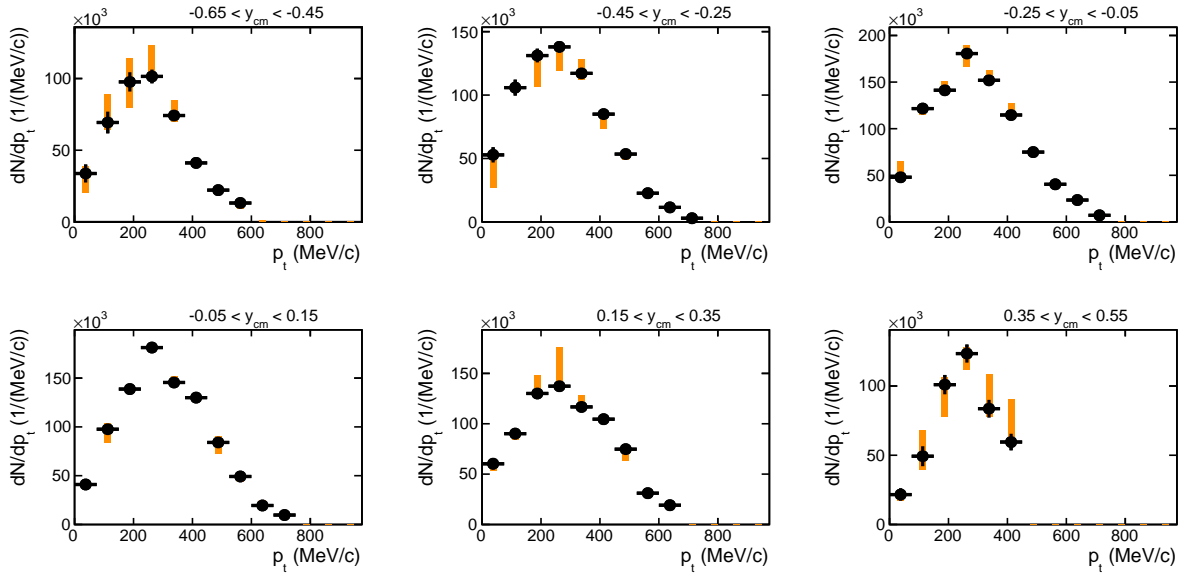


**Figure 3.8:** Acceptance and efficiency corrected transverse momentum  $p_t$  spectra of  $K_S^0$ 's in six center-of-mass rapidity bins. The black lines in the y-direction indicate statistical uncertainties and the orange bars correspond to systematic ones.

simulations as explained in Section 3.1.2, where one can find the correction matrix in Figure 3.6. These corrected spectra are depicted in Figure 3.7 panel (b) in a two-dimensional representation, while in Figure 3.8 the corrected  $p_t$  spectra are plotted for the six rapidity ranges together with the statistical (black) and systematic uncertainties (orange), which were determined as described in Section 3.1.3. Larger systematic uncertainties can be observed in the rapidity intervals farer away from mid-rapidity, which is due to the decrease of statistics and therefore leads to instability of the mass fits. However, these  $K_S^0$   $p_t$ - $y$  spectra from p+p reactions can be used for the validation of theoretical model calculations, which will be shown in Section 3.5.

### 3.2.2 Rapidity Density Distribution

Based on the  $p_t$ - $y$  spectra introduced above, rapidity density ( $dN/dy$ ) distributions can be explored. In this context, negative rapidity values are called target rapidities, while positive values are named beam rapidities, with respect to the center-of-mass system. These terms indicate the possibility to study regions, which are preferred for particle emission, since target rapidities correspond to backward emission and beam rapidities to forward emission. In the studied p+p collisions a symmetrical distribution with regard to the mid-rapidity ( $y_{cm} = 0$ ) is expected, which is related to the symmetric initial reaction system. Accordingly, a shifted spectrum will be observed in asymmetric colliding systems as for example in p+Nb reactions. Here, mainly secondary scattering processes on the nuclear target are responsible for this effect leading to a shift towards backward rapidities.

However, one possibility to extract the  $dN/dy$  spectra without having a  $4\pi$ -detector acceptance is to use the corrected  $p_t$ - $y$  distributions. As these spectra can only reflect the yield inside the acceptance, a method to extrapolate the yield to unmeasured kinematic regions had to be conceived. The unmeasured  $p_t$  region is dependent on the selected rapidity bin as shown in Figure 3.8. One can see that low transverse momenta are fully covered, while at higher  $p_t$  regions the acceptance breaks down. Therefore, a fit with a Boltzmann function (Eq. 3.5) was applied to the spectra fitting the tail of the available  $p_t$  distribution, to estimate the yield in the unmeasured momentum region by integrating over this range. Although the  $K_S^0$  momentum spectrum in p+p collisions is not expected a priori to follow Boltzmann behavior, it fits rather nicely to the  $p_t$  spectra as demonstrated in Figure 3.9, visible as gray curves. The total counts measured in a certain rapidity range was then calculated as the sum of all measured  $p_t$  points and the integral at high  $p_t$  extrapolated by the Boltzmann fit.

$$f(p_t) = A \cdot p_t \cdot \sqrt{p_t^2 + m_0^2} \cdot e^{-\frac{\sqrt{p_t^2 + m_0^2}}{T_B}} \quad (3.5)$$

with

$A$  : amplitude

$p_t$  : transverse momentum

$m_0$  : rest mass

$T_B$  : inverse slope parameter

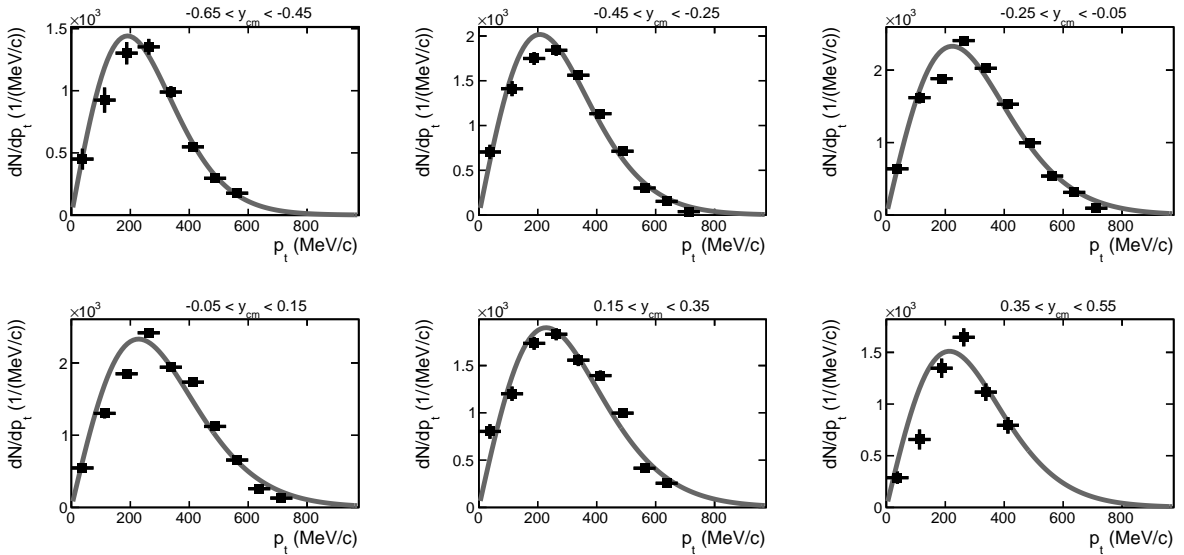


**Figure 3.9:** Acceptance and efficiency corrected transverse momentum  $p_t$  distributions of  $K_S^0$ 's in six center-of-mass rapidity bins and fitted by a Boltzmann function (Eq. 3.5) in gray.

The resulting acceptance and efficiency corrected rapidity density spectrum is depicted in Figure 3.10 panel (a). Again, the orange bars indicate the systematic uncertainties, which

were estimated with help of the minimal and maximal systematic uncertainties in the  $p_t$  distributions (Fig. 3.8). The  $dN/dy$  measurements are distributed symmetric with respect to the mid-rapidity, which is expected as mentioned above. Thus, one can exclude severe errors in the analysis procedure. Moreover, it was possible to extract the total yield and therefore the total production cross section of neutral kaons from this rapidity density distribution. To extrapolate to the unmeasured rapidity regions, a Gaussian function was fitted to the spectrum, which is illustrated as a black curve in the same plot. After normalizing the Gaussian integral absolutely to the elastic scattering cross section as explained in Section 2.3.3, the total  $K^0$  production cross section in p+p reactions was determined to be  $113.5 \pm 2.7(stat)_{-10.2}^{+16.6}(sys) \pm 7.95(sys_{norm}) \mu b$  at 3.5 GeV kinetic beam energy. Here, the branching of  $K^0$  into either  $K_S^0$  or  $K_L^0$  with a probability of 50% each was taken into account. The systematic uncertainties of the total cross section were estimated by the integrals of Gaussian fits to the maximal and minimal systematic uncertainties in the rapidity density distribution.

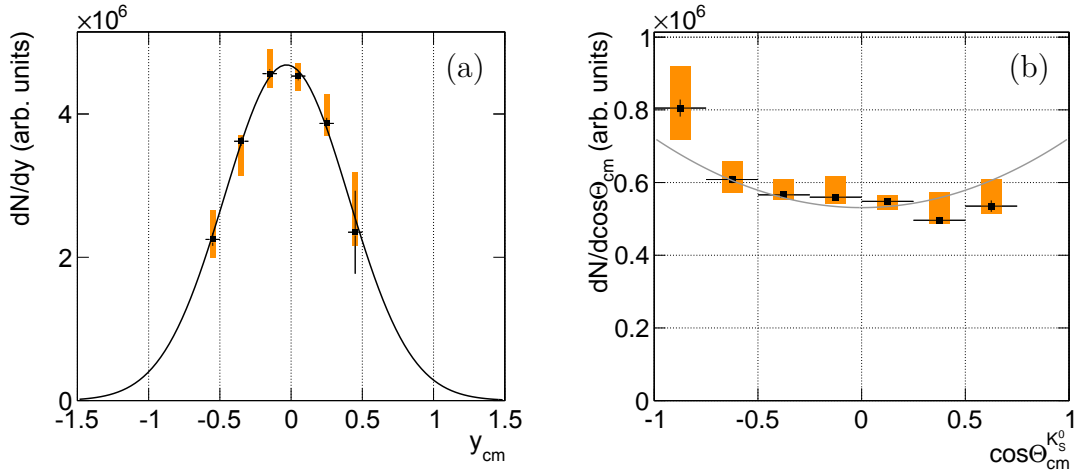


**Figure 3.10:** Panel (a):  $K_S^0$  rapidity density distribution extracted from the  $p_t$ - $y_{cm}$  spectra in Figure 3.9. The black curve corresponds to a Gaussian fit for the determination of the total  $K^0$  production cross section. Panel (b): Angular distribution  $\cos\Theta_{cm}$  of  $K_S^0$ 's fitted with a Legendre polynomial function (Eq. 3.6) in gray. Both spectra are corrected for acceptance and efficiency. The black lines along  $y$  indicate statistical uncertainties and the orange bars illustrate the systematic ones.

### 3.2.3 Angular Distributions

Another representation for the  $K_S^0$  production kinematics is the angular distribution  $\cos\Theta_{cm}$  in the center-of-mass reference frame, which emphasizes similar information like the rapidity density distribution. The range of the cosine ranging from  $-1$  to  $1$  corresponds to the polar angles from  $0^\circ$  to  $180^\circ$  and thus stands for the emission region, backward or forward, of the studied particle. In line with the rapidity density spectrum a symmetric distribution is expected with respect to  $\cos\Theta_{cm} = 0$  for symmetric colliding systems. But in addition,

$\cos\Theta_{cm}$  plots contain direct information on the iso- or anisotropy of the particle production, which strength can be quantified by fitting the distribution with a Legendre polynomial function (Eq. 3.6):

$$F(\cos\Theta_{cm}) = A_0 + A_1\cos\Theta_{cm} + A_2\frac{1}{2}(3\cos^2\Theta_{cm} - 1), \quad (3.6)$$

where  $A_0$  compensates for an offset coming from the statistics of a data sample or in the case of absolute normalized data depends on the production cross section. The coefficient  $A_1$  introduces a linear term for asymmetric distributions. Since the studied p+p collision system is symmetric, particle emission is also expected to be symmetric in the pp-center-of-mass reference frame. Hence, this term could be neglected. The last noted coefficient  $A_2$  describes the strength of a potential anisotropy in the production. If it is normalized to  $A_0$ , a direct comparison between different measurements can be drawn. From the general form of the Legendre polynomial function actually infinite number of terms can occur. However, the inclusion of further terms in the analysis had no influence and thus these correction terms could be omitted.

In Figure 3.10 panel (b) the corrected angular distribution of the  $K_S^0$  is plotted in black together with statistical (black lines) and systematic uncertainties (orange bars) and fitted with a Legendre polynomial function (gray curve). The data clearly favors a backward-forward anisotropy, which is confirmed by the fit. The out-coming coefficients are listed in Table 3.3. The ratio  $A_2/A_0$  was found to be  $0.214 \pm 0.017$  in the  $p_{cm}$  range 0 – 800 MeV/c, which can be interpreted as a slight anisotropy comparable to the measured  $K^0$  angular distribution by the COSY-TOF Collaboration with  $A_2/A_0 = 0.330 \pm 0.120$  at  $p_{beam} = 3059$  MeV/c for the reaction  $p+p \rightarrow \Sigma^+ + p + K^0$  [AB<sup>+</sup>12]. As will be shown later from the exclusive measurement of  $K_S^0$  channels (Chapter 4), this angular anisotropy seen here is a mixture of strong directional production of the resonant reactions  $p+p \rightarrow \Lambda + \Delta^{++} + K^0$  and  $p+p \rightarrow \Sigma(1385)^+ + p + K^0$  with isotropic four- or even five-body reactions.

**Table 3.3:** Coefficients of the Legendre polynomial functions fitted to  $K_S^0$  angular distributions depending on the studied center-of-mass momentum range. Quoted are also the normalized second coefficients  $A_2/A_0$  for the comparison to other measurements.

$p_{cm}$ [MeV/c]	$A_0$ [ $10^3$ ]	$A_2$ [ $10^3$ ]	$A_2/A_0$
0 – 800	$594.8 \pm 3.7$	$127.5 \pm 9.8$	$0.214 \pm 0.017$
0 – 160	$43.3 \pm 1.4$	$9.6 \pm 3.8$	$0.223 \pm 0.089$
160 – 320	$193.3 \pm 2.2$	$30.6 \pm 6.0$	$0.158 \pm 0.031$
320 – 480	$220.0 \pm 1.9$	$25.9 \pm 5.2$	$0.118 \pm 0.024$
480 – 640	$108.6 \pm 1.2$	$27.9 \pm 3.2$	$0.257 \pm 0.030$
640 – 800	$26.0 \pm 0.7$	$15.0 \pm 1.8$	$0.578 \pm 0.070$

However, a complete model independent correction can only be carried out in two-dimensional kinematics, which is why the  $K_S^0$  angular distribution was also studied as a function of the center-of-mass momentum  $p_{cm}$ . Depending on the phase space coverage

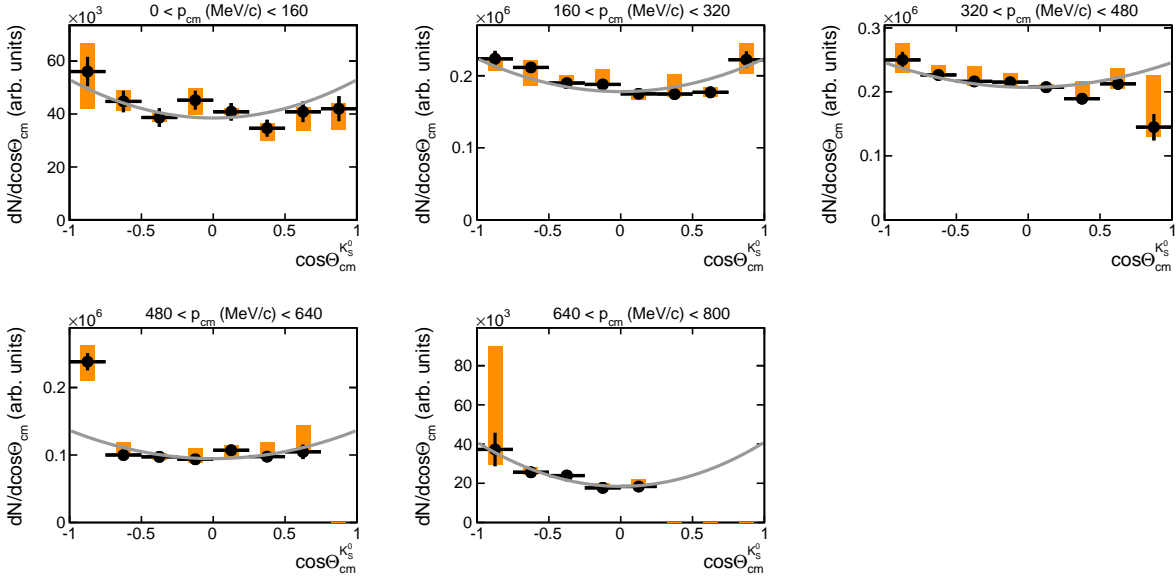


**Figure 3.11:** Acceptance and efficiency corrected angular distributions  $\cos\Theta_{cm}$  of  $K_S^0$ 's in five center-of-mass momentum bins fitted with Legendre polynomial functions (Eq. 3.6) in gray. The black lines in the y-direction indicate statistical uncertainties and the orange bars correspond to systematic ones.

of the data the ranges and binning were chosen as follows:  $p_{cm} = 0 - 800$  MeV/c with  $\Delta p_{cm} = 160$  MeV/c and  $\cos\Theta_{cm} = -1 - 1$  with  $\Delta\cos\Theta_{cm} = 0.25$ . The corresponding distributions are illustrated in Figure 3.11 and were fitted with the Legendre polynomial function (Eq. 3.6) to see how the strength of the anisotropy develops. Table 3.3 contains the results of the fits. The normalized  $A_2$  coefficients prove what is already visible by eye, namely that the anisotropy is present in all momentum bins. Moreover, derived from the numbers an increasing angular dependence was observed to lower and higher momenta with the minimum in the intermediate momentum range, where  $p_{cm} = 320 - 480$  MeV/c.

### 3.3 Self-Consistency Checks

In Section 3.2.2 it has been already mentioned that severe mistakes in the analysis especially in the correction procedure can be excluded, since a rather symmetric rapidity density distribution with respect to the NN mid-rapidity was obtained. However, a more precise method to validate the analysis are self-consistency checks. For such checks two different models are used, to prove also the model independence of the acceptance and efficiency correction, which is explained in Section 3.1.2. One can then either correct the fully analyzed model I with the correction matrix determined with model II and check, if the corrected model I is equal to its input, or one can directly compare the correction matrices obtained from both models. The conclusions, that can be drawn from the results in both cases, are equivalent and therefore only one of them was carried out, namely the latter one.

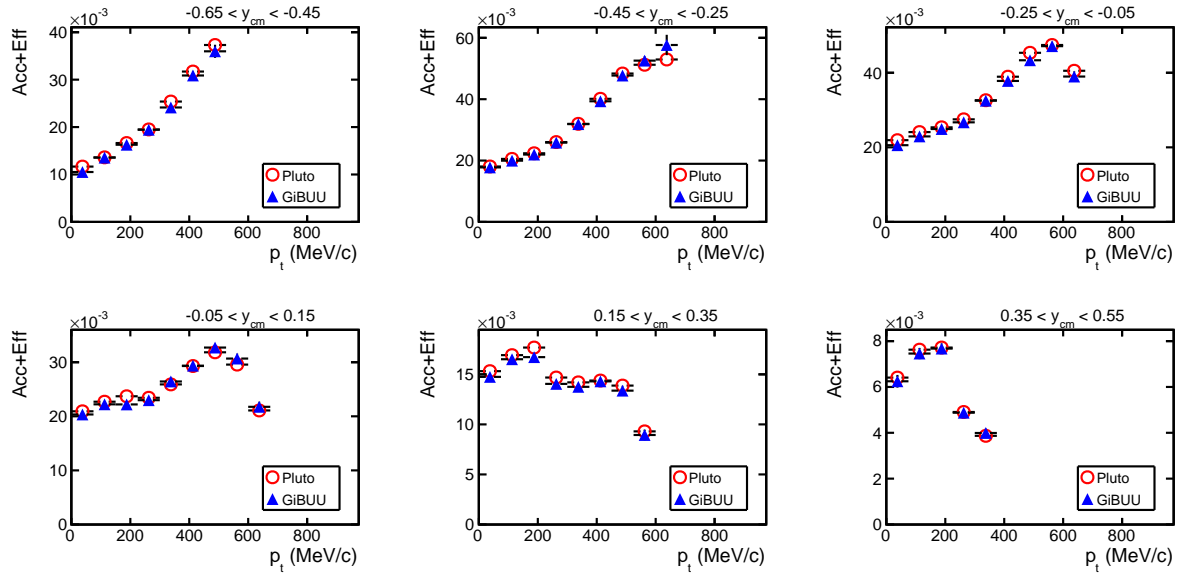


**Figure 3.12:** Comparison of the  $K_S^0$  acceptance and efficiency correction matrices in the  $p_t$ - $y_{cm}$  frame. The red open circles depict the correction obtained with the Pluto/Monte Carlo cocktail of 13  $K_S^0$  channels and the blue triangles correspond to GiBUU simulations [B<sup>+</sup>12].

For this purpose the Pluto simulation composed by the 13  $K^0$  production channels was used on the one hand, since this is the model employed for the corrections of the experimental data, and on the other hand the resonance based GiBUU model [B<sup>+</sup>12]. Both models have quite different kinematical distributions as can be seen in the Figures 3.14 and 3.22 showing their  $p_t$ - $y_{cm}$  spectra and therefore are suited for a self-consistency check. They were both processed through a full scale analysis using Geant3, to simulate the detector acceptance, the same tracking algorithm as for the experiment and also the same analysis steps. These filtered simulations were then divided by the corresponding input spectra to obtain the acceptance and efficiency correction matrices. A double differential presentation of the correction matrices was chosen, to allow for a model independent correction. Ultimately, the comparison of both models was plotted in terms of  $p_t$ - $y_{cm}$  and can be seen in Figure 3.12. The same ranges and binning were applied as noted in Section 3.2.1 for the experimental distributions. An extremely good agreement of both models is observed over the whole kinematical range confirming that the correction procedure, which is performed with help of the Pluto cocktail, can be employed on the experimental data without any bias. Furthermore, this comparison confirms the assumption that the correction done in two kinematical independent variables is model independent. That means also that the model used for the correction does not have to reproduce the reality perfectly and thus it does not matter, if the Pluto cocktail is not complete in the sense of  $K_S^0$  reactions, their cross sections and their potential angular anisotropies. Finally, one can conclude that the extracted spectra in this inclusive analysis can indeed be used to carry out comparisons to various theoretical models as will be shown in Section 3.5.

### 3.4 Comparison to the Pluto Cocktail

In this section, the double differential kinematical distributions, which have been discussed above, are compared with the Pluto cocktail. This cocktail consists of the 13 simulated  $K^0$  production channels, that have been introduced in Section 2.4.2 for the acceptance and efficiency corrections and includes also for one channel, namely the reaction  $p + p \rightarrow \Sigma^+ + p + K^0$ , an angular anisotropy for the  $K^0$  production modeled on the findings of the COSY-TOF Collaboration in [AB<sup>+</sup>12]. Furthermore, the individual cross sections were used according to Table 2.2.

The comparison of the  $p_t$ - $y_{cm}$  spectra are plotted in Figure 3.13 on an absolute scale meaning that both the experimental and the simulated spectra are absolutely normalized and can be presented in terms of cross sections (Sec. 2.3.3). One can see that the data (black squares) are rather well reproduced by these plain Monte Carlo simulations (red open circles) especially in the region around mid-rapidity. However, some discrepancies are observed. The position of the maxima are located 50-100 MeV/c lower than in the experiment in all rapidity ranges. Furthermore, disagreements are visible in the first and the last rapidity bins ( $-0.65 < y_{cm} < -0.45$  and  $0.35 < y_{cm} < 0.55$ ) hinting at a stronger anisotropy in the  $K_S^0$  production than included in the simulation. This suggestion has already been mentioned and will be brought up in more detail when discussing the exclusive  $K_S^0$  production in the next chapter. Nevertheless, by looking at Figure 3.14, in which the angular distributions are compared, this statement appears to be confirmed even if just slightly more anisotropy seems to be needed. This is also seen, when looking at the  $A_2/A_0$  ratios (Table 3.4) obtained by Legendre polynomial fits. Although the simulation tends to underestimate the data in both figures, which comes from the fact that the absolute cross section of the simulation is only  $\approx 94.74 \mu b$  while the extracted experimental cross section is  $\approx 113.5 \pm 2.7(stat)_{-10.2}^{+16.6}(sys) \mu b$ , it is worth mentioning that the simulation catches the data rather well in all  $p_{cm}$  ranges in terms of yield. This will not always be the case for transport models as will be shown in the following.

**Table 3.4:** Normalized second coefficients  $A_2/A_0$  of the Legendre polynomial functions fitted to  $K_S^0$  angular distributions depending on the studied center-of-mass momentum range for the Pluto, HSD, UrQMD, GiBUU-PYTHIA and GiBUU-resonance model.

$p_{cm}$ [MeV/c]	Pluto	HSD	UrQMD	GiBUU-P	GiBUU-R
0 – 160	$0.017 \pm 0.008$	$0.145 \pm 0.009$	$0.006 \pm 0.022$	$0.137 \pm 0.018$	$0.069 \pm 0.013$
160 – 320	$0.027 \pm 0.004$	$0.434 \pm 0.005$	$0.130 \pm 0.011$	$0.376 \pm 0.010$	$0.093 \pm 0.005$
320 – 480	$0.057 \pm 0.004$	$0.553 \pm 0.005$	$0.711 \pm 0.010$	$0.618 \pm 0.009$	$0.114 \pm 0.004$
480 – 640	$0.153 \pm 0.006$	$1.111 \pm 0.008$	$0.726 \pm 0.013$	$1.069 \pm 0.013$	$0.217 \pm 0.006$
640 – 800	$0.315 \pm 0.011$	$1.595 \pm 0.013$	$0.919 \pm 0.019$	$1.727 \pm 0.021$	$0.537 \pm 0.023$

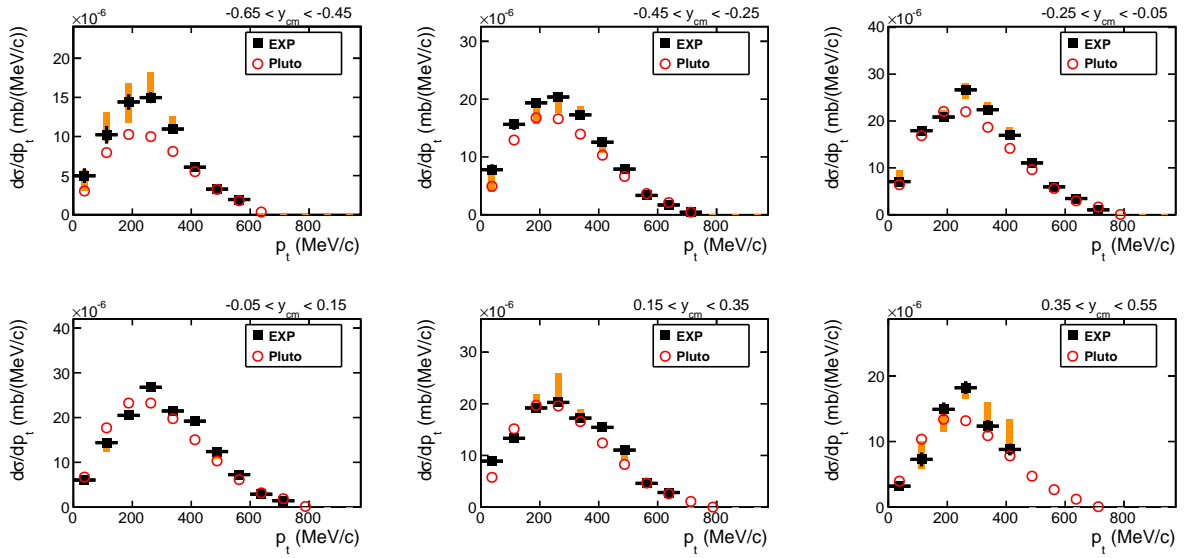


**Figure 3.13:** Comparison of the experimental  $K_S^0$   $p_t$ - $y_{cm}$  distributions (black squares) to a Pluto/Monte Carlo cocktail of 13  $K_S^0$  channels (red open circles) on an absolute scale. The experimental data include statistical (black lines) and systematic uncertainties (orange bars).

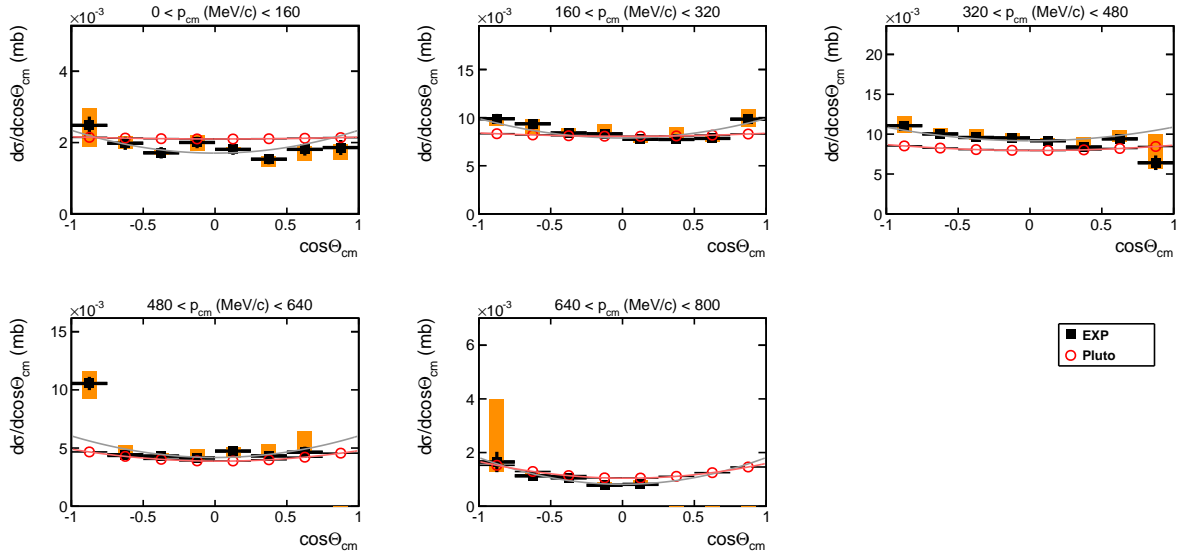


**Figure 3.14:** Comparison of the experimental  $K_S^0$  angular distributions (black squares) to a Pluto/Monte Carlo cocktail of 13  $K_S^0$  channels (red open circles) as a function of five center-of-mass momentum bins. Both data sets are absolute normalized and fitted with a Legendre polynomial function (Eq. 3.6). The experimental data include statistical (black lines) and systematic uncertainties (orange bars).

## 3.5 Comparison to Transport Calculations

Since the production of the  $K_S^0$  meson could be analyzed in almost full possible phase space and were corrected for acceptance and efficiency effects, the data are perfectly suited to validate transport models. For this purpose the very little statistical and moderate systematic uncertainties are also beneficial. Especially the studied kinetic beam energy of 3.5 GeV is of great interest, as this intermediate energy regime is located within a so called transition region, in which resonance models might be slowly replaced by string fragmentation models with increasing collision energy. Therefore, transport calculations from both types were selected for comparison. The comparison to the string fragmentation model of HSD [CB99] can be found in the next Section 3.5.1, to the resonance model of UrQMD [B<sup>+</sup>98] in Section 3.5.2 and to the GiBUU [B<sup>+</sup>12] model, which allows to study both types, in Section 3.5.3. More details about the transport models can be found in the introduction (Sec. 1.6).

### 3.5.1 Comparison to HSD

The choice to compare the presented data to the transport model HSD [CB99] is motivated by the publication of the FOPI Collaboration [B<sup>+</sup>09], in which the  $KN$  potential of  $K_S^0$  have been obtained in  $\pi^- + A$  collisions at  $p_{beam} = 1.15$  GeV/c with the help of this calculation (Fig. 1.8). This model uses a string fragmentation model named FRITIOF [AGP93], which is the former PYTHIA [SMS06], to describe the particle production at the studied energy of 3.5 GeV.

Similar as in Section 3.4 the model was compared in the  $p_t$ - $y_{cm}$  and in the  $\cos\Theta_{cm}$ - $p_{cm}$  frames (Figs. 3.15 and 3.16). Here, the model calculation is plotted as green open crosses and was absolutely normalized like the experimental data (black squares). The comparison reveals that the HSD model in general overshoots the experimental yield at low transverse momenta ( $p_t \lesssim 300$  MeV/c), while the larger transverse momenta are in good agreement. As a result the peak positions of the momentum spectra are all shifted to lower values with respect to the experimental distributions. This behavior is reflected in the angular distributions in that way that a clear excess is observed in the two bins, where  $p_{cm} < 320$  MeV/c, but at larger momenta a better agreement is achieved concerning the  $K_S^0$  production yield. Furthermore, the angular anisotropy is not only too strong in all  $p_{cm}$  bins, which can be retrieved from the  $A_2/A_0$  ratios in Table 3.4, but also features different characteristics compared to the experimental data (Table 3.3). As has been pointed out in Section 3.2.3 the data show an increasing strength of the anisotropy moving to lower and higher momenta with the minimum anisotropy at  $p_{cm} = 320 - 480$  MeV/c. In contrast, the HSD model shows a steep increase of the anisotropy with growing momenta. These findings do not automatically lead to the claim that the model does not work in general, for example for  $\pi^- + A$  reactions at low energies, but strongly suggest to investigate the reasons for the discrepancies in low energy p+p collisions, which would strengthen the reliability for more complex systems also at higher energies.

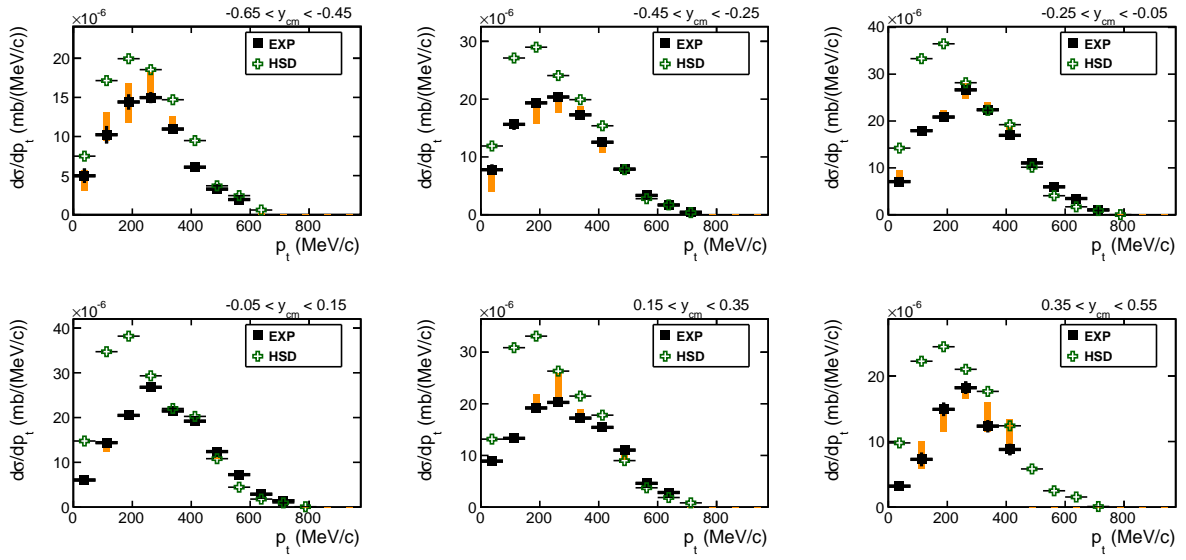


**Figure 3.15:** Comparison of the experimental  $K_S^0$   $p_t$ - $y_{cm}$  distributions (black squares) to the HSD transport model [CB99] (green open crosses) on an absolute scale. The experimental data include statistical (black lines) and systematic uncertainties (orange bars).

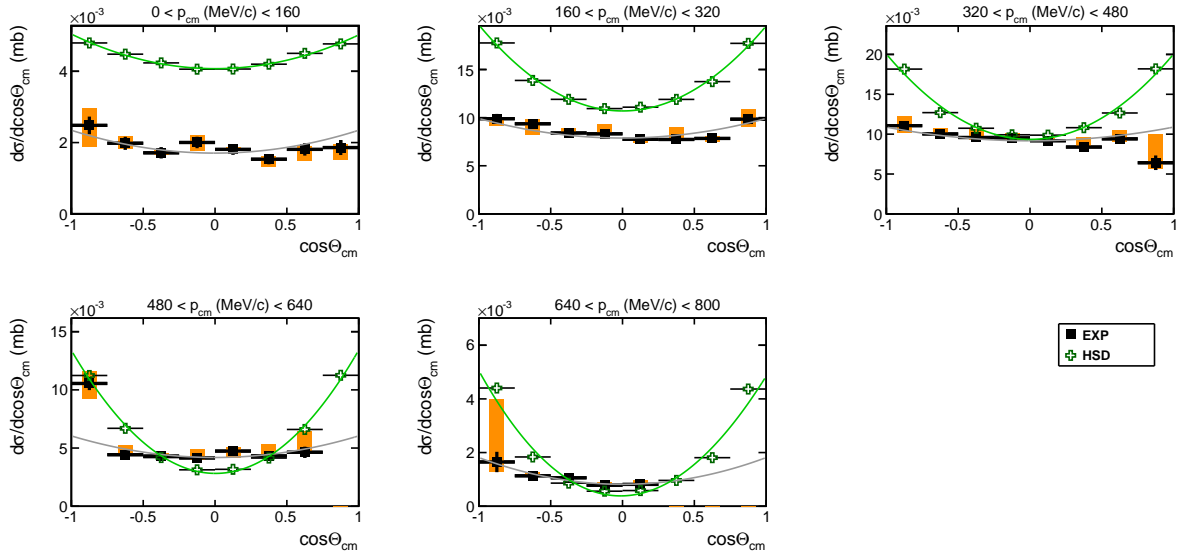


**Figure 3.16:** Comparison of the experimental  $K_S^0$  angular distributions (black squares) to the HSD transport model [CB99] (green open crosses) as a function of five center-of-mass momentum bins. Both data sets are absolute normalized and fitted with a Legendre polynomial function (Eq. 3.6). The experimental data include statistical (black lines) and systematic uncertainties (orange bars).

### 3.5.2 Comparison to UrQMD

A further commonly used transport model is the so called UrQMD model [B<sup>+</sup>98]. In contrast to the above discussed calculation, here, particle productions are always realized through two-body decays of intermediate resonances. Therefore, one can speak of a pure resonance model, at least in the low energy regime. Since the energy of this measurement is considered by theoreticians to lie in a transition region, in which it is not clear whether resonance models are still applicable or already string fragmentation models like HSD have to be employed, it is worth to perform a comparison of the data with the UrQMD model.

The same observables were consulted for this comparison as for the HSD calculation and again model and data are absolutely normalized. In Figure 3.17, in which the  $p_t$ - $y_{cm}$  spectra are plotted, it is clearly visible that the model (magenta open squares) underestimates the experimental yield in all rapidity bins. However, the shape of the transverse momentum spectra and so also the peak positions are rather well reproduced. Furthermore, one can see that the gap between model and data increases towards mid-rapidity indicating that the angular dependence of the production is not described correctly. This assumption is confirmed, when looking at Figure 3.18, which shows the angular distributions as a function of  $p_{cm}$ . While at low momenta the model seems to underestimate the strength of the angular anisotropy, too much anisotropy is observed with  $p_{cm} > 160$  MeV/c. From a Legendre polynomial fit of the angular distributions (magenta line) the normalized  $A_2$  coefficient was extracted and is listed in Table 3.4. The quoted numbers, which again scale with increasing momenta as seen from the HSD model, reflect what has been claimed before. However, a known issue in the UrQMD calculation is that direct three-body reactions or even more than three-body reactions are completely missing in the model, which very likely play a role in the studied energy regime. Hence, a three-body or more than three-body final state can only be produced by generating intermediate resonances, which decay in a second step (e.g.  $p + p \rightarrow N + R \rightarrow N + K + Y$ ). Therefore, the disagreement between model and experimental data is expected in a certain way.

### 3.5.3 Comparison to GiBUU

A third transport model was consulted for comparison, namely the GiBUU model [B<sup>+</sup>12]. As described in the introduction (Sec. 1.6) this model provides a switch to set the transition region from resonance model to the PYTHIA string fragmentation model at a given energy. In the default GiBUU code the transition energy for baryon-baryon collisions is set to  $\sqrt{s} = 2.6$  GeV with a transition region of  $\pm 0.2$  GeV. However, already for the study of dileptons the GiBUU model has been improved [WvHM12] to describe the data in the HADES energy regime ( $\sqrt{s} < 3.18$  GeV) within a single model. Among other improvements, the transition region has been pushed to  $\sqrt{s} = 3.4 \pm 0.1$  GeV and so all HADES data is compared with pure resonance model in that attempt. In the present study dealing with strangeness both approaches were compared to the  $K_S^0$  spectra by moving the switch for the transition region accordingly. One has to mention here that in contrast to the dilepton studies a different resonance model is implemented in the GiBUU model. When studying

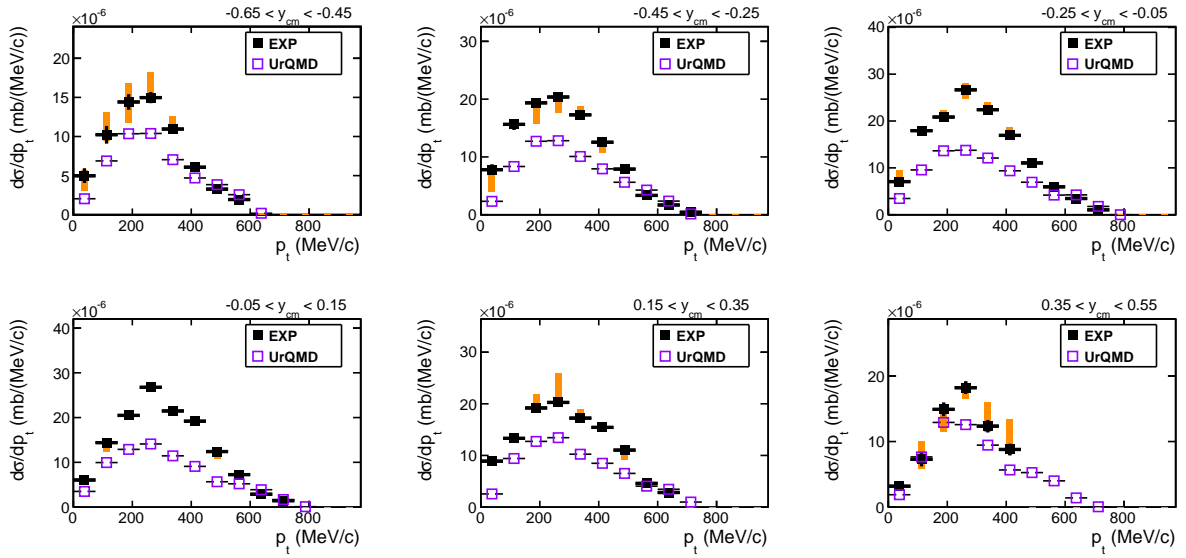


**Figure 3.17:** Comparison of the experimental  $K_S^0$   $p_t$ - $y_{cm}$  distributions (black squares) to the UrQMD transport model [B<sup>+</sup>98] (magenta open squares) on an absolute scale. The experimental data include statistical (black lines) and systematic uncertainties (orange bars).

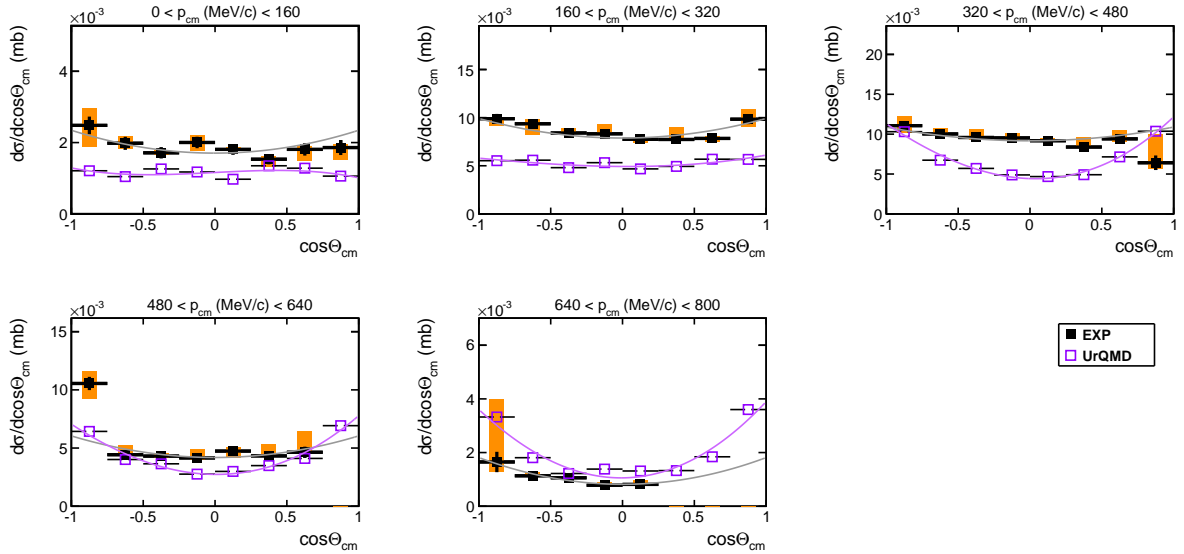


**Figure 3.18:** Comparison of the experimental  $K_S^0$  angular distributions (black squares) to the UrQMD transport model [B<sup>+</sup>98] (magenta open squares) as a function of five center-of-mass momentum bins. Both data sets are absolute normalized and fitted with a Legendre polynomial function (Eq. 3.6). The experimental data include statistical (black lines) and systematic uncertainties (orange bars).

non-strange reactions the GiBUU model uses resonance parameterizations from Manley and Saleski [MS92], but since this calculation does not cover strangeness, the resonance calculation from Tsushima [TST99] is employed in this case.

Again the comparison of the experimental data to the GiBUU model was carried out in the  $p_t$ - $y_{cm}$  and in the  $\cos\Theta_{cm}$ - $p_{cm}$  representations. The Figures 3.19 and 3.20 show the corresponding spectra with the PYTHIA based model (open blue triangles). Consistently to the HSD calculation, which also exploits the string fragmentation model, an overshoot of the model is observed at low transverse momenta ( $p_t \lesssim 400$  MeV/c) in all rapidity ranges on an absolute scale, whereas the high momentum tails are rather well reproduced leading to a shift of the maximum momenta to lower regions as compared to the experimental spectra. This excess is also visible in the angular distributions, while again too strong angular anisotropies in the  $K_S^0$  production were assumed by the PYTHIA model. However, the  $A_2/A_0$  coefficients extracted from Legendre polynomial fits (Table 3.4) show an even more rapidly growing anisotropy as a function of the center-of-mass momentum as in the case of HSD. This development of the angular distributions is not observed in the experimental data, as has been pointed out in Section 3.2.3.

Moreover, if the pure resonance model based GiBUU calculation is adapted, the comparison to the experimental spectra (Figs. 3.21 and 3.22) still exhibits an overshoot of the absolute yield. However, the overshoot is found at intermediate momenta ( $p_t \approx 150 - 525$  MeV/c). Since the maxima of the transverse momentum distributions are shifted to higher momenta compared to the experimental spectra, it can be claimed that not even the shape is reproduced by the model as it was the case for the UrQMD calculation. From the angular distributions plotted for several center-of-mass momentum bins, a similar observation was found. Although the experimental yields are relatively well described at low and high momenta, a large deviation is found at intermediate momenta, where  $p_{cm} = 320 - 480$  MeV/c. The strength of the angular anisotropy in the model, which only includes the anisotropies of three-body reactions  $p + p \rightarrow Y + B + K$ , catches the experimental data in a satisfactory way. Nevertheless, also here the anisotropy increases with growing momentum (see Table 3.4), which is not the case in the measurement (Table 3.3).

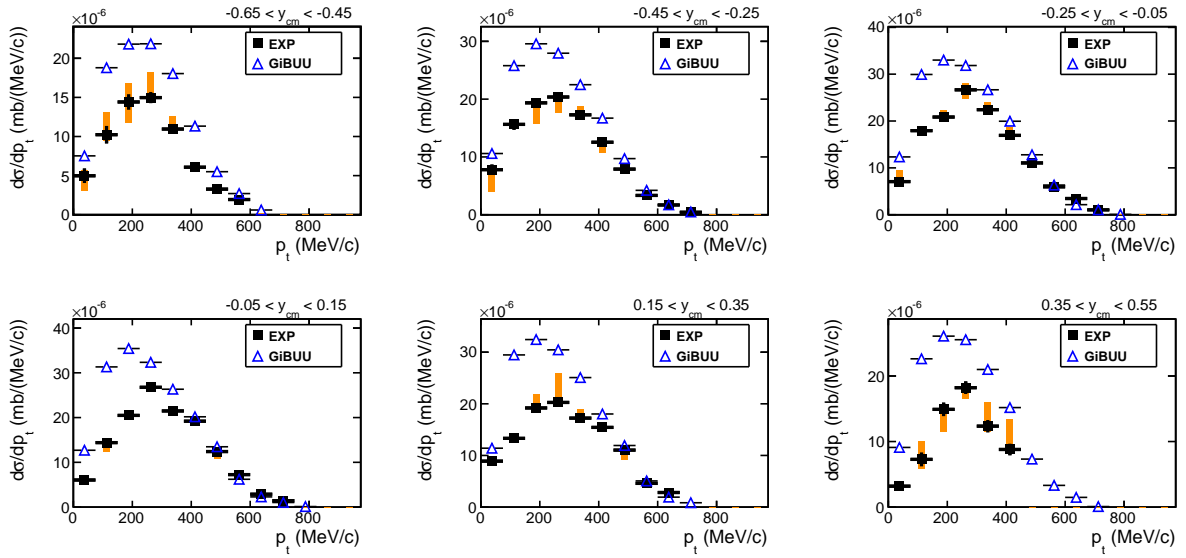


**Figure 3.19:** Comparison of the experimental  $K_S^0$   $p_t$ - $y_{cm}$  distributions (black squares) to the GiBUU transport model [B<sup>+</sup>12] based on PYTHIA (blue open triangles) on an absolute scale. The experimental data include statistical (black lines) and systematic uncertainties (orange bars).

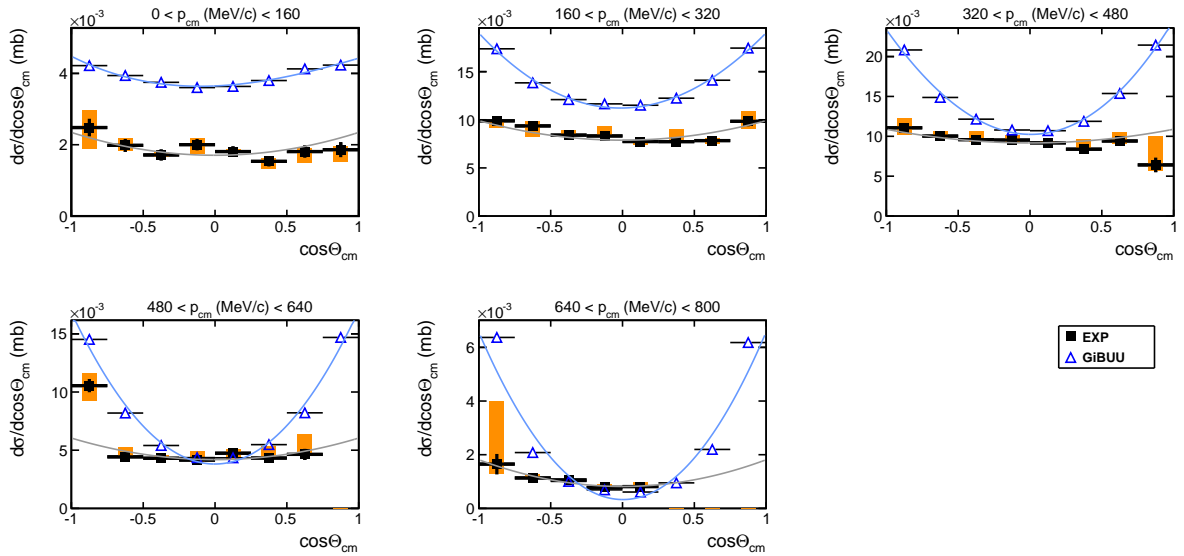


**Figure 3.20:** Comparison of the experimental  $K_S^0$  angular distributions (black squares) to the GiBUU transport model [B<sup>+</sup>12] based on PYTHIA (blue open triangles) as a function of five center-of-mass momentum bins. Both data sets are absolute normalized and fitted with a Legendre polynomial function (Eq. 3.6). The experimental data include statistical (black lines) and systematic uncertainties (orange bars).

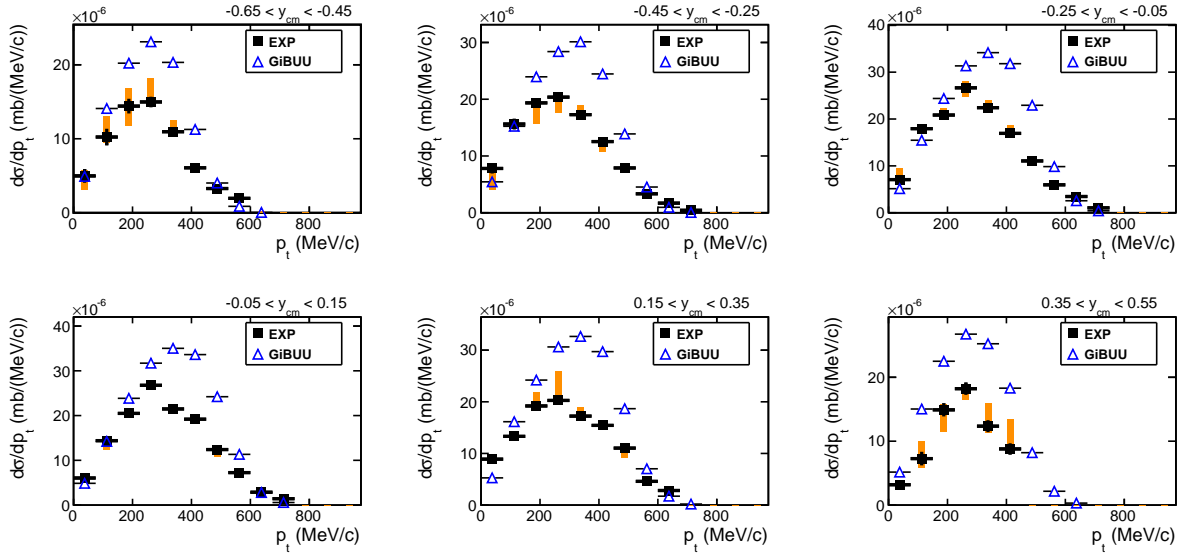


**Figure 3.21:** Comparison of the experimental  $K_S^0$   $p_t$ - $y_{cm}$  distributions (black squares) to the GiBUU transport model [B<sup>+</sup>12] based on the Tsushima resonance model [TST99] (blue open triangles) on an absolute scale. The experimental data include statistical (black lines) and systematic uncertainties (orange bars).

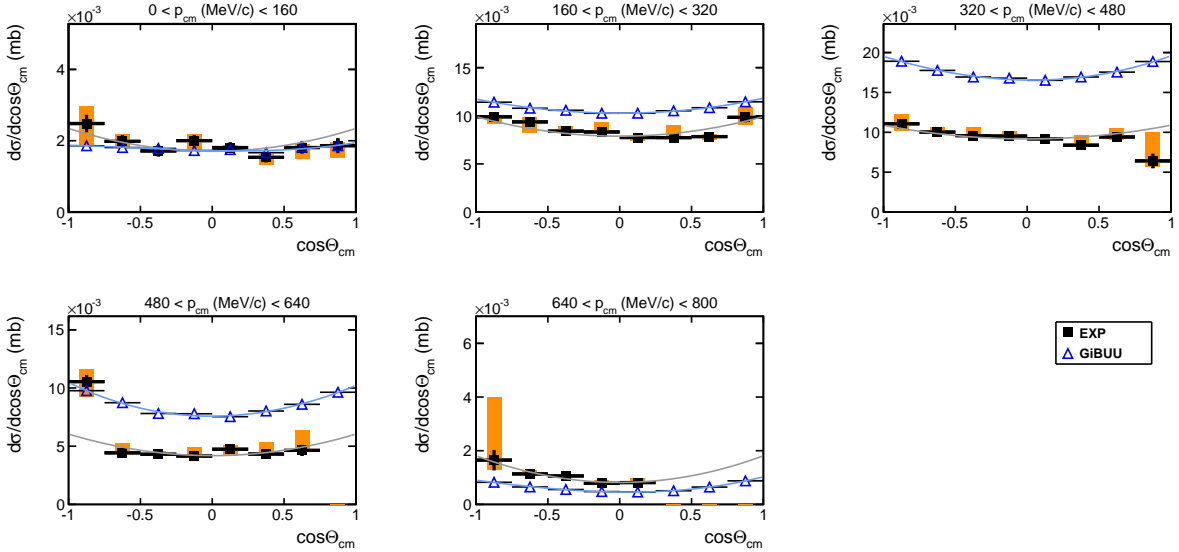


**Figure 3.22:** Comparison of the experimental  $K_S^0$  angular distributions (black squares) to the GiBUU transport model [B<sup>+</sup>12] based on the Tsushima resonance model [TST99] (blue open triangles) as a function of five center-of-mass momentum bins. Both data sets are absolute normalized and fitted with a Legendre polynomial function (Eq. 3.6). The experimental data include statistical (black lines) and systematic uncertainties (orange bars).

### 3.6 Summary of the Inclusive $K_S^0$ Analysis

The inclusive  $K_S^0$  analysis in p+p reactions at 3.5 GeV kinetic beam energy was performed with the aim to determine the production yield as a function of given kinematic variables. In particular, this measurement should serve as a reference for more complex p+A and heavy ion reactions for the study of kaon in-medium modifications such as the  $KN$  potential. Since the data of such complex systems are often interpreted with the help of transport models, the p+p data should also serve as a cross-check for these calculations. Therefore, the  $K_S^0$  was reconstructed in terms of  $p_t$ - $y_{cm}$  (Fig. 3.8),  $dN/dy_{cm}$  (Fig. 3.10, panel (a)),  $dN/d\cos\Theta_{cm}$  (Fig. 3.10, panel (b)) and  $p_{cm}$ - $\cos\Theta_{cm}$  (Fig. 3.11) and corrected with a Monte Carlo simulation of 13  $K^0$  channels for acceptance and efficiency. Not only expected symmetries of the rapidity density and angular distributions were found and therefore ensure the accuracy of the analysis, but also a successful self-consistency check put the analysis on solid ground and allowed the extraction of the total  $K^0$  production cross section of  $113.5 \pm 2.7(stat)_{-10.2}^{+16.6}(sys) \mu b$ . Furthermore, the angular distributions were fitted by means of a Legendre polynomial function (Eq. 3.6) to retrieve quantitative numbers, which can be compared to. Here, an increased anisotropy was observed for kaons, which were produced with either lower or higher momenta with the minimum anisotropy in the momentum range  $p_{cm} = 320 - 480$  MeV/c. The obtained coefficients of the fit are summarized in Table 3.3.

In Section 3.5 a comparison of the corrected spectra to three different transport models (HSD [CB99], UrQMD [B<sup>+</sup>98] and GiBUU [B<sup>+</sup>12]) is presented on an absolute scale, which either use string fragmentation models or resonance models for the transport calculation. However, none of the models showed satisfactory descriptions of the full experimental  $K_S^0$  production kinematics. For instance, the strength of the angular anisotropy develops differently than the experimental anisotropy. It rises for all transport calculations with increasing center-of-mass momentum and is with an exception on the resonance based GiBUU model too strong in all models. Also the production cross section could not be reproduced by any model. These discrepancies question the findings on the  $KN$  potential [B<sup>+</sup>09, B<sup>+</sup>04, A<sup>+</sup>10] and need further investigations from the theory side. From experimental side a more detailed analysis on the exclusive kaon production was carried out to deliver more reference points and probably also input for the transport calculations. This analysis will be shown in the next chapter.



## 4 The Exclusive $K_S^0$ production in p+p @ 3.5 GeV

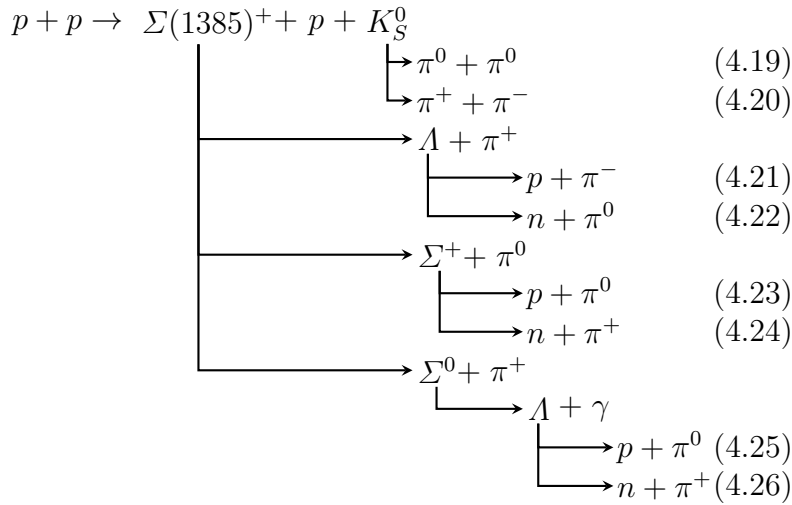
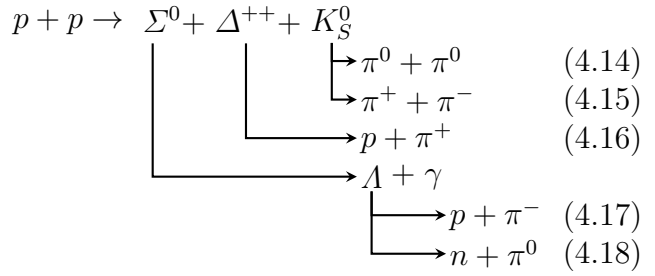
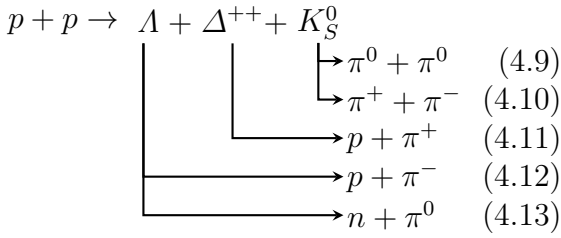
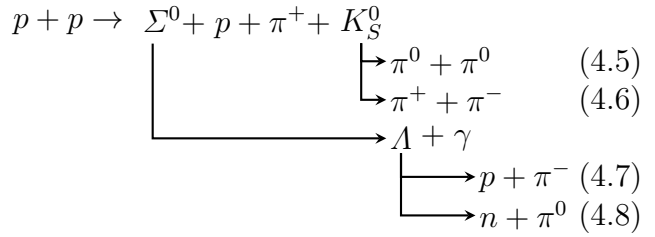
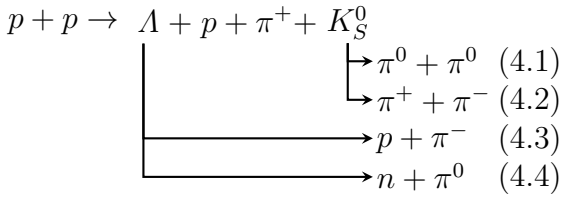
The study of the exclusive  $K_S^0$  production is not only interesting by itself, since the low energy region of the studied p+p measurement ( $\sqrt{s} = 3.18$  GeV) has only been investigated by few experiments, but is especially needed as an input and cross-check for theoretical calculations. In the last chapter it has been shown that none of the compared transport models (HSD [CB99], UrQMD [B<sup>+</sup>98] and GiBUU [B<sup>+</sup>12]) were able to describe the inclusive  $K_S^0$  spectra satisfactorily in terms of kinematics ( $p_t$ - $y_{cm}$  and  $p_{cm}$ - $\cos\Theta_{cm}$ ) and yield. In the case of the GiBUU model, when using the parametrization of the Tsushima resonance model, a clear indication for these discrepancies can be found in [TST99]. As mentioned before, this calculation overestimates most of the exclusive  $K^0$  production channels in the low energy region, where the models are only constrained by some measurements of the COSY-TOF and ANKE Collaboration [AB<sup>+</sup>12, N<sup>+</sup>07]. At higher energies one can find measurements from bubble chamber experiments, but with rather large uncertainties, which results are compiled in [MS88]. The experimental situation is depicted in Figure 2.11 for the most common reactions in the presented data sample. Especially for the four-body reactions a lack of measured cross sections is visible in the intermediate energy regime. A further question arises, if one recalls the transition energy for the application of resonance models and string fragmentation models, which is supposed to be located in the studied energy region. Namely, how large is the contribution of produced resonances and therefore, is the resonance model still applicable?

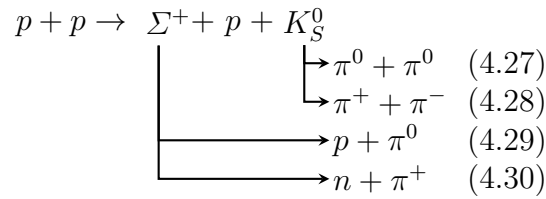
There are several possibilities for the formation of a kaon final state, in which resonances can play a role. For instance,  $\Sigma K$ -pairs can be generated through the decay of intermediate  $N^*$  or  $\Delta^*$  resonances and  $\Lambda K$ -pairs might be decay particles from  $N^*$ 's. A detailed investigation of such reactions has been performed for the three-body production channel  $p + p \rightarrow \Lambda + p + K^+$  in a separate analysis of the same data sample [Epp14, F<sup>+</sup>13, A<sup>+</sup>15], which shows that the main source for the  $K^+$  final state is not related to a direct production, but to the formation of  $N^*$  resonances. Furthermore, the study of the reaction  $p + p \rightarrow \Sigma(1385)^+ + n + K^+$  has shown that the production kinematics can be best modeled by assuming 33% of the resonant contribution  $p + p \rightarrow \Delta(2035)^{++} + n \rightarrow \Sigma(1385)^+ + n + K^+$  [A<sup>+</sup>12b]. The present study focuses on the production of a  $K_S^0$  accompanied by a resonance and ignoring how the kaon itself was created. By looking at the list of contributing  $K_S^0$  reactions (Table 2.2) it is noticeable that some of the reactions end up in the same final states, but differ in the resonance contribution. Therefore, one can speak of non-resonant and resonant reactions. One of these cases is for example the non-resonant reaction  $p + p \rightarrow \Lambda + p + \pi^+ + K^0$ , which final states can be also formed by the resonant reactions

$p + p \rightarrow \Lambda + \Delta^{++} + K^0$  and  $p + p \rightarrow \Sigma(1385)^+ + p + K^0$ . The same scenario occurs for the channel  $p + p \rightarrow \Sigma^0 + p + \pi^+ + K^0$  accordingly with exchanged hyperon content. Obviously, different production kinematics will be found for the different reactions. Therefore, it is crucial to have a precise knowledge of the cross sections and production kinematics of these reactions.

## 4.1 Analysis Procedure

In the upcoming sections a detailed description of the analysis procedure will be presented to study the following reactions taking into account part of the listed decay channels:





The main steps of the analysis start with a specific selection of interesting events from the full p+p data sample and continue with the reconstruction of the  $K_S^0$  (Sec. 4.1.1), the modeling of the background via a sideband technique (Sec. 4.1.3) and a simultaneous fit of simulated channels to a subset of missing and invariant mass spectra, in which the individual reactions are distinguishable (Secs. 4.1.2 and 4.1.4). Ultimately, the cross sections of the studied reactions were extracted and the angular distributions of the reactions  $p + p \rightarrow \Lambda/\Sigma^0 + \Delta^{++} + K^0$  were determined (Sec. 4.1.5).

### 4.1.1 Event and Track Selection

Since this analysis aims to study the contribution of the  $K^0$  reactions listed above, in particular  $p + p \rightarrow \Lambda/\Sigma^0 + \Delta^{++} + K^0$ , the event selection was chosen such to contain and measure as many final state particles as possible. However, one had to keep in mind that the detection of more than five particles ( $N_{particles} > 5$ ) in one event is very unlikely due to the limited HADES acceptance and reconstruction efficiency and would significantly reduce the available statistics. Therefore, a semi-exclusive selection was more reasonable and even allowed for the analysis of all the above mentioned reactions at once through some of their decay channels. Exactly four charged particles were required to be identified per event, which are a proton, a  $\pi^+$ , a  $\pi^-$  and another  $\pi^+$  assuming that the  $\pi^-$  and one of the  $\pi^+$  stem from the  $K_S^0$  decay (BR= 69.2%), whereas the proton and the other  $\pi^+$  are either produced directly (Ch. 4.2 or 4.6) or originate from the  $\Delta(1232)^{++}$  (Ch. 4.10+4.11 or 4.15+4.16). The reactions  $p + p \rightarrow \Sigma(1385)^+ + p + K^0$  and  $p + p \rightarrow \Sigma^+ + p + K^0$  are included in this event selection as well, if one assumes that the detected proton is a primary particle, whereas the second  $\pi^+$  is a daughter particle from the decay of the  $\Sigma(1385)^+$  or  $\Sigma^+$ . As for the inclusive analysis, the charged particles were identified via their specific energy loss in the MDCs (Sec. 2.2). Nevertheless, the question arises, why exactly four particles were asked for and not allowing more, since the relevant statistics reduces by  $\approx 40.9\%$  in comparison to a selection with  $N_{particles} \geq 4$  demanding at least the four mentioned particles. The reason for this decision is that due to the combinatorics it was possible to count an event multiple times even if the cuts on the target, on the  $K_S^0$  decay vertex and on the  $K_S^0$  mass were applied. Such double-counting can occur, if in the same event a particle type (e.g.  $\pi^+$ ) is present more than one time and hence several ways of combining these particles are possible. Therefore, one would end up with more than one combination of the same event. However, the probability for the double-counting of one event reduced from 23.3% to less than 0.3%, if events with more than four particles are rejected. That way, the simulation did not need to reproduce the probability of the multiple event counting and thus a complete and realistic p+p simulation was not required for the description of the data.

As already indicated, in the first attempt the  $K_S^0$  was reconstructed via its charged decay into two pions while applying several cuts on the selected data sample similarly as in the inclusive  $K_S^0$  analysis. To reduce off-target events a cut was applied on the reconstructed primary vertex distribution (Sec. 2.3.1), which was  $17 \times 17 \text{ mm}^2$  in the x-y-dimensions with respect to the corrected beam axis (see Section 2.3.2) and 60 mm in the direction of the beam. Furthermore, the same secondary vertex cuts were used as in the inclusive study, which are quoted in Table 3.1, although these cuts do not lead to the optimal  $S^2/B$  ratio in the exclusive analysis. This was actually needed here, because the analysis required a sufficient amount of background events to perform a sideband analysis. This procedure will be explained in Section 4.1.3. The resulting  $\pi^+\pi^-$ -invariant mass spectrum is illustrated in Figure 4.1 using the technique already explained in Section 3.1. The distribution was fitted with the sum of two Gaussians for the signal and the sum of a Landau and a third order polynomial function for the background description. From this fit a  $K_S^0$  signal of  $N_{K_S^0} = 6102$  was obtained inside the  $3\sigma$  region (dashed-dotted lines), which was calculated as the amplitude weighted average of the standard deviations of the two Gaussians. This  $3\sigma$  region was used later on as a cut to select  $K_S^0$  events. A rather large amount of background is left inside this region, that is reflected in the  $S/B$  ratio of 0.64. As mentioned before, this background is, however, helpful for the sideband analysis and therefore not a disadvantage.

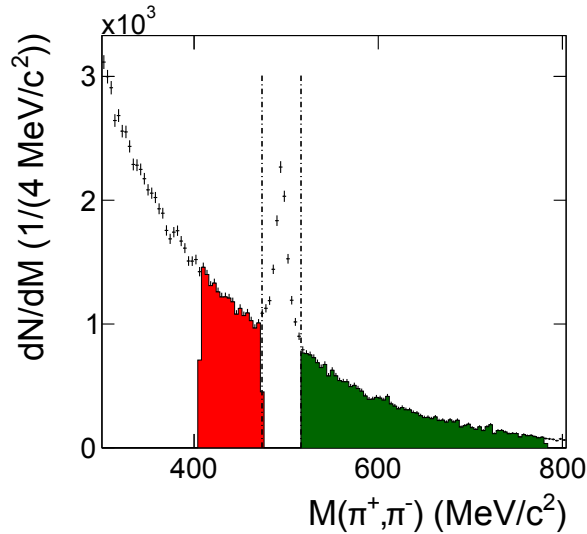


**Figure 4.1:**  $\pi^+\pi^-$ -invariant mass distribution after secondary vertex cuts for the selected event sample. The reconstructed values from a fit with the sum of two Gaussians, a polynomial and a Landau function are  $\langle m_{K_S^0} \rangle = 494.9 \text{ MeV}/c^2$ ,  $\langle \sigma_{K_S^0} \rangle = 7.1 \text{ MeV}/c^2$ ,  $N_{K_S^0} = 6102$  and  $S/B = 0.64$ . The dashed-dotted lines show the  $3\sigma$  region around the  $K_S^0$  signal. The red and green areas indicate the chosen low and high mass sideband sample, respectively.

In principle one could have tackled the resonant reactions  $p + p \rightarrow \Lambda/\Sigma^0 + \Delta^{++} + K^0$  by reconstructing the hyperon together with the decay products of the  $\Delta^{++}$ , for example by

selecting events with a proton, a  $\pi^+$ , another proton and a  $\pi^-$  (with  $\Lambda \rightarrow p + \pi^-$ ). However, this method has the disadvantage that the  $\Lambda$  channel cannot be distinguished from the  $\Sigma^0$  channel. This is only possible, if the  $K_S^0$  is reconstructed instead of the hyperon and then by building the missing mass of the four selected particles.

### 4.1.2 Missing Mass, Invariant Mass and Angular Distributions

Once the  $K_S^0$  has been reconstructed from the  $\pi^+\pi^-$ -invariant mass, a cut was defined to further enhance the purity of the event selection. Thereupon, a subset of kinematical observables had to be defined, which allow to distinguish the channels of interest listed in Section 4.1 from each other. For that, the invariant mass technique, which has been already explained in Section 3.1, and the missing mass technique were employed. The latter technique can only be employed, if one measures or knows all the participating particles in one reaction except the missing one (could be also more than one particle missing), as it is based on energy and momentum conservation. Therefore, this method is only applicable in elementary reactions, in which the 4-momentum of the beam ( $E_b, \vec{p}_b$ ) and target ( $E_t, \vec{p}_t$ ) are known. The 4-momentum of the missing particle can then be calculated from the measured particles ( $E_i, \vec{p}_i$ ):

$$m_{miss} = \frac{1}{c^2} \sqrt{E^2 - \vec{p}^2 c^2} = \frac{1}{c^2} \sqrt{\left(E_b + E_t - \sum_{i=1}^n E_i\right)^2 - \left(\vec{p}_b + \vec{p}_t - \sum_{i=1}^n \vec{p}_i\right)^2} c^2. \quad (4.31)$$

The advantage of this method is that also neutral particles can be identified, although none of the HADES detectors can measure them directly.

In this exclusive analysis this method was used to calculate the missing mass of the four selected particles  $MM(p, \pi^+, \pi^-, \pi^+)$  (Fig. 4.2, panel (a)), which was chosen to separate the reactions by their hyperon content. Indeed the resolution of the HADES setup is good enough to do so, since clear peaks corresponding to the missing  $\Lambda$  and  $\Sigma^0$  show up in the distribution. This can be later on used for further selections. For this purpose, these two peaks were fitted with four Gaussians, two for each peak to take signal broadening from scattering in the detector system into account. The  $\sigma$  values of these fits are, thereby, the amplitude weighted averages of the standard deviations from the according two Gaussians. The lower border of the  $\Lambda$ -selection was then defined by the  $3\sigma$  interval with respect to the  $\Lambda$ -Gaussian mean, while the upper border of the cut was confined by the intersection of the  $\Lambda$ -Gaussians and the  $\Sigma^0$ -Gaussians. Accordingly, the  $\Sigma^0$ -selection reaches from the intersection to the  $3\sigma$  limit determined by the  $\Sigma^0$ -Gaussians. Another peak appears in the  $MM(p, \pi^+, \pi^-, \pi^+)$  that corresponds to the missing neutron, which stems from the reaction  $p + p \rightarrow \Sigma^+ + p + K^0$  (Ch. 4.30). Furthermore, this neutron peak arises to some extent from the reaction  $p + p \rightarrow p + \pi^+ + \pi^+ + \pi^- + n$ .

A second missing mass distribution was studied to distinguish between the reactions  $p + p \rightarrow \Sigma^+ + p + K^0$  and  $p + p \rightarrow \Sigma(1385)^+ + p + K^0$ , which is the missing mass to the three particles proton,  $\pi^+$  and  $\pi^-$ . Respective enhancements at the specific masses are seen in Figure 4.2 panel (b). The other  $K^0$  production channels have a rather broad

structure in this observable. However, another peak is visible that originates from the reaction  $p + p \rightarrow p + p + \pi^+ + \pi^-$ , which can contribute in this data sample, when a proton is misidentified as a  $\pi^+$ .

The third missing mass spectrum is essentially the same as the first  $MM(p, \pi^+, \pi^-, \pi^+)$ . However, a cut on the  $MM(p, \pi^+, \pi^-)$  was applied in addition accepting only events with  $MM(p, \pi^+, \pi^-) > 1270 \text{ MeV}/c^2$ . This way the reaction  $p + p \rightarrow \Sigma^+ + p + K^0$  was rejected leading to the missing mass distribution in Figure 4.2 panel (c), which is addressed as  $MM(p, \pi^+, \pi^-, \pi^+)_{CUT}$  in the following. The reason to include this spectrum in the analysis was to get rid of the  $p + p \rightarrow \Sigma^+ + p + K^0$  inside the neutron peak. As a consequence, only non-strange reactions contribute at  $MM(p, \pi^+, \pi^-, \pi^+)_{CUT} < 1000 \text{ MeV}/c^2$ , which facilitates a constraint on the yield of the background model.

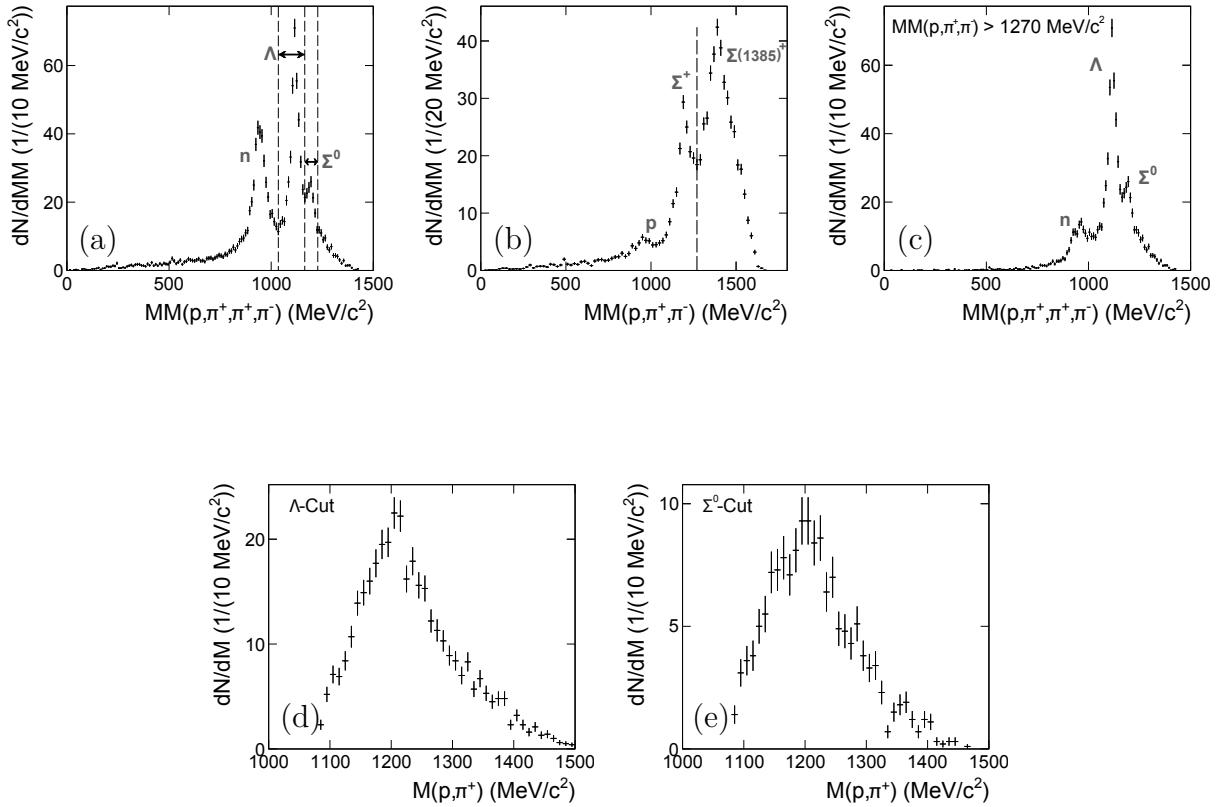


**Figure 4.2:** Missing mass distributions in panel (a) with respect to the  $p$ ,  $\pi^+$ ,  $\pi^+$  and  $\pi^-$ , in panel (b) with respect to the  $p$ ,  $\pi^+$  and  $\pi^-$ , and in panel (c) with respect to the  $p$ ,  $\pi^+$ ,  $\pi^+$  and  $\pi^-$  with the cut  $MM(p, \pi^+, \pi^-) > 1270 \text{ MeV}/c^2$  indicated in panel (b) as dashed line. Panel (d) and (e) show the  $p\pi^+$ -invariant mass distributions with applied  $\Lambda$ - or  $\Sigma^0$ -selection, respectively. All spectra are plotted with a cut on the  $K_S^0$  mass in the  $\pi^+\pi^-$ -invariant mass spectrum (Fig. 4.1). The double arrows in panel (a) indicate the so-called  $\Lambda$ -cut and  $\Sigma^0$ -cut, respectively.

After the definition of observables, in which  $\Lambda$  associated reactions can be separated from  $\Sigma^0$  associated reactions and  $\Sigma^+$  from  $\Sigma(1385)^+$  channels, further variables had to be found, in which the resonant  $\Delta^{++}$  reactions could be distinguished from the non-resonant reactions producing directly  $p\pi^+$ -pairs. Therefore, the two  $p\pi^+$ -invariant mass spectra  $M(p,\pi^+)_{\Lambda}$  and  $M(p,\pi^+)_{\Sigma^0}$  with either the  $\Lambda$ -cut or the  $\Sigma^0$ -cut on the variable  $MM(p,\pi^+,\pi^-\pi^+)$  were selected and are illustrated in Figure 4.2 panel (d) and (e). Since the proton and the  $\pi^+$  would be correlated, if they would stem from the  $\Delta^{++}$  decay, an enhancement would be seen in these invariant mass spectra at the specific  $\Delta^{++}$  mass, whereas uncorrelated  $p\pi^+$ -pairs would show a broad structure. However, the  $\Delta^{++}$  signal will not be a narrow peak, which is only a few  $\text{MeV}/c^2$  broad, but has a rather broad Breit-Wigner shape with a  $\Gamma$  of about 117  $\text{MeV}$ , which is due to its very short lifetime in the order of  $10^{-24}$  s [O<sup>+</sup>14]. Hence, a simple fit of the spectra like in the case of the  $K_S^0$  could not be applied without producing large systematic uncertainties. Therefore, a different method to extract the contributions was developed, in which all contributions were simulated or modeled and fitted simultaneously to these five introduced distributions by means of a  $\chi^2$  minimization. More details about this procedure are available in the next sections.

The mass spectra in Figure 4.2 are nicely suited to study the contribution of the  $K_S^0$  production channels without ambiguities. However, this analysis aims also for the extraction of the angular distributions of the resonant channels  $p + p \rightarrow \Lambda/\Sigma^0 + \Delta^{++} + K^0$ . Therefore, two angular distributions of the  $p\pi^+$ -system ( $\cos\Theta_{c.m.}^{p\pi^+}$ ) were studied as well and are plotted in Figure 4.3. The distribution in panel (a) contains  $\Lambda$ -events, while the spectrum in panel (b) passed through a  $\Sigma^0$ -selection.

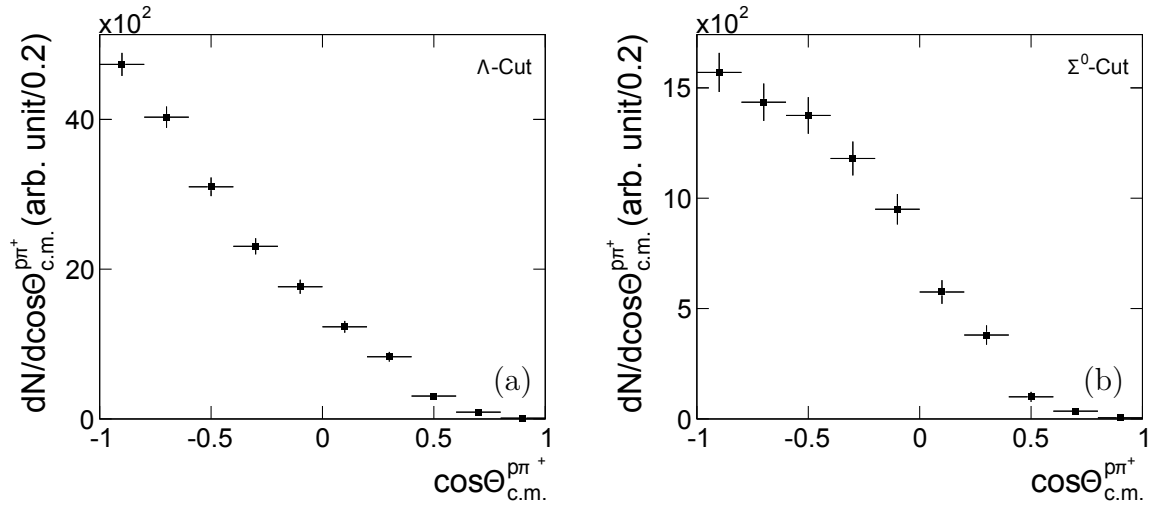


**Figure 4.3:** Angular distributions of  $p\pi^+$ -pairs in the center of mass reference system either in the  $\Lambda$ -cut (panel (a)) or in the  $\Sigma^0$ -cut (panel (b)) with a cut on the  $K_S^0$  mass in the  $\pi^+\pi^-$ -invariant mass spectrum (Fig. 4.1).

**Table 4.1:** Some possible non-strange reactions contributing to the final state selected in this analysis.

Non-strange reactions in selected events
$p + p \rightarrow p + n + \pi^+ + \pi^+ + \pi^-$
$p + p \rightarrow p + p + \pi^+ + \pi^+ + \pi^- + \pi^-$
$p + p \rightarrow p + p + \pi^+ + \pi^-$
$p + p \rightarrow p + p + \eta$

### 4.1.3 Background Determination

As mentioned above, a rather large amount of background remains in the selected data sample even after target, off-vertex and the  $K_S^0$  mass cut meaning also in the missing mass and invariant mass distributions introduced in the last section. This background contains mainly combinatorial background from non-strange reactions, of which some are listed in Table 4.1. Since only less than 0.3% of the events are used more than one time, the combinatorial background from  $K_S^0$  production channels can be neglected. However, a much longer list of non-strange reactions than listed in Table 4.1 contribute in the data sample, from which one would need to know the cross sections and kinematical distributions, if the background should be modeled by simulations. This is obviously not the case, which is why a data-driven sideband analysis was performed to emulate the background. In such an analysis a sample of experimental background events is defined by selecting a  $\pi^+\pi^-$ -invariant mass outside the  $3\sigma$   $K_S^0$  region. The invariant mass regions covered by this sample are indicated as red (LM, low mass) and green (HM, high mass) areas in Figure 4.1 and are chosen as large as possible while keeping the integral of both areas similar. In the following, the terms background, background events or  $K_S^0$  background will be denoted to events with an  $\pi^+\pi^-$ -invariant mass inside the  $3\sigma$   $K_S^0$  window, while the background events with a  $\pi^+\pi^-$ -invariant mass outside  $3\sigma$   $K_S^0$  region the will be addressed as  $K_S^0$  sideband events.

The aim of the sideband analysis is to model the full kinematics of the  $K_S^0$  background with help of the sideband events. Thereby, the easiest way was to adjust the  $\pi^+\pi^-$ -momentum distribution of the sideband sample to the background momentum distribution. A pure background sample could be obtained by a cut on  $MM(p, \pi^+, \pi^-) < 1100$  MeV/c<sup>2</sup>. This cut is plotted in Figure 4.4 as a dotted line. In the same plot, which shows the experimental  $MM(p, \pi^+, \pi^-)$  distribution overlaid by  $K_S^0$  Monte Carlo simulations (more details in next section), one can notice that no  $K_S^0$  reaction contributes at lower masses than this dotted cut-line. The resulting  $\pi^+\pi^-$ -momentum distribution of such events is depicted in Figure 4.5 and marked as black squares. The momentum distributions of both sideband samples,  $p_{LM}^{\pi^+\pi^-}$  and  $p_{HM}^{\pi^+\pi^-}$ , were then fitted to the one of the  $K_S^0$  background by adjusting the yields of the distributions according to:

$$N_{BG} = a \cdot N_{LM} + b \cdot N_{HM} \quad (4.32)$$

with

- $N_{BG}$  : yield of the  $K_S^0$  background
- $N_{LM}$  : yield of the low mass sideband sample
- $N_{HM}$  : yield of the high mass sideband sample
- $a, b$  : fit coefficients

Thereby, the starting values of the fit coefficients  $a$  and  $b$  were both set to one to reflect the nearly same integrals of the LM and the HM sideband samples. As a result a  $\chi^2/NDF$  of 2.32 was achieved. The outcome is also shown in Figure 4.5, where  $p_{LM}^{\pi^+\pi^-}$  is plotted as red filled triangles,  $p_{HM}^{\pi^+\pi^-}$  as green open triangles together with the sum of both (gray shaded area). A satisfactorily good agreement of the  $\pi^+\pi^-$ -momentum distributions was obtained and thus also the relative scaling factors that need to be applied on the LM and HM events. Furthermore, it was seen that the LM sideband sample had to be scaled more than the HM events ( $a > b$ ), which was expected, because the  $K_S^0$  background is not constant over the  $\pi^+\pi^-$ -invariant mass, but decreases with growing invariant mass.

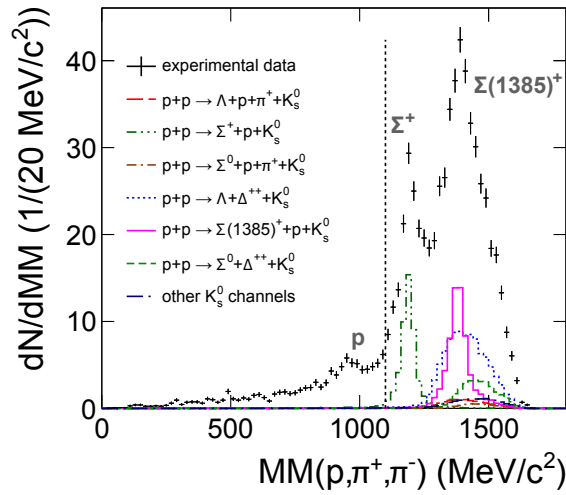


**Figure 4.4:** Missing mass distribution with respect to the  $p$ ,  $\pi^+$  and  $\pi^-$ , both with a cut on the  $K_S^0$  mass in the  $\pi^+\pi^-$ -invariant mass spectrum (Fig. 4.1). The dotted line at 1100  $\text{MeV}/c^2$  is used in the sideband analysis for a background selection.

This momentum distribution was cross-checked differentially in the polar angle  $\Theta_{lab}^{\pi^+\pi^-}$ , which is kinematically independent from  $p_{lab}$  and hence allows to display the full  $\pi^+\pi^-$ -kinematics. Figure 4.6 shows the  $\pi^+\pi^-$ -momentum spectra in five  $\Theta_{lab}^{\pi^+\pi^-}$  bins ranging from  $0^\circ$  to  $75^\circ$  with the same conditions as for the total  $\pi^+\pi^-$ -momentum distribution. The color code is the same as before, while the scaling factors for LM and HM events ( $a$  and  $b$ )

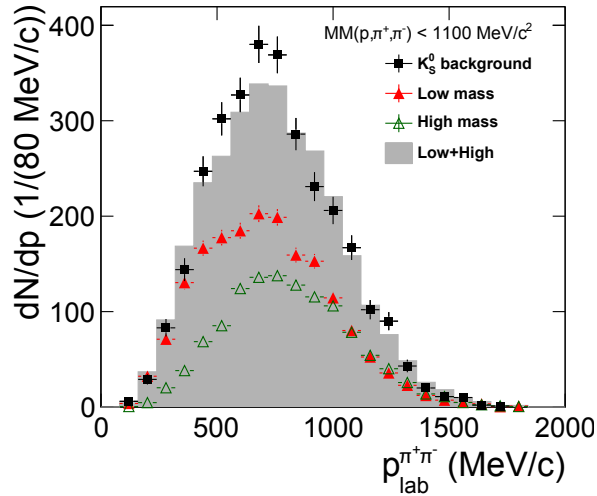


**Figure 4.5:** Momentum distribution of the  $K_S^0$  background (full squares). Applied conditions are a  $3\sigma$  cut around the  $K_S^0$  peak in the  $\pi^+\pi^-$ -invariant mass distribution (Fig. 4.1), and a cut on  $MM(p, \pi^+, \pi^-) < 1100 \text{ MeV}/c^2$ . Relative weights of low mass (full triangles) and high mass (open triangles) sideband samples were fitted simultaneously to the spectrum. The sum of both is shown as a gray filled histogram.

fixed by the fit to the total momentum spectrum were applied to the sideband distribution. The sum of the sideband samples reproduces the background distribution fairly well in all polar angle ranges ensuring that the sideband sample can be used as a background model in the kinematic observables shown in Figure 4.2 and 4.3.

#### 4.1.4 Simulation Cocktail

The data sample for this analysis was chosen such to enhance the relative contribution of certain  $K_S^0$  production channels by selecting events with the four charged particles proton,  $\pi^+$ ,  $\pi^+$  and  $\pi^-$ . This sample still contains background from non-strange reactions, which can be explained by the sideband sample introduced in Section 4.1.3. The contributing  $K_S^0$  reactions are listed to an almost complete extent in Table 4.2 and were simulated as an incoherent cocktail with the Pluto event generator [F<sup>+</sup>07] to study cross sections and angular distributions. This Monte Carlo tool is explained in detail in Section 2.4.1.

The list of considered  $K^0$  production channels found in Table 4.2 holds three different classifications of the reactions. The class C1 includes the main contributing  $K^0$  reactions, that this analysis focuses on and which already have been introduced in Section 4.1 listing all decay branches of each reaction. The classes C2 and C3 reflect the  $K^0$  channels that have a relatively low probability to pass the event selection due to their many-body final state. C2 reactions correspond to multi-pion  $K^0$  reactions, while the C3 class contains the remaining  $K^0$  channels. The reactions of these two classes C2 and C3 show very similar

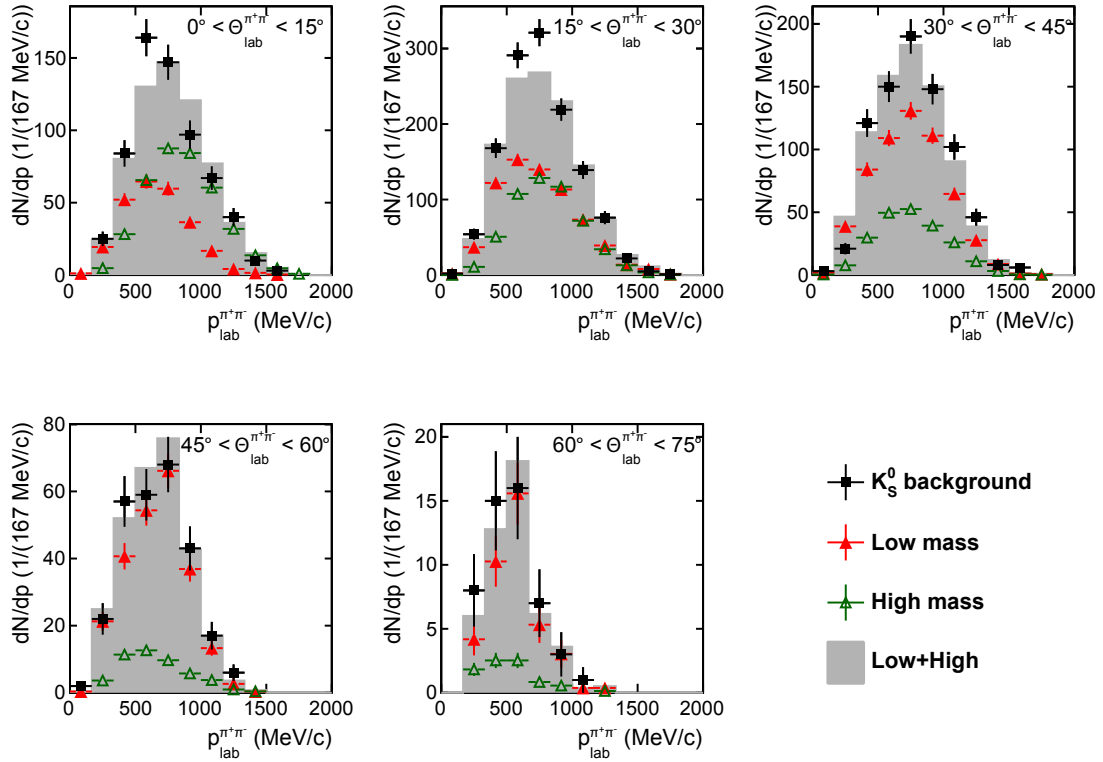


**Figure 4.6:** Momentum spectra for several bins in  $\Theta_{lab}$  of the  $K_S^0$  background. Applied conditions are a  $3\sigma$  cut around the  $K_S^0$  peak in the  $\pi^+\pi^-$ -invariant mass distribution (Fig. 4.1), and a cut on  $MM(p,\pi^+,\pi^-) < 1100 \text{ MeV}/c^2$ . The scaling of the low and high mass sideband is a result of the simultaneous fit of both sidebands to the momentum distribution of the  $K_S^0$  background in Fig. 4.5. The symbols are the same as in Fig. 4.5.

shapes in all the observables, that are studied in this analysis, within their class. Therefore, these reactions could be merged within the two groups and treated each as one single contribution in further studies, which allowed to reduce the number of free parameters in the fit. Anyway, the contributions of the C2 and C3 reactions in the studied data sample were so small that their determined cross sections are compatible with zero within the statistical uncertainties. Even in the case that some  $K^0$  reactions might be missing in this compilation, they will most probably be many-body reactions, which can be either grouped into class C2 or C3. However, two interesting reactions including a  $K^*(892)^+ \rightarrow K^0 + \pi^+$  were inspected explicitly to figure out, whether they need to be considered or not. Indeed, an ongoing inclusive  $K^*(892)^+$  analysis has shown enough statistics for double differential investigations. Both the reactions  $p+p \rightarrow \Lambda + p + K^*(892)^+$  ( $\varepsilon = 230 \text{ MeV}$ ) and  $p+p \rightarrow \Sigma^0 + p + K^*(892)^+$  ( $\varepsilon = 157 \text{ MeV}$ ) are above threshold in the considered p+p reaction at 3.5 GeV. Nevertheless, the invariant mass of the three selected pions showed that the geometrical acceptance for the  $K^*(892)^+$  is very small within the four-particle selection. This statement holds true for both reactions as can be seen in Figure 4.7, in which panel (a) shows the  $MM(\pi^+,\pi^-\pi^+)$  using the  $\Lambda$ -selection and panel (b) with the corresponding  $\Sigma^0$ -selection. The red dashed

**Table 4.2:**  $K^0$  production channels contributing to the selected final state. The cross sections  $\sigma_{ch}^{fit}$  at 3.5 GeV are determined by a fit with a cross section parametrization from [SC98] (Eq. 34) to experimental cross sections measured at other energies (\*no experimental data existing to perform the fit). The excess energies  $\varepsilon$  are calculated for p+p reactions at 3.5 GeV.

Main contributing reactions (C1)	$\sigma_{ch}^{fit}$ [ $\mu\text{b}$ ]	$\varepsilon$ [MeV]
$p + p \rightarrow \Sigma^+ + p + K^0$	20.43	551
$p + p \rightarrow \Lambda + p + \pi^+ + K^0$	18.40	485
$p + p \rightarrow \Sigma^0 + p + \pi^+ + K^0$	12.38	408
$p + p \rightarrow \Lambda + \Delta^{++} + K^0$	4.47	331
$p + p \rightarrow \Sigma^0 + \Delta^{++} + K^0$	-*	254
$p + p \rightarrow \Sigma(1385)^+ + p + K^0$	5.31	358
Multi-pion $K^0$ reactions (C2)	$\sigma_{ch}^{fit}$ [ $\mu\text{b}$ ]	$\varepsilon$ [MeV]
$p + p \rightarrow \Lambda + n + \pi^+ + \pi^+ + K^0$	5.08	344
$p + p \rightarrow \Lambda + p + \pi^+ + \pi^0 + K^0$	4.46	350
$p + p \rightarrow \Sigma^- + p + \pi^+ + \pi^+ + K^0$	3.75	264
$p + p \rightarrow \Sigma^+ + p + \pi^+ + \pi^- + K^0$	2.26	272
Other $K^0$ reactions (C3)	$\sigma_{ch}^{fit}$ [ $\mu\text{b}$ ]	$\varepsilon$ [MeV]
$p + p \rightarrow p + n + K^+ + \bar{K}^0$	7.58	307
$p + p \rightarrow \Sigma^+ + n + \pi^+ + K^0$	4.53	410
$p + p \rightarrow \Sigma^+ + p + \pi^0 + K^0$	4.06	416
$p + p \rightarrow \Sigma^+ + \Delta^+ + K^0$	6.59	257
$p + p \rightarrow p + p + \pi^+ + K^- + K^0$	2.02	169

lines in both histograms indicates the nominal mass of the  $K^*(892)^+$ . Since the  $K^*(892)$  has a width of only  $\Gamma \approx 50$  MeV [O<sup>+</sup>14], it is furthermore unlikely that it contaminates the shown invariant mass spectra. Ultimately, these reactions could be neglected in this analysis and were not included.

Finally, all the simulated reactions (Table 4.2) were processed through the HADES detector simulation using Geant3, tracked and analyzed with the same algorithms as used for the experimental data to obtain the three missing mass and two invariant mass spectra introduced in Section 4.1.2. The yields of these simulated distributions were then fitted simultaneously to the five experimental mass spectra by means of a  $\chi^2$  minimization, to determine the contribution of each class C1 reaction. In this minimization procedure start parameters for the scaling of each channel  $F_{ch}^{start}$  were defined taking the cross sections  $\sigma_{ch}^{fit}$  quoted in Table 4.2 normalized to the elastic p+p cross section as follows:

$$F_{ch}^{start} = \frac{\sigma_{ch}^{fit}}{N_{ch}^{sim}} \cdot \frac{N_{el}^{tot}}{\sigma_{el}}. \quad (4.33)$$

$N_{ch}^{sim}$  corresponds to the number of events simulated for each channel and the cross

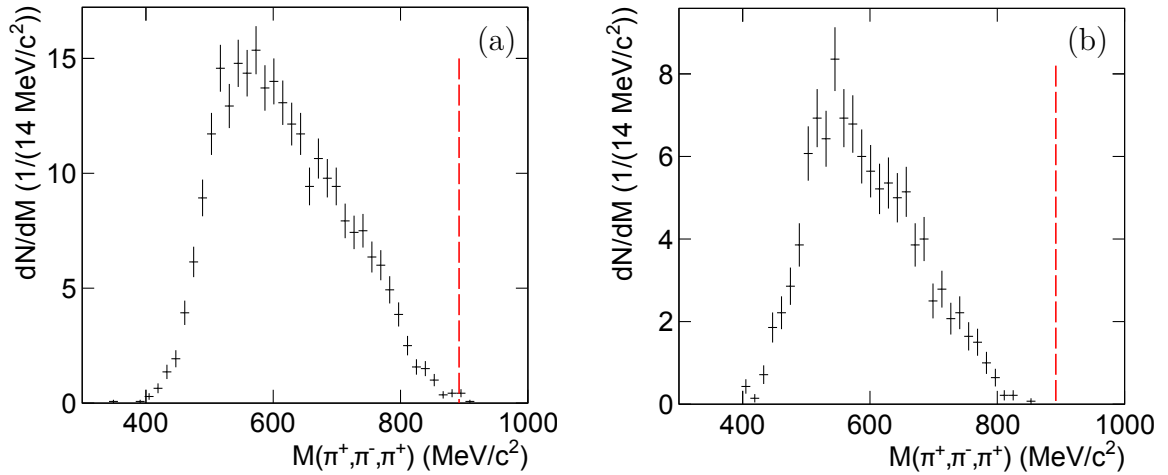


**Figure 4.7:** Invariant mass distribution of the three pions  $\pi^+$ ,  $\pi^+$  and  $\pi^-$  inside the four-particle event selection and including  $K_S^0$  off-vertex and  $K_S^0$  mass cuts. Panel (a) is selected for  $\Lambda$ -events and panel (b) for  $\Sigma^0$ -events using the relevant cuts in the  $MM(p, \pi^+, \pi^-, \pi^+)$  (Fig. 4.2, panel (a)). The red dashed lines indicate the nominal mass of a  $K^*$  (892).

sections  $\sigma_{ch}^{fit}$  were estimated from a fit to measured data for various beam energies using the parametrization from Eq. 34 in [SC98]. Figure 2.11 shows some fits as an example. It has to be mentioned that the quoted cross sections for the reaction  $p + p \rightarrow \Lambda + p + \pi^+ + K^0$  include also the contributions from the branching of the reactions  $p + p \rightarrow \Lambda + \Delta^{++} + K^0$  and  $p + p \rightarrow \Sigma(1385)^+ + p + K^0$  into the same final states. Indeed, most of the previous measurements did not distinguish among them.  $N_{el}^{tot}$  corresponds to the total number of elastic events, while  $\sigma_{el}$  is the cross section for elastic events in the analyzed data set. They have been extracted in a separate analysis found in [Rus10]. In principle, the ratio of these parameters relates the measured signal counts to cross sections and should stay constant for every investigated reaction. If one assumes that the quoted  $\sigma_{ch}^{fit}$  would be correct, one could obtain the number of events of each reaction, that should be measured in the experimental data sample by applying the factor  $F_{ch}^{start}$  to simulations. In this case acceptance and efficiency effects would already be considered, since the simulation was processed through a full-scale analysis. Additionally, the relative contributions of the LM and HM sideband samples were fixed by the sideband analysis (Sec. 4.1.3), but the total sideband contribution was allowed to vary within  $\pm 30\%$ . That was done, to take into account the fact that the yield of the sideband events was obtained on the basis of a small data sample due to the cut  $MM(p, \pi^+, \pi^-) < 1100 \text{ MeV}/c^2$  (see also Sec. 4.1.3). As a result the minimization process delivers scaling factors  $f_{ch}$  for each reaction to fulfill following condition:

$$N^{exp\_acc} = \sum_{ch} f_{ch} \cdot F_{ch}^{start} \cdot N_{ch}^{sim\_acc}, \quad (4.34)$$

where  $N^{exp\_acc}$  and  $N_{ch}^{sim\_acc}$  are related to the number of experimental and simulated events inside the HADES acceptance and including efficiency effects from tracking and analysis. In simple words, the minimization process varies the cross section  $\sigma_{ch}^{fit}$  by adjusting the

scaling factor  $f_{ch}$ , so that experimental data are described the best way. As a result quite different cross sections were obtained compared to the values of  $\sigma_{ch}^{fit}$ , which is mainly due to the separate consideration of resonant and non-resonant reactions. A detailed discussion on these findings can be found in Section 4.2.2.

Thereby, the assumption was made that the different channels were not interfering with each other. Indeed, channels ending up in the same final states might interfere, which means in this analysis that the non-resonant channels might interfere with the resonant channels:

- $p + p \rightarrow \Sigma^0 + p + \pi^+ + K^0$ ,  $p + p \rightarrow \Sigma^0 + \Delta^{++} + K^0$  and  
 $p + p \rightarrow \Sigma(1385)^+ + p + K^0 \rightarrow \Sigma^0 + \pi^+ + p + K^0$
- $p + p \rightarrow \Lambda + p + \pi^+ + K^0$ ,  $p + p \rightarrow \Lambda + \Delta^{++} + K^0$  and  
 $p + p \rightarrow \Sigma(1385)^+ + p + K^0 \rightarrow \Lambda + \pi^+ + p + K^0$

Nevertheless, the no-interference assumption is fairly reasonable, if one regards the missing mass and invariant mass spectra plotted in Figure 4.2. Indeed, from studies with a Partial Wave Analysis (PWA) of the same data set [A<sup>+</sup>15, Epp14], where interferences are taken into account, it was seen that interference effects would influence the invariant mass spectra leading to distorted distributions, which is not the case in this analysis. Furthermore, a clear peak of the  $\Sigma(1385)^+$  and the broad structure of the  $\Delta^{++}$  resonance were seen in the experimental data, which hint at dominant contributions from the resonant channels. These peak structures would wash out, if strong interferences would play a role.

### 4.1.5 Angular Anisotropy

After performing the minimization procedure on the five kinematical observables with the simulation cocktail described above (Fig. 4.2), it was found that the angular distributions of the  $p\pi^+$ -pairs separated for  $\Lambda$ - and  $\Sigma^0$ -events shown in Figure 4.3 could not be reproduced by the incoherent sum of the simulated  $K^0$  channels. Although that minimization delivered a reasonable  $\chi^2/NDF$  of 2.8 in the five mass spectra, the  $\chi^2/NDF$  calculated from both  $\cos\Theta_{cm}^{p\pi^+}$  distributions was 25.64. The large discrepancies can be observed in Figure 4.8, where the simulation completely failed to emulate the backward kinematics. The reason for that was found in the missing production anisotropies for several reactions, which had to be included. First of all angular anisotropies were incorporated in the simulation from previous measurements of the reactions  $p + p \rightarrow \Sigma^+ + p + K^0$  and  $p + p \rightarrow \Sigma(1385)^+ + p + K^0$ . The reaction  $p + p \rightarrow \Sigma^+ + p + K^0$  has been studied by the COSY-TOF Collaboration at a lower energy of  $E_{kin} = 2.26$  GeV, in which they have observed the anisotropic production of the emitted  $K_S^0$  [AB<sup>+</sup>12]. The extracted strength of the anisotropy has been quantified in terms of parameters of the Legendre polynomial function (Eq. 3.6), which are quoted in Table 4.3, and were used to weight the  $K_S^0$  in the corresponding simulated channel. Similarly the  $\Sigma(1385)^+$  was weighted using the determined Legendre polynomial coefficients from the investigation of the reaction  $p + p \rightarrow \Sigma(1385)^+ + n + K^+$  in the same data sample as the presented one [A<sup>+</sup>12b]. These coefficients are also listed in Table 4.3.

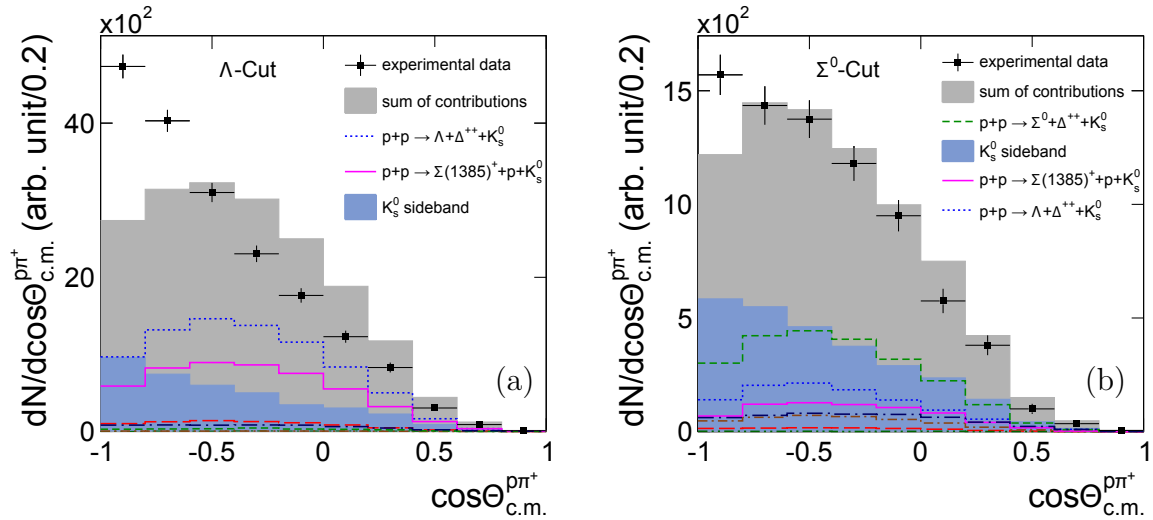


**Figure 4.8:** Angular distributions of  $p\pi^+$ -pairs in the center of mass reference system either in the  $\Lambda$ -cut (panel (a)) or in the  $\Sigma^0$ -cut (panel (b)) with a cut on the  $K_S^0$  mass in the  $\pi^+\pi^-$ -invariant mass spectrum (Fig. 4.1). The gray histogram corresponds to the sum of simulated isotropic contributions plus the background defined by the sideband sample. The same color code and line styles are used as in Figs. 4.10 and 4.11.

**Table 4.3:** Coefficients of the Legendre polynomials included for the angular distributions of the listed particles in the corresponding reactions. Coefficients of channel  $p+p \rightarrow \Sigma^+ + p + K^0$  are taken from [AB<sup>+</sup>12]. The coefficients for  $p+p \rightarrow \Sigma(1385)^+ + p + K^0$  was assumed to be the same as found in [A<sup>+</sup>12b] for the reaction  $p+p \rightarrow \Sigma(1385)^+ + n + K^+$ .

Reaction	cos	$A_0$ [ $\mu b$ ]	$A_1$ [ $\mu b$ ]	$A_2$ [ $\mu b$ ]	$A_2/A_0$
$p+p \rightarrow \Sigma^+ + p + K^0$	$\Theta_{cm}^{K^0}$	13.15	-0.40	4.37	0.33
$p+p \rightarrow \Sigma(1385)^+ + p + K^0$	$\Theta_{cm}^{\Sigma(1385)^+}$	7.23	0.00	10.24	1.42
$p+p \rightarrow \Lambda + \Delta^{++} + K^0$	$\Theta_{cm}^{\Delta^{++}}$	14.84	0.00	22.15	1.49
$p+p \rightarrow \Sigma^0 + \Delta^{++} + K^0$	$\Theta_{cm}^{\Delta^{++}}$	4.63	0.00	0.36	0.08

However, the simulation cocktail was still not able to reproduce the angular distributions of the  $p\pi^+$ -system, which pointed to missing angular anisotropies in further  $K^0$  production channels. Since an anisotropic production is more likely to occur in three-body than in many-body reactions and a dominant contribution was expected from the resonant channels, which lead to larger effects from these reactions, it was concluded that both reactions  $p+p \rightarrow \Lambda/\Sigma^0 + \Delta^{++} + K^0$  must carry some anisotropy - less in the  $\Sigma^0$  than in the  $\Lambda$  associated channel, as the discrepancy was larger in the  $\Lambda$ -selected distribution. To determine the strength of the anisotropies an iterative process was applied making use of the Legendre polynomial function to parametrize the angular distribution. The function is quoted in Equation 3.6, from which the  $A_1$  term was neglected, because the studied  $p+p$  system should not contain any asymmetric component. The  $\Delta^{++}$  in the two corresponding reactions were weighted assuming a certain combination of  $A_2$  coefficients,

which reflect the magnitude of the anisotropy, and processed through the minimization procedure on the five mass spectra. Thereby, the second coefficients were varied in the ranges  $A_2^{\Lambda\Delta^{++}K^0} = 20.65 - 23.65 \mu b$  and  $A_2^{\Sigma^0\Delta^{++}K^0} = -0.64 - 2.36 \mu b$  in steps of  $0.5 \mu b$ , while keeping the  $A_0$  coefficients constant at  $14.84$  and  $4.63 \mu b$ , respectively, which are related to the yield of the corresponding reactions. For each set of  $A_2$  parameters the  $\chi^2/NDF$  was calculated combining the two  $p\pi^+$ -angular distributions, which is depicted in Figure 4.9. This  $\chi^2/NDF$  distribution is highly sensitive on the variation of the anisotropy of the  $\Lambda$  associated reaction, whereas the  $\chi^2/NDF$  shows very little modification with the  $A_2$  alternation of the  $\Sigma^0$  reaction. However, a minimum could be found at  $A_2^{\Lambda\Delta^{++}K^0} = 22.15 \mu b$  and  $A_2^{\Sigma^0\Delta^{++}K^0} = 0.36 \mu b$  with  $\chi^2/NDF = 1.827$ . The values are summarized in Table 4.3 together with the  $A_2/A_0$  ratios for comparison. A rather strong anisotropy is obtained for the  $\Delta^{++}$ , if it is produced together with a  $\Lambda$ , while the formation in association with a  $\Sigma^0$  seems to be almost isotropic. The explanation about this finding will follow in the next section, when discussing the results of the exclusive analysis.

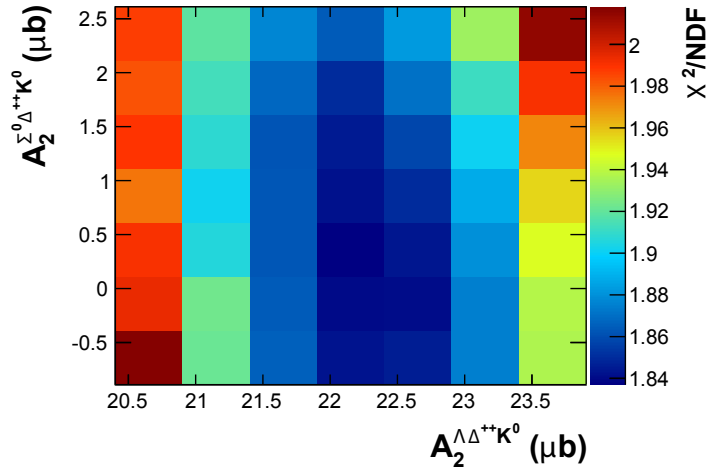


**Figure 4.9:**  $\chi^2/NDF$  distribution in the  $\cos \Theta_{cm}^{p\pi^+}$  spectra in Fig. 4.14 for the variation of the second coefficients  $A_2$  of the Legendre polynomials of the channels  $p + p \rightarrow \Lambda + \Delta^{++} + K^0$  and  $p + p \rightarrow \Sigma^0 + \Delta^{++} + K^0$ .

## 4.2 Results and Discussion

In this section results will be presented that were obtained in the four-particle selection (proton,  $\pi^+$ ,  $\pi^+$ ,  $\pi^-$ ) of the p+p data at a beam kinetic energy of 3.5 GeV. The data sample was filtered such to enhance contributions from  $K^0$  production channels, especially to study resonant reactions and their production dynamics. The analysis procedure is described in detail in the previous section.

### 4.2.1 Exclusive Contributions

One of the main goals of this exclusive analysis was to extract the contributions of resonant reactions that are produced in association with a neutral kaon. The data was studied in five different mass spectra, which allowed to distinguish between these channels listed in Table 4.2. As explained above, the simulated cocktail and the sideband sample, which was used to model the background, were simultaneously fitted to these five spectra delivering a scaling factor  $f_{ch}$  for each channel (C1) or channel class (C2 and C3). In the end, this scaling factor could be used to calculate the total cross section  $\sigma_{ch}^{tot}$  taking the cross sections  $\sigma_{ch}^{fit}$  into account, which were introduced as start parameters for the minimization process, as following:

$$\sigma_{ch}^{tot} = f_{ch} \cdot \sigma_{ch}^{fit} \quad (4.35)$$

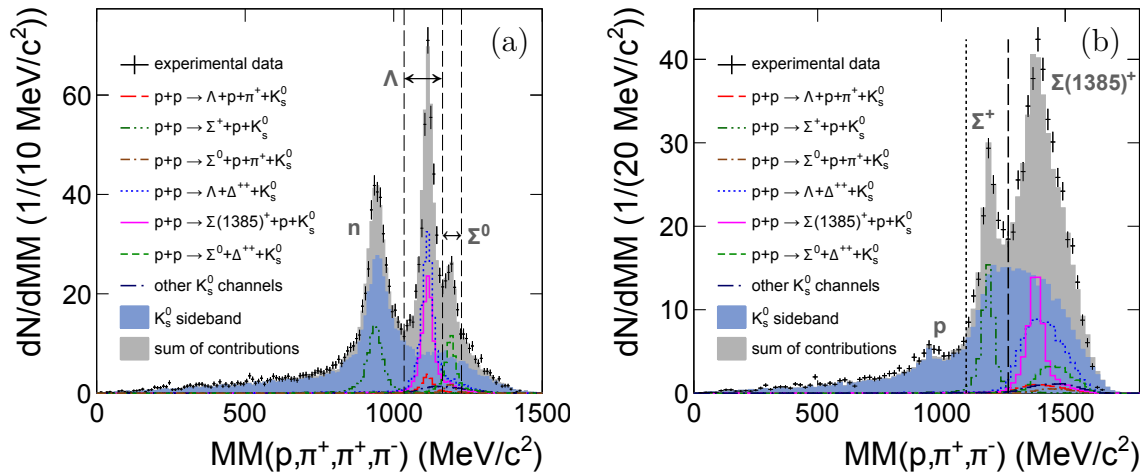


**Figure 4.10:** Missing mass distribution with respect to the p,  $\pi^+$ ,  $\pi^+$  and  $\pi^-$  in panel (a) and in panel (b) with respect to the p,  $\pi^+$  and  $\pi^-$ , both with a cut on the  $K_S^0$  mass in the  $\pi^+\pi^-$ -invariant mass spectrum (Fig. 4.1). The gray histogram corresponds to the sum of simulated contributions plus the background defined by the sideband sample. The double arrows in panel (a) indicate the so-called  $\Lambda$ -cut and  $\Sigma^0$ -cut, respectively. The dotted and dashed lines in panel (b) at 1100 MeV/c<sup>2</sup> and 1270 MeV/c<sup>2</sup> are used as cuts in other variables. See text for details.

The minimization converged with a  $\chi^2/NDF$  of 2.57, which already points out the good agreement of the fitted contributions to the experimental spectra. In Figure 4.10 one can find the missing mass spectrum to the four selected particles  $MM(p, \pi^+, \pi^-, \pi^+)$  in panel (a), while in panel (b) the missing mass to the proton,  $\pi^+$  and  $\pi^-$  is illustrated. The simulated  $K_S^0$  reactions scaled according to the parameters obtained from the minimization procedure are plotted as colored curves, the background model is shown as a blue filled area and the incoherent sum of all contributions is depicted in gray. Only the multi-pion reactions (C2) are not shown in the plots, since the resulting contribution ( $\approx 3.91 \cdot 10^{-7} \mu b$ ) is extremely small. First of all one can see that the sum of all contributions matches the experimental data very nicely in both distributions. All the peak structures together with their widths, that mainly originate from the HADES detector resolution, are in good agreement. Even the low mass tails together with the proton peak in the  $MM(p, \pi^+, \pi^-)$ , which are almost entirely background events and hence had to be modeled by the sideband sample, are fairly well reproduced. This is also visible in the  $MM(p, \pi^+, \pi^-, \pi^+)_{CUT}$  spectrum, which is plotted in Figure 4.11. Altogether, the background model covers more than half of the selected statistics, which was already reflected in the  $S/B$  ratio of 0.64 obtained from the  $\pi^+\pi^-$ -invariant mass distribution in Figure 4.1. However, a distinction between non-resonant and resonant reactions was not possible with these missing mass spectra, although the  $\Sigma(1385)^+$  reaction could be pretty well separated from the  $\Sigma^+$  reaction in the  $MM(p, \pi^+, \pi^-)$  and the  $\Lambda$  from the  $\Sigma^0$  reactions in the  $MM(p, \pi^+, \pi^-, \pi^+)$ . But for example the three reactions  $p + p \rightarrow \Lambda + \Delta^{++} + K^0$ ,  $p + p \rightarrow \Lambda + p + \pi^+ + K^0$  and  $p + p \rightarrow \Sigma(1385)^+ + p + K^0$  were mixed up in the  $\Lambda$ -peak of the four-particle missing mass distribution.

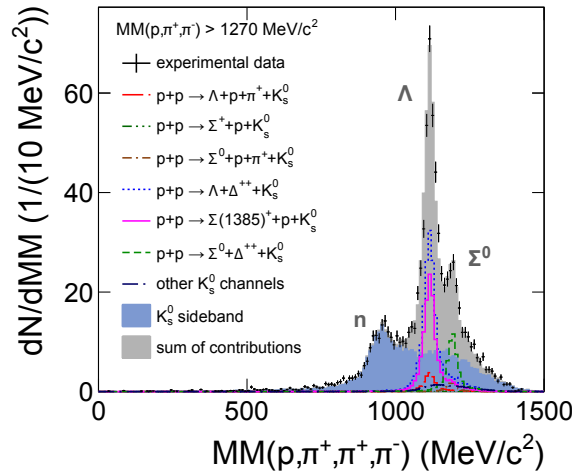


**Figure 4.11:** Missing mass distribution with respect to the  $p$ ,  $\pi^+$ ,  $\pi^+$  and  $\pi^-$  obtained after the cut  $MM(p, \pi^+, \pi^-) > 1270 \text{ MeV}/c^2$  and a cut on the  $K_S^0$  mass in the  $\pi^+\pi^-$ -invariant mass spectrum (Fig. 4.1). The gray histogram corresponds to the sum of simulated contributions plus the background defined by the sideband sample.

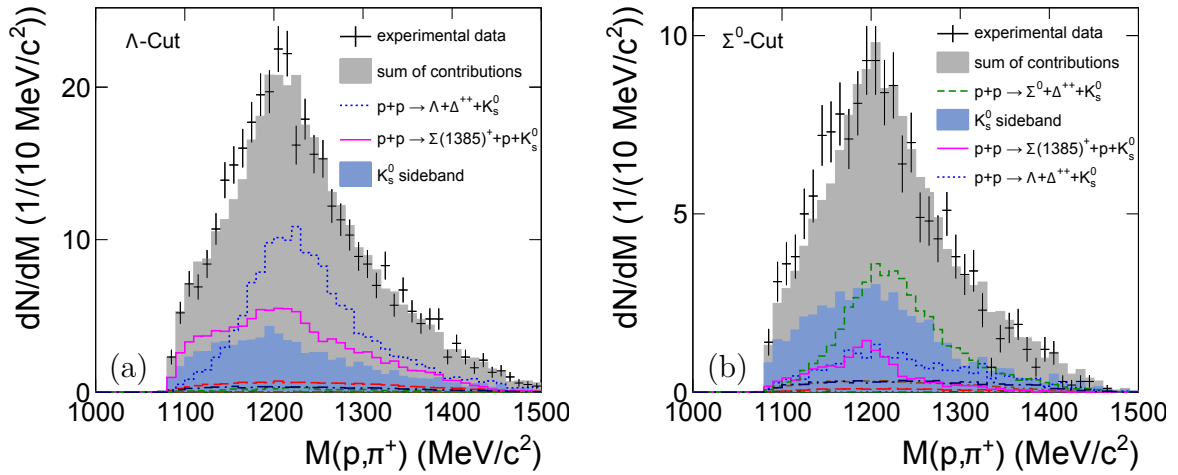


**Figure 4.12:**  $p\pi^+$ -invariant mass distribution after the  $\Lambda$ -cut (panel (a)) and  $\Sigma^0$ -cut (panel (b)) on the  $MM(p, \pi^+, \pi^+, \pi^-)$  distribution (Fig. 4.10 panel (a)) and with a cut on the  $K_S^0$  mass in the  $\pi^+\pi^-$ -invariant mass spectrum (Fig. 4.1). The gray histogram corresponds to the sum of simulated contributions plus the background defined by the sideband sample. The same color code and line styles are used as in Figs. 4.10 and 4.11.

Therefore, further observables were included in the minimization procedure, which are the  $p\pi^+$ -invariant mass spectra seen in Figure 4.12 subdivided into  $\Lambda$ - (panel (a)) and  $\Sigma^0$ -events (panel (b)). Also these spectra are quite well reproduced by the sum of the fitted contributions. As already suggested by the experimental spectra, most of the yield arise from the resonant reactions  $p + p \rightarrow \Lambda/\Sigma^0 + \Delta^{++} + K^0$ . Furthermore, a rather large contribution comes from the channel  $p + p \rightarrow \Sigma(1385)^+ + p + K^0$ , whereas the non-resonant reactions including the so-called “other  $K_S^0$ ” channels play a minor role. From Figure 4.12 panel (b) one can also notice that the  $\Sigma^0$ -selection did not work as efficiently as the  $\Lambda$ -selection, which is due to the  $MM(p, \pi^+, \pi^-, \pi^+)$  resolution. A rather large amount of  $\Lambda$  reactions still contributes in this spectrum. Nevertheless, this issue could be handled thanks to the minimization procedure, which fixed the contributions on five different observables at once. The necessity for a dominant production of the  $\Delta^{++}$  channels was checked in addition by presuming that the final states  $\Lambda + p + \pi^+ + K^0$  and  $\Sigma^0 + p + \pi^+ + K^0$  would originate only from non-resonant formation. In that sense, the full yields of the  $\Delta^{++}$  reactions were assigned to the corresponding non-resonant reactions. The resulting  $p\pi^+$ -invariant mass spectra can be found in Figure 4.13. Here, a significant worsening of the agreement between the model and the data is visible especially in panel (a), which depicts the  $\Lambda$ -events. This means in numbers a change of the  $\chi^2/NDF$  from 1.29 to 5.44 in the  $p\pi^+$ -invariant mass spectrum with a  $\Lambda$ -selection and from 2.44 to 3.55 in the  $\Sigma^0$ -spectrum. These observations confirm the statement that still at the measured kinetic beam energy of 3.5 GeV resonant productions are not only present but predominant.

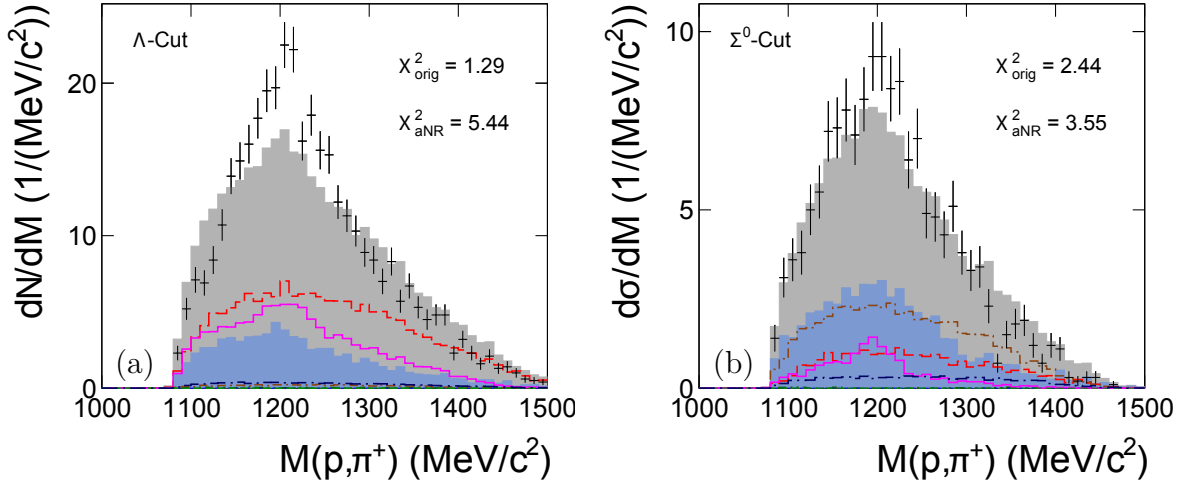


**Figure 4.13:**  $p\pi^+$ -invariant mass distribution after the  $\Lambda$ -cut (panel (a)) and  $\Sigma^0$ -cut (panel (b)) on the  $MM(p,\pi^+,\pi^+,\pi^-)$  distribution (Fig. 4.10 panel (a)) and with a cut on the  $K_S^0$  mass in the  $\pi^+\pi^-$ -invariant mass spectrum (Fig. 4.1). Full yields of the resonant  $\Delta^{++}$  reactions assigned to the non-resonant  $\Lambda/\Sigma^0 + p + \pi^+ + K^0$  reactions. The gray histogram corresponds to the sum of simulated contributions plus the background defined by the sideband sample. The same color code and line styles are used as in Figs. 4.10 and 4.11.

As described in Section 4.1.5 the yields of the background sample and the simulated  $K^0$  channels were fixed via a simultaneous fit to the five mass spectra discussed above, while incorporating angular anisotropies in four reactions ( $p + p \rightarrow \Sigma^+ + p + K^0$ ,  $p + p \rightarrow \Sigma(1385)^+ + p + K^0$ ,  $p + p \rightarrow \Lambda + \Delta^{++} + K^0$  and  $p + p \rightarrow \Sigma^0 + \Delta^{++} + K^0$ ). Two angular distributions were taken from previous measurements [AB<sup>+</sup>12, A<sup>+</sup>12b] and the anisotropies from the  $\Delta^{++}$  reactions were determined in the presented analysis. Only by taking them into account a reasonable agreement could be achieved in the angular distributions in the  $p\pi^+$ -system, which are plotted in Figure 4.14 for the  $\Lambda$ -events in panel (a) and for the  $\Sigma^0$ -events in panel (b). The color code for the model is the same as for the mass spectra. When comparing these plots with the distributions seen in Figure 4.8, in which all the simulations were produced isotropically, one can recognize immediately that the backward angles can be described much better, if the angular anisotropies are included. Hereby, a rather strong anisotropy was needed for the  $\Delta^{++}$  produced together with a  $\Lambda$ , while for its formation with a  $\Sigma^0$  only a weak anisotropy was compatible. The obtained Legendre polynomial parametrization is as follows for the first case:

$$F(\cos\Theta_{cm}^{\Delta^{++}}) = 14.84\mu b + 22.15\mu b \cdot \frac{1}{2}(3\cos^2\Theta_{cm}^{\Delta^{++}} - 1). \quad (4.36)$$

And for the reaction  $p + p \rightarrow \Sigma^0 + \Delta^{++} + K^0$  the parametrization of the  $\Delta^{++}$  angular anisotropy was found to be:

$$F(\cos\Theta_{cm}^{\Delta^{++}}) = 4.63\mu b + 0.36\mu b \cdot \frac{1}{2}(3\cos^2\Theta_{cm}^{\Delta^{++}} - 1). \quad (4.37)$$

Such a behavior of the angular anisotropy, which is dependent on the hyperon produced in the final state, was already discovered by the COSY-TOF Collaboration while studying the reactions  $p + p \rightarrow \Lambda/\Sigma^0 + p + K^+$  at  $p_{beam} = 3059$  MeV/c [AB<sup>+</sup>10] and can be interpreted as a consequence of the different production mechanisms involving intermediate  $N^*$  and  $\Delta^*$  resonances to form a  $\Sigma K$ - or  $\Lambda K$ -pair, while the latter cannot be generated through  $\Delta^*$ .

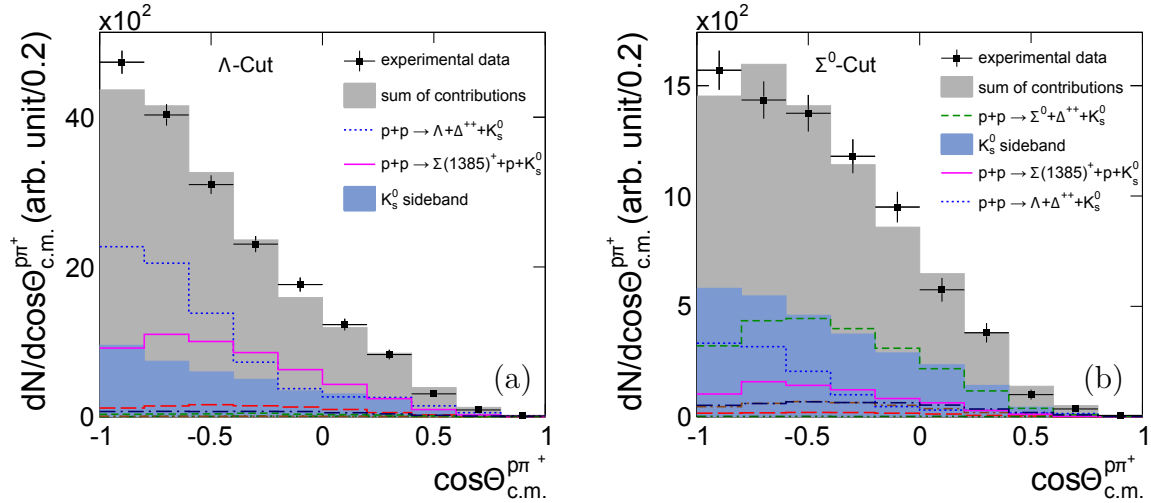


**Figure 4.14:** Angular distributions of  $p\pi^+$ -pairs in the center of mass reference system either in the  $\Lambda$ -cut (panel (a)) or in the  $\Sigma^0$ -cut (panel (b)) with a cut on the  $K_S^0$  mass in the  $\pi^+\pi^-$ -invariant mass spectrum (Fig. 4.1). The gray histogram corresponds to the sum of simulated contributions plus the background defined by the sideband sample. The same color code and line styles are used as in Figs. 4.10 and 4.11.

Since the model consisting of the simulated  $K^0$  cocktail and the sideband sample to emulate the background describes all the kinematic distributions fairly well, a correction of the detector acceptance and analysis efficiency could be performed on the angular distributions making use of this model. For this purpose, the experimental  $\cos\Theta_{cm}^{p\pi^+}$  spectrum for the reactions  $p + p \rightarrow \Lambda + \Delta^{++} + K^0$  and  $p + p \rightarrow \Lambda + p + \pi^+ + K^0$  in Figure 4.14 panel (a) was prepared by subtracting all other simulated reactions and the background model. The angular distribution of the reactions  $p + p \rightarrow \Sigma^0 + \Delta^{++} + K^0$  and  $p + p \rightarrow \Sigma^0 + p + \pi^+ + K^0$  in Figure 4.14 panel (b) was obtained accordingly. Of course, the requirement for this procedure was that the yields and the angular anisotropies incorporated for the  $\Sigma^+$  and  $\Sigma(1385)^+$  channels were correct. Otherwise, a model independent correction would also not be possible in this one-dimensional kinematic observable. However, the correction could be applied under the assumption that the  $\Sigma^+$  and  $\Sigma(1385)^+$  channels were modeled correctly and that a one-dimensional acceptance and efficiency correction does approximately work. The correction that needed to be applied to the experimental spectra was determined from the simulation of the two  $\Delta^{++}$  reactions and the two corresponding non-resonant reactions by comparing their acceptance and efficiency filtered to their initial distributions. The result overlaid with the simulated reactions can be found in Figure 4.15, in which panel (a) shows the  $\Lambda$  associated channels and panel (b) the channels linked to  $\Sigma^0$ . The figures include the systematic uncertainties identified by a permutation of the  $K_S^0$  off-vertex cuts

by  $\pm 20\%$  as it was done in the inclusive  $K_S^0$  analysis (see Table 3.2) and by a variation of the integral in the  $\pi^+\pi^-$ -invariant mass, which defined the sideband sample, again by  $\pm 20\%$ . Although the uncertainties in some bins are rather large, it is clearly visible that the  $p\pi^+$ -angular distribution of the  $\Lambda$  reactions favor a strong backward forward anisotropy, whereas the  $p\pi^+$ -system of the  $\Sigma^0$  reactions is produced nearly isotropically.

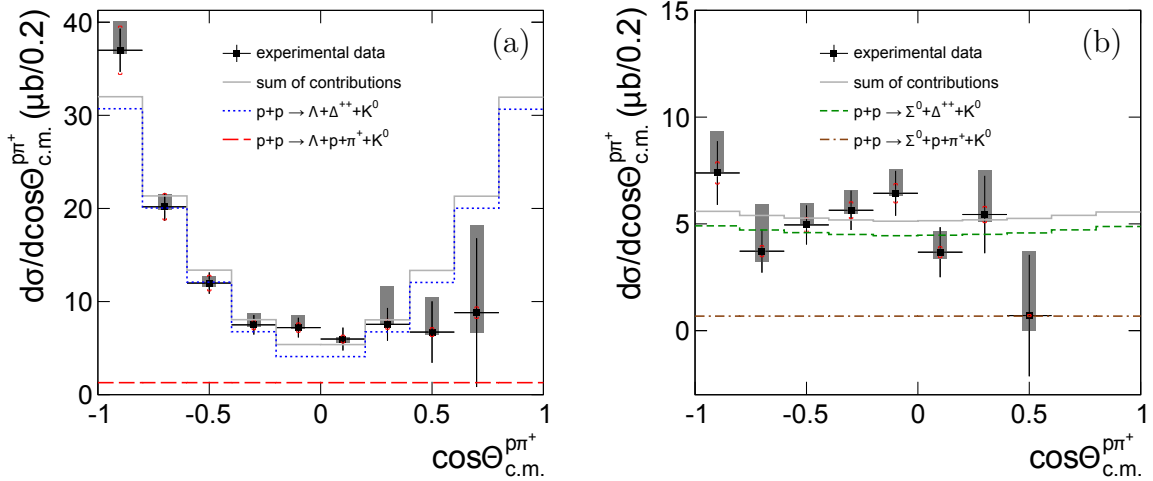


**Figure 4.15:** Absolute normalized angular distributions of  $p\pi^+$ -pairs in the center of mass reference system corrected for acceptance and efficiency. Panel (a) includes contributions from the reactions  $p + p \rightarrow \Lambda + (p + \pi^+)/\Delta^{++} + K^0$  and panel (b) from the reactions  $p + p \rightarrow \Sigma^0 + (p + \pi^+)/\Delta^{++} + K^0$ . The gray histogram corresponds to the sum of simulated contributions. The gray bands are the systematic uncertainties, whereas the red cups indicate the 7% uncertainty from the absolute normalization to elastic scattering cross sections [Rus10].

## 4.2.2 Exclusive Cross Sections

From the simultaneous fit of the model contributions to the three missing mass and two invariant mass spectra (Figs. 4.10, 4.11 and 4.12) it was possible to determine the relative yields of each fitted component to the experimental data. Therefore, the absolute cross sections of the  $K^0$  channels could be extracted from Equation 4.35 using the scaling factors  $f_{ch}$  obtained from this minimization process and are listed in Table 4.4. The Table quotes also uncertainties in the following sequence: Statistical uncertainties, that were calculated relative to the experimental uncertainties; systematic uncertainties, that were determined equally to the corrected angular distributions in Figure 4.15 through the variation of the  $K_S^0$  secondary vertex cuts by  $\pm 20\%$  (see Table 3.2) and by modifying the integral in the  $\pi^+\pi^-$ -invariant mass spectrum used for the sideband sample again by  $\pm 20\%$ ; and systematic uncertainties originating from the normalization to the elastic cross section [Rus10], which is always  $\pm 7\%$  from the measured value. Furthermore, the cross sections are shown for the two cases, when assuming isotropic productions of all channels and when including angular anisotropies for the reactions  $p + p \rightarrow \Lambda + \Delta^{++} + K^0$ ,  $p + p \rightarrow \Sigma^0 + \Delta^{++} + K^0$ ,  $p + p \rightarrow \Sigma^+ + p + K^0$  and  $p + p \rightarrow \Sigma(1385)^+ + p + K^0$  (see Sec. 4.1.5) to be able to

reproduce the  $p\pi^+$ -angular distributions (Fig. 4.14). The cross sections for the multi-pion reactions (C2) are not listed, since their contribution to the selected data sample were too small to extract a definite number. For the group of “other  $K^0$ ” reactions (C3) a reduction of their summed cross sections by a factor 0.82 was observed.

**Table 4.4:** Cross sections of the exclusive  $K^0$  reactions. Here  $\sigma_{anisotropic}$  means that the four channels listed in Table 4.3 include an anisotropic angular distribution, while  $\sigma_{isotropic}$  means that all channels were simulated isotropically. The first uncertainties correspond to statistical errors from the experimental data. The second uncertainties are the systematic errors from the variation of  $K_S^0$  secondary vertex cuts by  $\pm 20\%$  and the variation of the integral in the  $\pi^+\pi^-$ -invariant mass distribution used for the sideband sample by again  $\pm 20\%$ . The third uncertainties stem from the systematic uncertainties of the normalization to the elastic cross section [Rus10].

$K^0$ reactions	$\sigma_{isotropic} [\mu b]$	$\sigma_{anisotropic} [\mu b]$
$p + p \rightarrow \Sigma^+ + p + K^0$	$24.25 \pm 0.63_{-1.80}^{+2.42} \pm 1.70$	$26.27 \pm 0.64_{-2.13}^{+2.57} \pm 1.84$
$p + p \rightarrow \Lambda + p + \pi^+ + K^0$	$2.37 \pm 0.02_{-2.35}^{+0.18} \pm 0.17$	$2.57 \pm 0.02_{-1.98}^{+0.21} \pm 0.18$
$p + p \rightarrow \Sigma^0 + p + \pi^+ + K^0$	$1.40 \pm 0.02_{-1.40}^{+0.41} \pm 0.10$	$1.35 \pm 0.02_{-1.35}^{+0.10} \pm 0.09$
$p + p \rightarrow \Lambda + \Delta^{++} + K^0$	$25.56 \pm 0.08_{-1.45}^{+1.85} \pm 1.79$	$29.45 \pm 0.08_{-1.46}^{+1.67} \pm 2.06$
$p + p \rightarrow \Sigma^0 + \Delta^{++} + K^0$	$9.17 \pm 0.05_{-0.11}^{+1.45} \pm 0.64$	$9.26 \pm 0.05_{-0.31}^{+1.41} \pm 0.65$
$p + p \rightarrow \Sigma(1385)^+ + p + K^0$	$13.15 \pm 0.05_{-2.07}^{+1.91} \pm 0.92$	$14.35 \pm 0.05_{-2.14}^{+1.79} \pm 1.00$

First of all, one can see that the cross sections are sensitive to the angular distributions, at least the ones from the reactions, which were weighted with angular anisotropy. It makes a difference especially for the cross section of the reaction  $p + p \rightarrow \Lambda + \Delta^{++} + K^0$ , which changes by almost 15.22% with respect to the isotropic value. Therefore, one can conclude that not only the cross sections, but also the correct angular distributions need to be implemented in theoretical models. Furthermore, the numbers confirm what was already observed from the figures. The resonant reactions play a major role in this p+p data sample measured at the kinetic beam energy of 3.5 GeV, which reflects in a ten times higher cross section of the reaction  $p + p \rightarrow \Lambda + \Delta^{++} + K^0$  compared to its non-resonant equivalent and a six times larger production yield in the case, if a  $\Sigma^0$  is formed. Actually, if the uncertainties are taken into account, it is not even sure, whether non-resonant productions are needed at all. Moreover, the cross sections of the reaction  $p + p \rightarrow \Sigma^+ + p + K^0$  and  $p + p \rightarrow \Sigma(1385)^+ + p + K^0$  could be determined in this analysis, which have comparable contributions to the resonant  $\Delta^{++}$  channels.

Furthermore, it is interesting to compare the extracted cross sections to the starting values of the minimization procedure (see Table 4.2), since they were obtained with help of other experimental measurements. However, large differences are observed. At first one has to recall the circumstances of how these start values were determined. For instance, when the measured cross sections of the reactions  $p + p \rightarrow \Lambda/\Sigma^0 + p + \pi^+ + K^0$  at other beam energies were fitted with a parametrization according to phase space [SC98] (Fig. 2.11, panel (a) and (c)), the non-resonant as well as the resonant cross sections of channels with the particular final states were summed up (see Sec. 2.4.2). Therefore, the fitted cross sections of these

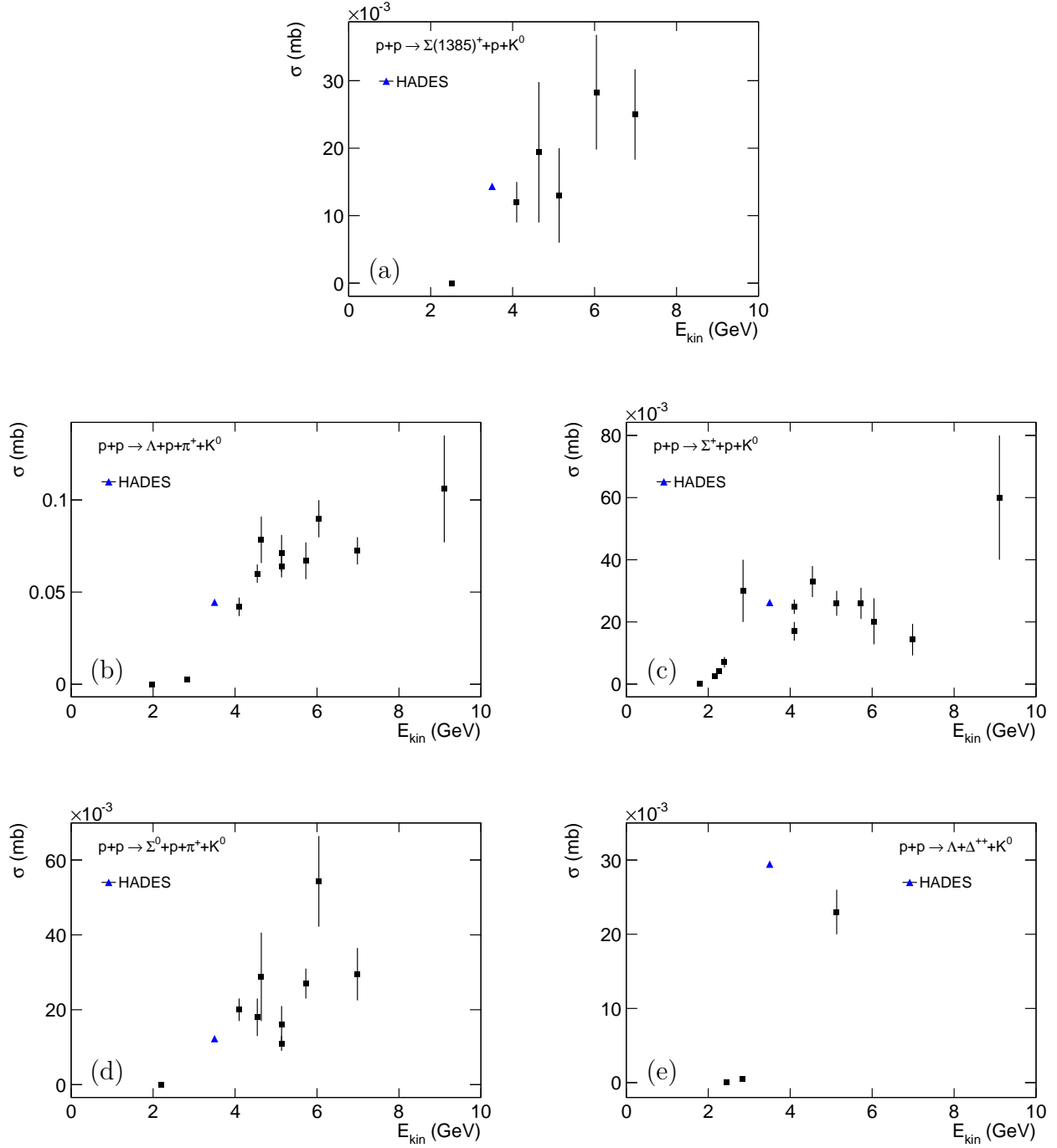


**Figure 4.16:** Experimentally measured cross sections [MS88, N<sup>+</sup>07, AB<sup>+</sup>12, A<sup>+</sup>14a] as a function of kinetic beam energy for the quoted reactions. The blue triangles correspond to the cross sections determined in this analysis with statistical uncertainties (smaller than the symbol). The first entries indicate the threshold energies.

two reactions ( $\sigma_{\Lambda p \pi^+ K^0}^{fit} = 18.40 \mu b$ ,  $\sigma_{\Sigma^0 p \pi^+ K^0}^{fit} = 12.38 \mu b$ ) are rather large and are not directly comparable with the exclusively extracted values quoted in Table 4.4. However, one can use the same procedure with the determined cross sections and sum up the values of the reactions, which lead to the same final states taking also into account the branching of the reaction  $p + p \rightarrow \Sigma(1385)^+ + p + K^0$  ( $\Sigma(1385)^+ \rightarrow \Lambda + \pi^+$  87%,  $\Sigma(1385)^+ \rightarrow \Sigma^0 + \pi^+$  11.7%), to obtain comparable numbers. By doing so, the sum of the cross sections leading to the  $\Lambda + p + \pi^+ + K^0$  final states yields to  $44.50 \pm 0.09(stat) \mu b$ , while for the  $\Sigma^0$  production the sum amounts to  $12.29 \pm 0.06(stat) \mu b$ . In that sense, the cross sections extracted by the phase space parametrization still differ a lot from the here measured, which can be attributed to the uncertainties of the fit due to the large uncertainties of the measurements at higher energies and due to the lack of data at intermediate energies. Ultimately, the cross sections extracted in this analysis (blue triangles) were plotted together with the other measurements (black squares) in Figure 4.16 filling up the intermediate energy regime. Also here, the summed cross sections are plotted in panel (b) and (d) for the reactions  $p + p \rightarrow \Lambda/\Sigma^0 + p + \pi^+ + K^0$ . The HADES data points lie nicely in the trend of the other measurements except for the reaction  $p + p \rightarrow \Lambda + \Delta^{++} + K^0$ , which seems to be too high. However, only two further experiments have studied this reaction before so that a final judgment cannot be made. A plot for the reaction  $p + p \rightarrow \Sigma^0 + \Delta^{++} + K^0$  is not shown, since there are no other measurements to compare with meaning also that this cross section has been extracted for the first time.

### 4.3 Implementation of the Exclusive Cross Sections in Models

In the last sections the results have been shown including exclusive cross sections for resonant and non-resonant  $K^0$  reactions and angular distributions for the  $\Delta^{++}$  reactions. These results were adopted in the first instance in the Pluto model consisting of a  $K^0$  cocktail and compared to the results from the inclusive  $K_S^0$  analysis on an absolute scale. Thereby, the reaction  $p + p \rightarrow \Sigma^0 + \Delta^{++} + K^0$  was simulated in addition to the 13  $K^0$  channels used for acceptance and efficiency correction of the inclusive spectra (Table 2.2). And moreover, the angular distributions of the  $\Delta^{++}$  in the reactions  $p + p \rightarrow \Lambda/\Sigma^0 + \Delta^{++} + K^0$  were weighted according to Equations 4.36 and 4.37. Also the angular anisotropy of the  $\Sigma(1385)^+$  was incorporated to weight the reaction  $p + p \rightarrow \Sigma(1385)^+ + p + K^0$  (Table 4.3). As in Section 3.4, in which the 13 simulated  $K^0$  channels with the phase space cross sections (Table 2.2) were compared to data, the double differential kinematics  $p_t - y_{cm}$  and  $\cos\Theta_{cm} - p_{cm}$  were chosen for the same purpose. The corresponding plots can be found in the Figures 4.17 and 4.18. Although the Pluto cocktail with the fitted cross sections was already in a rather good agreement with the inclusive  $K_S^0$  spectra, quite some improvement can be observed, when the results of the exclusive analysis were implemented. This can be seen for example in the transverse momentum spectra, in which first of all the maxima have shifted 50-100 MeV/c higher and second, which is more pronounced, the yield in the rapidity bins farer away from mid-rapidity have increased leading to a much better description of the experimental

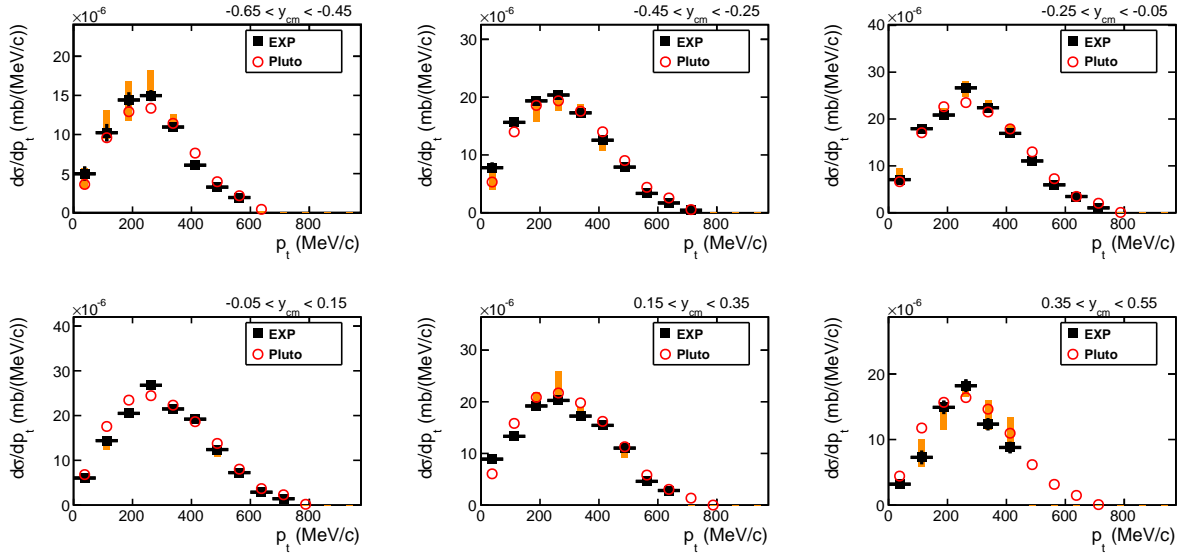


**Figure 4.17:** Comparison of the experimental  $K_S^0$   $p_t$ - $y_{cm}$  distributions (black squares) to a Pluto/Monte Carlo cocktail of 14  $K_S^0$  channels (red open circles) on an absolute scale. Exclusive cross sections and angular anisotropies were implemented. The experimental data includes statistical (black lines) and systematic uncertainties (orange bars).

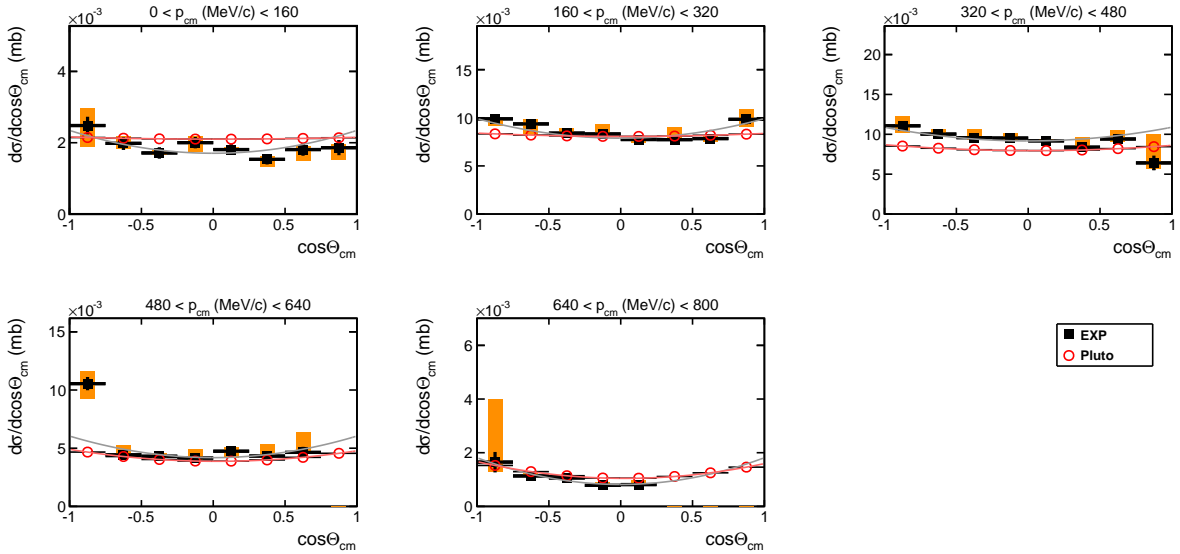


**Figure 4.18:** Comparison of the experimental  $K_S^0$  angular distributions (black squares) to a Pluto/Monte Carlo cocktail of 14  $K_S^0$  channels (red open circles) as a function of five  $p_{cm}$  bins. Exclusive cross sections and angular anisotropies were implemented. Both data sets are absolute normalized and fitted with a Legendre polynomial function (Eq. 3.6). The experimental data includes statistical (black lines) and systematic uncertainties (orange bars).

data. Furthermore, this improvement is visible in the angular distributions, which catch the observed angular anisotropy more precisely due to the inclusion of further anisotropic channels. The normalized second coefficient of a Legendre polynomial fit  $A_2/A_0$  confirms this observation (see Table 4.5). The ratio increased in all center-of-mass momentum bins relatively to the ratio extracted from the primary Pluto cocktail (Table 3.4) and is therefore closer to the experimental values, though discrepancies still remain. That suggests that further reaction channels might be produced anisotropic and/or intermediate resonances play also a role in other final states. Nevertheless, the overall good agreement of the Monte Carlo cocktail with the experimental data points out the rather plain physics, that is involved in p+p reactions, and confirms that there is no need to implement any extraordinary effects.

**Table 4.5:** Normalized second coefficients  $A_2/A_0$  of the Legendre polynomial functions fitted to  $K_S^0$  angular distributions depending on the studied center-of-mass momentum range for the Pluto cocktail using the measured exclusive cross sections and angular distributions, for the tuned GiBUU-resonance model and for the experimental values determined in Section 3.2.3.

$p_{cm}$ [MeV/c]	Pluto	GiBUU-R <sub>tuned</sub>	EXP
0 – 160	$0.065 \pm 0.008$	$0.046 \pm 0.012$	$0.223 \pm 0.089$
160 – 320	$0.092 \pm 0.004$	$0.080 \pm 0.006$	$0.158 \pm 0.031$
320 – 480	$0.145 \pm 0.004$	$0.136 \pm 0.006$	$0.118 \pm 0.024$
480 – 640	$0.227 \pm 0.005$	$0.267 \pm 0.008$	$0.257 \pm 0.030$
640 – 800	$0.325 \pm 0.010$	$0.543 \pm 0.028$	$0.578 \pm 0.070$

Furthermore, it was possible to compare the experimental spectra to a modified GiBUU transport model [B<sup>+</sup>12] incorporating a pure resonance model. In the following the modification of the model will be explained and can be also found in [A<sup>+</sup>14c]. As already mentioned in Section 3.5.3, when comparing the inclusive data to GiBUU, the model uses cross section parameterizations from the resonance model of Tsushima *et al.* [TST99] if dealing with strangeness. However, for some exclusive channels an overestimation was observed, when confronting the model with measured cross sections [TST99]. And so the overshoot relative to the inclusive  $K_S^0$  spectra seen in the Figures 3.21 and 3.22 is well comprehensible. Therefore, the obvious modification that had to be applied was to adjust the parametrization such to fit not only the cross sections determined in this analysis but also experimental data measured at other energies. This was done by multiplying a scaling factor to the cross section parametrization of the corresponding channels. As seen in Table 4.6 especially the four-body reaction  $p + p \rightarrow \Lambda + p + \pi^+ + K^0$  had to be scaled down by a factor 0.42, which is solely produced via the reaction  $p + p \rightarrow \Lambda + \Delta^{++} + K^0$  in the model. In that sense, the model is rather close to the findings of this analysis. However, also other reactions found in the same Table were decreased. Moreover, enough energy is provided at the studied beam energy ( $E_{kin} = 3.5$  GeV) to open phase space for five-body reactions, which are not included in the resonance model. For example an excess energy of  $\varepsilon = 344$  MeV is found for the reaction  $p + p \rightarrow \Lambda + n + \pi^+ + \pi^+ + K^0$ . Further five-body final states are listed under multi-pion  $K^0$  reactions (C2) together with their excess energies in Table 4.2.

In order to consider them in the model the channels  $p+p \rightarrow \Lambda(1405)/\Sigma(1385)^0 + \Delta^{++} + K^0$  and  $p+p \rightarrow \Sigma(1385)^+ + \Delta^+ + K^0$  were added exploiting the decays of the  $\Lambda(1405)$  into  $\Sigma\pi$ - and of the  $\Sigma(1385)$  into  $\Lambda\pi$ - and  $\Sigma\pi$ -pairs. Since more final state particles are produced in these reactions, less energy is given to the  $K^0$ , which is reflected in a shift of the transverse momentum distribution to lower values. This modification is, therefore, needed to compensate the original GiBUU  $p_t$  distributions, which peak at higher momenta than the experimental ones (Fig. 3.21). The cross sections of these five-body channels found in Table 4.6 were chosen in such a way as to reproduce the low  $p_t$  regions of the inclusive  $K_S^0$  spectra. At the same time the cross sections were constrained such to not exceed the cross sections of the reactions  $p+p \rightarrow N + \Lambda(1405)/\Sigma(1385) + K$  as reported in [A<sup>+</sup>12b, A<sup>+</sup>12e, A<sup>+</sup>13], since a formation of more final states should be less probable.

**Table 4.6:** Cross sections at a beam energy of  $E_{kin} = 3.5$  GeV used in the GiBUU resonance model [B<sup>+</sup>12] based on [TST99]. Listed are original and tuned values together with the applied scaling factors in brackets. The last three reactions were added on top of the original model.

Reaction	GiBUU-R [ $\mu\text{b}$ ]	GiBUU-R <sub>tuned</sub> [ $\mu\text{b}$ ]
$p+p \rightarrow \Sigma^+ + p + K^0$	37.8	26.5 (0.70)
$p+p \rightarrow \Lambda + p + \pi^+ + K^0$	75.9	31.9 (0.42)
$p+p \rightarrow \Sigma^0 + p + \pi^+ + K^0$	24.6	17.7 (0.72)
$p+p \rightarrow \Sigma^+ + p + \pi^0 + K^0$	10.9	7.8 (0.72)
$p+p \rightarrow \Sigma^+ + n + \pi^+ + K^0$	5.5	3.9 (0.72)
$p+p \rightarrow \Lambda(1405) + \Delta^{++} + K^0$	n/a	5.3
$p+p \rightarrow \Sigma(1385)^0 + \Delta^{++} + K^0$	n/a	3.5
$p+p \rightarrow \Sigma(1385)^+ + \Delta^+ + K^0$	n/a	2.3

With these changes a comparison of the GiBUU model was performed to the experimental  $p_t$ - $y_{cm}$  (Fig. 4.19) and  $\cos\Theta_{cm}$ - $p_{cm}$  (Fig. 4.20) spectra of the inclusive  $K_S^0$  production as before on an absolute scale. A significant improvement of the comparison can be found in both representations with respect to the confrontation with the original model (Figs. 3.21 and 3.22). The yields almost coincide with the data in all transverse momentum distributions and also the maxima are in good agreement. This is confirmed in the angular distributions, which nicely agree in terms of yield. Only the highest center-of-mass momentum bin ( $p_{cm} = 640 - 800$  MeV/c) seems to be a little bit underestimated. However, no conclusion can be made here, since not the whole  $\cos\Theta_{cm}$  range was measured in this momentum bin. In terms of the strength of the angular anisotropy, no big difference was observed, as no changes were made regarding this aspect. Differences might have occurred only because of the modified relative cross sections of the reactions. Therefore, small fluctuations were measured in the normalized  $A_2$  coefficients (Table 4.5) from fitting the angular distributions with a Legendre polynomial function (Eq. 3.6) compared to the original values (Table 3.4). However, already the original model reproduced the experimental angular anisotropy in a satisfactory way, which can be deduced from the tuned model as well. The good agreement of the modified GiBUU model with the data allowed the usage of this tuned model for

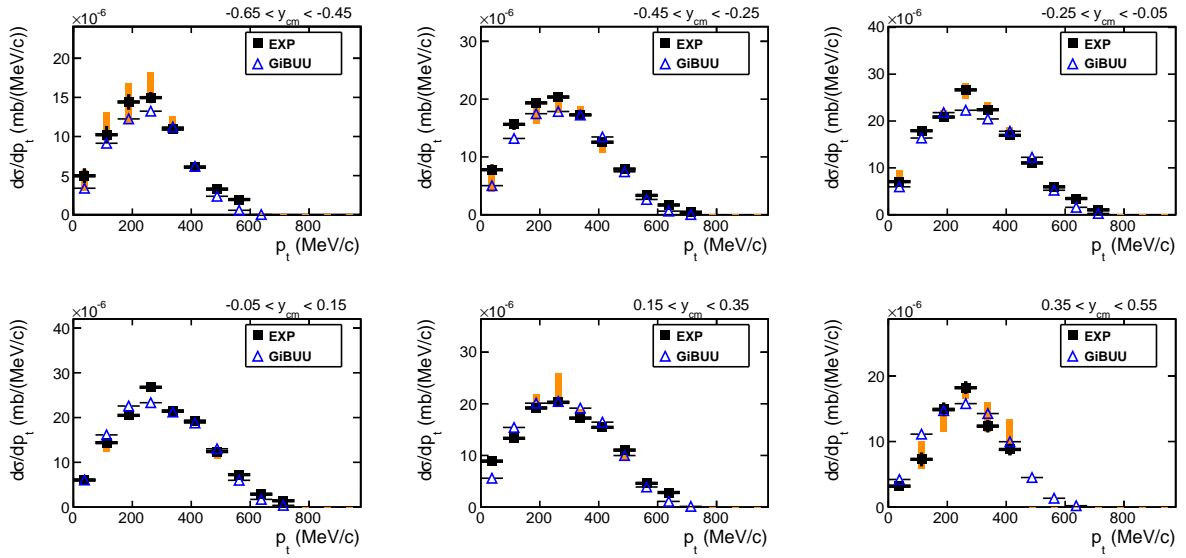


**Figure 4.19:** Comparison of the experimental  $K_S^0$   $p_t$ - $y_{cm}$  distributions (black squares) to the GiBUU transport model [B<sup>+</sup>12] based on the modified Tsushima resonance model [TST99] (blue open triangles) on an absolute scale. The experimental data includes statistical (black lines) and systematic uncertainties (orange bars).

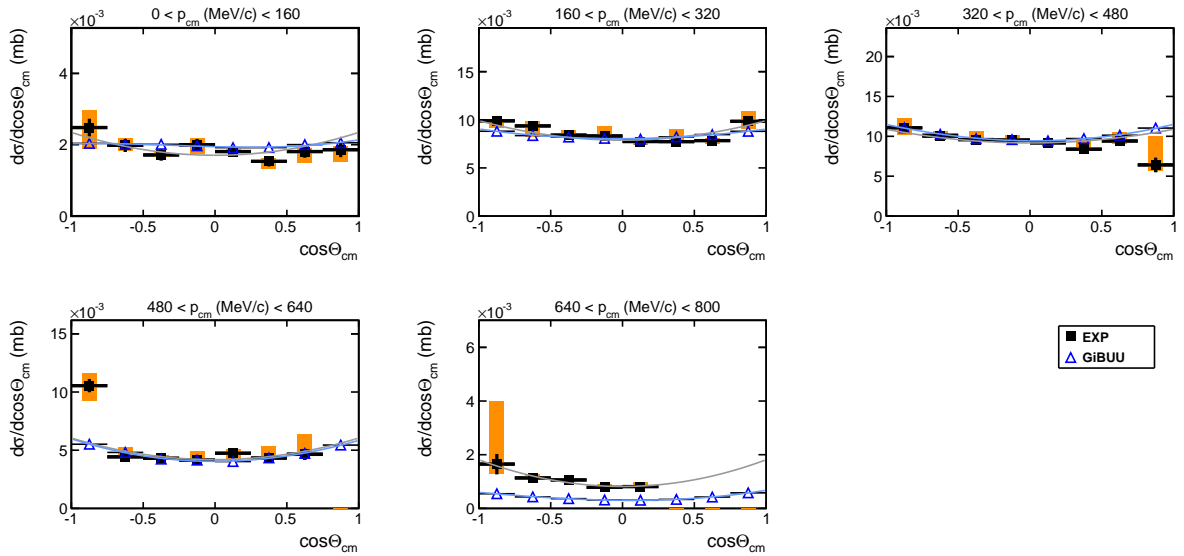


**Figure 4.20:** Comparison of the experimental  $K_S^0$  angular distributions (black squares) to the GiBUU transport model [B<sup>+</sup>12] based on the modified Tsushima resonance model [TST99] (blue open triangles) as a function of five center-of-mass momentum bins. Both data sets are absolute normalized and fitted with a Legendre polynomial function (Eq. 3.6). The experimental data includes statistical (black lines) and systematic uncertainties (orange bars).

more complicated reactions, namely p+Nb reactions, which have been measured at the same beam energy as the p+p data also with the HADES spectrometer. In a separate analysis of that data set it was possible to draw a conclusion on the repulsive kaon nucleon potential at normal nuclear density, which was found to be  $40 \pm 5$  MeV [A<sup>+</sup>14c]. Thereby, the GiBUU model was fixed by the p+p data as explained above, while other poorly constraint parameters like cross sections for  $p + n \rightarrow N + Y + K$  or  $\Delta + N \rightarrow K + X$  were systematically varied, to be able to pin down the desired information ( $KN$  potential) from the model.

## 4.4 Summary of the Exclusive $K_S^0$ Analysis

One of the motivations to study exclusive  $K_S^0$  channels in the p+p data sample collected at 3.5 GeV kinetic beam energy was given by the unsatisfactorily description of the kinematic distributions of the inclusive  $K_S^0$  production by transport models (Section 3.5), since this was required to extract information on the  $KN$  potential in the p+Nb data recorded at the same incident energy. The reason was found amongst others in the lack of exclusive experimental cross sections measured at the presented intermediate energy regime, in which the need of the inclusion of resonant reactions in the theoretical calculations had to be clarified. Therefore,  $K_S^0$  channels associated with resonant production ( $p + p \rightarrow K_S^0 + R + X$ ) were of particular interest and were studied in this work.

It was shown that by selecting events with exactly the four charged particles proton,  $\pi^+$ ,  $\pi^+$  and  $\pi^-$  the fraction of following reactions could be enhanced in the data sample for further investigations:

- $p + p \rightarrow \Lambda + \Delta^{++} + K^0$
- $p + p \rightarrow \Sigma^0 + \Delta^{++} + K^0$
- $p + p \rightarrow \Lambda + p + \pi^+ + K^0$
- $p + p \rightarrow \Sigma^0 + p + \pi^+ + K^0$
- $p + p \rightarrow \Sigma^+ + p + K^0$
- $p + p \rightarrow \Sigma(1385)^+ + p + K^0$

All  $K_S^0$  production channels, which were taken into account, are listed in Table 4.2. Several cuts on the primary and the secondary vertex of the  $K_S^0$  were applied on the data sample to reduce background contributions. However, a considerable amount of background originating from combinatorics of non-strange reactions remained and is reflected in the  $S/B$  ratio of 0.64 in the  $\pi^+\pi^-$ -invariant mass spectrum (Fig. 4.1). A procedure was found to describe this background with so-called sideband events, which is explained in Section 4.1.3. Five kinematical observables (three missing mass and two invariant mass distributions) illustrated in Figure 4.2 were defined to separate the listed reactions from each other. Indeed the obtained spectra confirmed the capability to distinguish reactions by the type of their hyperon content, which is of special interest, since the reaction  $p + p \rightarrow \Sigma^0 + \Delta^{++} + K^0$  has never been measured at any energy before. Furthermore, the goal to determine the contribution of the resonant  $\Delta(1232)^{++}$  reactions could be reached by including the  $p\pi^+$ -invariant mass spectra in the analysis, which allowed to differentiate

between a typical Breit-Wigner shape and a flat non-resonant phase space distribution. The relative contributions of the  $K_S^0$  channels, which were simulated by means of Monte Carlo with help of the Pluto event generator [F<sup>+</sup>07], and the background model were finally obtained by fitting them simultaneously to these five mass observables leading to the results shown in Section 4.2. Thereby, no interference was assumed to happen between the corresponding reactions. The extracted cross sections are quoted in Table 4.4 pointing out a predominant role of resonant production channels (6-10 times more than non-resonant) and rather large contributions from the  $\Sigma^+$  and the  $\Sigma(1385)^+$  reactions.

In the course of this analysis also the angular distribution of the  $p\pi^+$ -system was considered and studied with the assumption that the anisotropies included for the reactions  $p + p \rightarrow \Sigma^+ + p + K^0$  and  $p + p \rightarrow \Sigma(1385)^+ + p + K^0$  from previous measurements [AB<sup>+</sup>12, A<sup>+</sup>12b] are applicable for this analysis. The implementation of an angular anisotropy for the two  $\Delta^{++}$  channels was found to be necessary to reproduce the  $\cos\Theta_{cm}^{p\pi^+}$  spectra shown in Figure 4.3, let it be for  $\Lambda$ -preselected events or for  $\Sigma^0$ -preselected ones. The needed angular dependency could be determined (Sec. 4.1.5) and the corrected angular distributions are depicted in Figure 4.15, while the obtained values for the Legendre polynomial parameterizations can be found in Table 4.3. The angular anisotropies were found to be related to the hyperon type contained in the studied channel. Thus, a rather strong anisotropy was found to be necessary, if the  $\Delta^{++}$  reaction comes along with a  $\Lambda$ , whereas a  $\Sigma^0$  in the final state would lead to an almost flat emission of the  $\Delta^{++}$ . Similar findings were obtained by the COSY-TOF Collaboration [AB<sup>+</sup>10], which indicate very different production mechanisms of the corresponding channels to be the reason.

Last, but not least these exclusive results were implemented in terms of yield and anisotropy in a Monte Carlo cocktail of 14  $K^0$  channels and compared to experimental inclusive  $K_S^0$  spectra by means of  $p_t$ - $y_{cm}$  and  $\cos\Theta_{cm}$ - $p_{cm}$  (Figs. 4.17 and 4.18). A quite good description was found in both representations demonstrating the fact that no further processes are hidden in p+p collisions, but also approving the exclusive results obtained in this analysis. Furthermore, the exclusive yields could be used to adjust the resonance based GiBUU transport model [B<sup>+</sup>12, TST99], which under other modifications (see Sec. 4.3) fit nicely to the experimental spectra (Figs. 4.19 and 4.20). This allowed to fix the p+p interactions in the model for the systematic study of the  $KN$  potential in the p+Nb data set [A<sup>+</sup>14c], which was determined with a repulsive strength of  $40 \pm 5$  MeV.



# 5 Summary and Outlook

In today's understanding the standard model (SM) of particle physics is assumed to be the basic concept, with which our world can be explained. It did not only predict the fundamental ingredients (quarks and leptons) of which material is made of, but also delivered descriptions of the forces, that act in between them, and the gauge bosons, that mediate the forces. Although the model has not been proven wrong until now, not everything is well understood and thus require steady investigations. One of the hot topics is the study of strong interaction, which has been described in the framework of quantum chromodynamics (QCD). Due to this force quarks stick together within hadrons and nucleons are bound to each other within nuclei. The special feature of strong interaction is the property of gluons, which as mediators carry a combination of color–anti-color leading to color confinement and asymptotic freedom. Confinement plays a role at large distances equivalent to low-energy scales and is the reason, why quarks and gluons can never occur as free particles at normal conditions. The confined hadron phase as characterized in the QCD phase diagram is settled in this energy regime, in which the net baryon densities and the temperatures are relatively low. Experiments at the GSI Helmholtzzentrum für Schwerionenforschung in Darmstadt, Germany, which are supplied by the SIS18 synchrotron, are operating in this range, also the HADES setup [A<sup>+</sup>09], with which the data of this work has been recorded. The QCD phase diagram is actually the outcome of the nuclear equation of state (EOS), which links parameters such as temperature  $T$ , pressure  $p$  and baryon density  $\rho$  with each other ( $p(\rho, T)$ ). Furthermore, it connects many physics fields like astrophysics and nuclear physics and puts them into one global context. The form of the EOS is, however, not fixed and contains a lot of free parameters, that need to be determined little by little. Thereby, astrophysical observables as the mass and radius of neutron stars help to constrain the EOS as well as measurements of heavy ion reactions to probe different regimes of the QCD phase diagram. Hence, also rather high densities can be reached in heavy ion collisions ( $1 - 3\rho_0$  at SIS18) and provide indications of possible compositions of the neutron star interior ( $5 - 6\rho_0$ ). In terms of strangeness the idea of kaon condensation inside the neutron star, first brought up by Kaplan and Nelson [KN86, NK87], is of special interest. Such a condensate might appear, if the kaon chemical potential becomes equal to the electron and nucleon chemical potential, which is assumed to set in already at  $\approx 2 - 4\rho_0$ . Although such a scenario would considerably soften the EOS at least in the density region of heavy ion collisions, so that the heavy neutron star masses measured recently ( $>1.97 M_\odot$  [DPR<sup>+</sup>10, AFW<sup>+</sup>13]) could not be described anymore, some theoreticians still hang on the possibility of this idea [SB08, WCSB12, MCS13, GA12]. More information is, therefore, needed from experimental side to understand better in-medium effects and the resulting modifications of kaon interaction. The modification of kaon properties inside of a surrounding medium can be attributed to a restoration of the

spontaneously broken chiral symmetry as seen within the so-called chiral perturbation theory (ChPT) [BR91, RW00, Fuc06]. In this framework the effective degrees of freedom are not anymore the fermions, but the baryons and mesons. One can construct then the effective chiral kaon-nucleon Lagrangian, which includes the Weinberg-Tomozawa term. This term is responsible for the opposite behavior of kaons and anti-kaons in matter, since it either generates a repulsive  $KN$  or an attractive  $\bar{K}N$  potential leading to an in-/decrease of the respective kaon/anti-kaon mass with nuclear density. The strength of the potentials are not well measured especially for anti-kaons. For kaons ( $K^+$  and  $K^0$ ) several experiments studying for example momentum spectra [B<sup>+</sup>04, B<sup>+</sup>09, A<sup>+</sup>10] have agreed in a relatively slight repulsion, but disagree in the magnitude ( $U^{KN} = 20 - 40$  MeV). This situation requires not only a re-measurement of this observable, but also a validation of transport models, with which these results have been obtained.

The data used for this purpose are p+p reactions taken at a kinetic beam energy of 3.5 GeV. This data should on the one hand serve as a reference for measurements of more complex systems like p+A and heavy ion collisions, from which one could extract the  $KN$  potential, and on the other hand allow for a cross-check of widely-used transport models. An inclusive analysis was, therefore, performed to determine the  $K^0$  yield as a function of various kinematical observables (Chap. 3). One of the chosen double differential representations is the transverse momentum  $p_t$  spectrum in different center-of-mass rapidity  $y_{cm}$  ranges (Sec. 3.2.1), which is of particular interest for the study of the  $KN$  potential. If the  $K^0$  is produced within nuclear matter, it should feel the repulsive potential, that shifts the momentum spectrum to larger values and suppresses low momentum kaons as compared to kaons formed in p+p collisions. A further way to look at the  $K^0$  kinematics is the study of angular distributions as a function of the momentum within the pp-center-of-mass reference frame  $p_{cm}\text{-}\cos\Theta_{cm}$  (Sec. 3.2.3), that offers the possibility to quantify the production angles by means of a fit with a Legendre polynomial function. Thereby, the anisotropy was found to be momentum dependent showing a minimum at  $p_{cm} = 320 - 480$  MeV/c. Such representations in two kinematical independent observables allowed for a model independent acceptance and efficiency correction of the data (see Sec. 3.1.2), which was applied with help of a Monte Carlo cocktail of 13 channels producing  $K^0$  mesons in the final state. The composition of this simulation model is described in Section 2.4.2. To prove the applicability of a model independent correction, that also excuses the use of models, which do not completely reproduce reality, a self-consistency check was performed. As explained in Section 3.3, the acceptance and efficiency correction matrix obtained from the Monte Carlo cocktail was compared to the matrix, which was calculated from GiBUU simulations [B<sup>+</sup>12], and showed very good agreement as expected. Moreover, these corrected double differential spectra allowed to extract the integrated one-dimensional angular distribution  $dN/\cos\Theta_{cm}$ , from which a slight overall anisotropy was observed comparable to the  $K^0$  production at the lower beam energy of 2.26 GeV in the reaction  $p + p \rightarrow \Sigma^+ + p + K^0$  [AB<sup>+</sup>12]. In a similar way, it was possible to determine the rapidity density distribution  $dN/dy_{cm}$  from the  $p_t$ -spectra as described in Section 3.2.2. After an absolute normalization of the data (see Sec. 2.3.3), a total  $K^0$  cross section of  $113.5 \pm 2.7(stat)_{-10.2}^{+16.6(sys)} \mu b$  could be determined from this observable. Furthermore, both of these one-dimensional distributions reflect a symmetric production of the  $K^0$  mesons with respect to the pp-center-of-mass and thus

confirm the validity of the analysis procedure.

As mentioned above, these data were used for a cross-check of some widely-used transport calculations (HSD [CB99], UrQMD [B<sup>+</sup>98] and GiBUU [B<sup>+</sup>12]), which principles are explained in Section 1.6. The main difference between these theories is, however, the underlying model applied at the studied energy ( $\sqrt{s} = 3.18$  GeV). In this energy regime, HSD already uses the FRITIOF [AGP93] string fragmentation model for the description of particles, while UrQMD still relies on a resonance model. Since the GiBUU model is constructed quite flexible, it was possible to perform comparisons with the implemented resonance and PYTHIA [SMS06] string fragmentation models separately by adjusting the threshold energy for the transition accordingly. The double differential spectra introduced above were employed for the comparisons on absolute scales. However, none of the transport models could reproduce the  $K^0$  production kinematics satisfactorily. The angular anisotropy implemented in the models is too strong for all simulations except for the resonance based GiBUU model and the strength develops in a different way than in experiment. In fact, it increases with rising center-of-mass momenta. Furthermore, not even the  $K^0$  production cross sections could be reproduced by any model. The conclusion drawn from these results is that still quite some investigations have to be carried out from theory side also to reassure the results obtained from the measurements in terms of the  $KN$  potential in [B<sup>+</sup>04, B<sup>+</sup>09, A<sup>+</sup>10].

Nevertheless, these disagreements between experiment and transport calculations motivated a further analysis, with the aim to support theory with more experimental input. As described in Section 1.6, one of the main ingredients in transport models are experimental cross sections of elementary inelastic reactions. Therefore, exclusive measurements of  $K^0$  production channels can help to provide more reference points for eventual cross section parameterizations. The HADES energy regime is, furthermore, very interesting for transport models, since it is located in the transition region, in which the theories start to switch or have already switched from resonance to string fragmentation models. In this context, it is also important to extract possible contributions of resonances, which should be considered in the models. Since the reaction  $B + B \rightarrow B + Y + K$  (with  $B =$  baryon or baryon resonance and  $Y = \Lambda$  or  $\Sigma$  hyperon) is one of the main production channels for kaons, it is obvious that baryon resonances (e.g.  $N^*$  or  $\Delta^*$ ) might play a role in the initial as well as in the final states and influence kaon dynamics. This work has focused on the second case, namely on the resonance associated  $K^0$  production  $p + p \rightarrow K^0 + R + X$ . In particular, six reactions were selected by choosing events, which include exactly the four particles proton,  $\pi^+$ ,  $\pi^+$  and  $\pi^-$  within the detected and identified particles:

- $p + p \rightarrow \Lambda + \Delta^{++} + K^0$
- $p + p \rightarrow \Lambda + p + \pi^+ + K^0$
- $p + p \rightarrow \Sigma^+ + p + K^0$
- $p + p \rightarrow \Sigma^0 + \Delta^{++} + K^0$
- $p + p \rightarrow \Sigma^0 + p + \pi^+ + K^0$
- $p + p \rightarrow \Sigma(1385)^+ + p + K^0$

Here, the  $\Delta^{++}$  corresponds to the ordinary  $\Delta(1232)^{++}$ . However, further channels with a  $K_S^0$  in the final state remain in the selected data sample, which were also taken into account in this analysis. After various cuts, for example on the  $K_S^0$  mass observed in

the  $\pi^+\pi^-$ -invariant mass spectrum, a considerable background was left over, that mainly stems from combinatorics of non-strange reactions. This background could be successfully modeled by means of a  $K_S^0$  sideband sample. The method is explained in Section 4.1.3. To distinguish between the mentioned exclusive channels five kinematical observables (three missing mass and two invariant mass spectra) were considered, which were introduced in Section 4.1.2. For instance, they allowed to select on events with a  $\Lambda$  or a  $\Sigma^0$  in the final states and more importantly to differentiate between the resonant  $\Delta^{++}$  reactions and the non-resonant channels. In order to determine the relative contributions of the  $K^0$  channels, all of them were simulated by means of a Monte Carlo simulation and were fitted to the five kinematical distributions at once, whereby the background model was included in the fit as well. The results of the fit showing the incoherent sum of the fitted contributions compared to the experimental spectra are depicted in Section 4.2. A rather good agreement corresponding to a  $\chi^2/NDF$  of 2.57 was achieved in this procedure allowing to extract the total reaction cross sections for the listed  $K^0$  channels. A dominant role was found to be taken on by the resonant reactions. The  $\Delta^{++}$  channels inhibit a 6-10 times higher total yield as compared to their non-resonant equivalents. And also the reaction including a  $\Sigma(1385)^+$  resonance shows a rather large relative contribution, which is almost half of the amount of the reaction  $p + p \rightarrow \Sigma^+ + p + K^0$ . Here, one can already conclude that resonance models seem to be more suitable for the description of the HADES energy regime ( $\sqrt{s} < 3.18$  GeV).

Moreover, not only the exclusive cross sections could be extracted, but also information on angular distributions. As described in Section 4.1.5, the implementation of angular anisotropies in the production of the reactions  $p + p \rightarrow \Lambda/\Sigma^0 + \Delta^{++} + K^0$  were necessary to reproduce the angular distributions of the  $p\pi^+$ -system  $\cos\Theta_{cm}^{p\pi^+}$ . With help of an iterative procedure, it was possible to determine the strength of the needed anisotropies in dependency of the hyperon type formed in the final states. Quantitative numbers could be extracted by means of Legendre polynomial parameters, which show a rather strong anisotropy in the  $\Delta^{++}$  emission, if it is associated with a  $\Lambda$  hyperon. On the other hand, if it comes along with a  $\Sigma^0$  an almost flat distribution is observed. Similar findings were obtained in a study of the COSY-TOF Collaboration [AB<sup>+</sup>10] and were associated with the different production mechanisms of  $\Lambda K$ - and  $\Sigma K$ -pairs involving intermediate  $N^*$  and  $\Delta^*$  resonances.

Finally, it could be demonstrated that the inclusion of the exclusive results, which have been published in [A<sup>+</sup>14a], into simulations could considerably improve the description of the inclusive  $K_S^0$  data. Already by implementing the yields and the angular anisotropies into a simple incoherent Monte Carlo cocktail containing 14  $K^0$  production channels it was possible to reproduce the inclusive  $p_t$ - $y_{cm}$  and  $\cos\Theta_{cm}$ - $p_{cm}$  distributions of the  $K_S^0$  (Sec. 4.3). That means that actually no further processes seem to be needed to describe p+p reactions. Furthermore, it reassures the validity of the obtained exclusive results. As mentioned before, such exclusive cross sections can be used as an input for transport models. Indeed, this was done for the resonance based GiBUU model, which under some other modifications (see Sec. 4.3) was able to describe the same two-dimensional spectra to such a good extend that this improved model could be applied in another analysis to extract physics. Thereby, the contributions of the p+p interactions were fixed reducing some of the uncertain model parameters, while other parameters were systematically varied to determine the repulsive

---

$KN$  potential in the study of  $K_S^0$  in p+Nb collisions at the same kinetic beam energy [A+14c]. The strength of the  $KN$  potential was found to be  $40\pm 5$  MeV. This should be seen as a motivation to make use of the here obtained results also in other models and thus reduce the number of free or uncertain parameters. This is needed to receive more precise interpretations of p+A and heavy ion reactions, also for the upcoming experiments of HADES and CBM at the FAIR facility (Darmstadt, Germany), which will perform measurements at beam energies of 2-50 AGeV [F+11, FSS12].

In terms of studying kaon interaction and actually also anti-kaon interaction a further data set just recorded last year with the HADES setup will help in an improved understanding. The measurement of  $\pi^-+A$  reactions (for  $A = {}^{12}\text{C}$  or  ${}^{74}\text{W}$ ) at a beam momentum of  $p_{beam} = 1.7$  GeV/c benefit from an installed diamond start detector for time-of-flight measurements, from a pion-tracker, with which one can determine the momentum of the incoming secondary pion beam, and from high resolution RPCs (**R**esistive **P**late **C**hambers), which even allow for the identification of  $K^+$  and  $K^-$  mesons. The results will complement the pion-induced measurements carried out by the FOPI Collaboration [B+09] and deliver further inputs for theoretical models. Furthermore, it offers another possibility to obtain the strength of the  $KN$  potential at an energy range, in which all transport models agree in using an underlying hadron/resonance model.



# A Appendix to the Particle Identification

## A.1 Energy Loss in TOF and TOFino

Additionally to the energy loss ( $dE/dx$ ) information of the MDCs (Multi-Wire Drift Chambers) further detectors deliver information on the same quantity. The energy of a particle track lost in the TOF is depicted in Figure A.1, panel (a), as a function of the polarity times momentum. Although the  $dE/dx$  resolution is in principle good enough to distinguish  $\pi^+$  mesons from protons up to a momentum of about 1000 MeV/c, protons with momenta lower than 400 MeV/c are stopped in the detector and leave a signature of a linear correlation in the energy loss distribution. As a consequence, pions are contaminated with protons at low momenta and therefore cannot be identified unambiguously anymore. This is the reason, why the TOF  $dE/dx$  information was not used in this work.

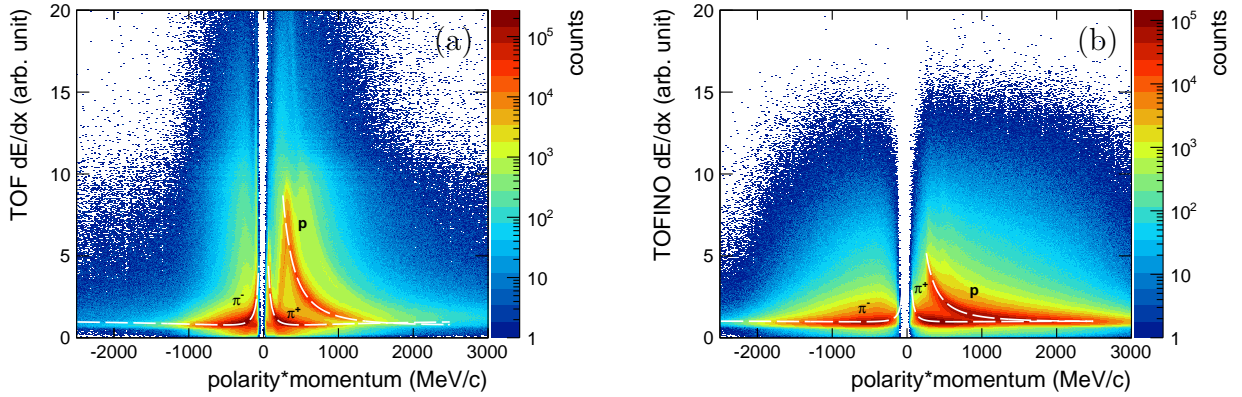


**Figure A.1:** Experimental energy loss  $dE/dx$  in the TOF (panel (a)) and in the TOFino (panel (b)) detectors as a function of the momentum times charge of the track. The white dashed lines indicate the specific energy loss functions according to Bethe-Bloch (Eq. 2.1).

Also from the TOFino detector it is possible to extract the energy loss information, which is shown in panel (b) of the same figure again as function of polarity times momentum of the particle track. However, the  $dE/dx$  resolution is much worse than the one determined from the MDCs allowing a separation of  $\pi^+$  mesons from protons only below 500 MeV/c. Thus, no improvement of the particle identification can be expected by including this observable and so it was also disregarded.

## A.2 Energy Loss in MDC with Pion Preselection in TOF

To study the purity of the particle identification as described in Section 2.2 a rather pure sample of pions needed to be preselected. Such a sample was retrieved by a narrow graphical cut on the  $dE/dx$  distribution of the TOF detector (Fig. A.1, panel (a)). The MDC energy loss distribution of these pions are illustrated in Figure A.2, in which a sharp cut-off at 1200 MeV/c is seen due to the applied cut in the TOF  $dE/dx$ . Since no other structure than the one of the pions appear, which could be for example induced by the stopped protons in the TOF, it was assumed that the pion sample is pure enough for the intended purity study.

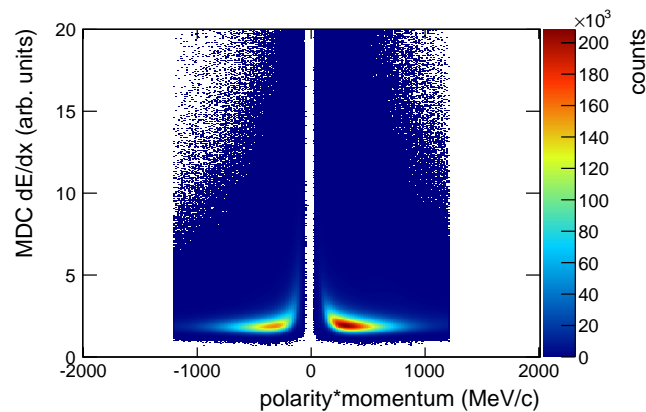


**Figure A.2:** Experimental energy loss  $dE/dx$  in the MDCs as a function of the momentum times charge of the track with a pion preselection with help of the TOF  $dE/dx$  information.

# Bibliography

- [A+05] M. Agnello et al.  
Evidence for a kaon-bound state  $K^-pp$  produced in  $K^-$  absorption reactions at rest.  
*Phys. Rev. Lett.*, 94:212303, 2005.  
(Cited on page 11)
- [A+08] G. Agakishiev et al.  
Study of dielectron production in C+C collisions at 1 A GeV.  
*Phys. Lett.*, B663:43–48, 2008.  
(Cited on page 21)
- [A+09] G. Agakishiev et al.  
The High-Acceptance Dielectron Spectrometer HADES.  
*Eur. Phys. J.*, A41:243–277, 2009.  
(Cited on pages i, ii, 21, 22, 24, and 101)
- [A+10] G. Agakishiev et al.  
In-Medium Effects on  $K^0$  Mesons in Relativistic Heavy-Ion Collisions.  
*Phys. Rev.*, C82:044907, 2010.  
(Cited on pages i, ii, 12, 22, 67, 102, and 103)
- [A+11] G. Agakishiev et al.  
Dielectron production in Ar+KCl collisions at 1.76 A GeV.  
*Phys. Rev.*, C84:014902, 2011.  
(Cited on page 21)
- [A+12a] Georges Aad et al.  
Observation of a new particle in the search for the Standard Model Higgs boson with the ATLAS detector at the LHC.  
*Phys. Lett.*, B716:1–29, 2012.  
(Cited on page 6)
- [A+12b] G. Agakishiev et al.  
Baryonic resonances close to the  $\bar{K}$ -N threshold: The Case of  $\Sigma(1385)^+$  in pp collisions.  
*Phys. Rev.*, C85:035203, 2012.  
(Cited on pages 10, 14, 22, 69, 82, 83, 88, 96, and 99)
- [A+12c] G. Agakishiev et al.  
First measurement of low momentum dielectrons radiated off cold nuclear matter.  
*Phys. Lett.*, B715:304–309, 2012.  
(Cited on page 21)

- [A<sup>+</sup>12d] G. Agakishiev et al.  
Inclusive dielectron spectra in p+p collisions at 3.5 GeV.  
*Eur. Phys. J.*, A48:64, 2012.  
(Cited on page 21)
- [A<sup>+</sup>12e] G. Agakishiev et al.  
Production of  $\Sigma^\pm\pi^\mp pK^+$  in p+p reactions at 3.5 GeV beam energy.  
*Nucl. Phys.*, A881:178–186, 2012.  
(Cited on pages 15 and 96)
- [A<sup>+</sup>13] G. Agakishiev et al.  
Baryonic resonances close to the  $\bar{K}$ -N threshold: the case of  $\Lambda(1405)$  in pp collisions.  
*Phys. Rev.*, C87:025201, 2013.  
(Cited on pages 10, 22, and 96)
- [A<sup>+</sup>14a] G. Agakishiev et al.  
Associate  $K^0$  production in p+p collisions at 3.5 GeV: The role of  $\Delta(1232)^{++}$ .  
*Phys. Rev.*, C90:015202, 2014.  
(Cited on pages 92 and 104)
- [A<sup>+</sup>14b] G. Agakishiev et al.  
Lambda hyperon production and polarization in collisions of p(3.5 GeV)+Nb.  
*Eur. Phys. J.*, A50:81, 2014.  
(Cited on page 22)
- [A<sup>+</sup>14c] G. Agakishiev et al.  
Medium effects in proton-induced  $K^0$  production at 3.5 GeV.  
*Phys. Rev.*, C90:054906, 2014.  
(Cited on pages i, ii, 95, 98, 99, and 105)
- [A<sup>+</sup>15] G. Agakishiev et al.  
Partial Wave Analysis of the Reaction  $p(3.5\text{GeV}) + p \rightarrow pK^+\Lambda$  to Search for the " $ppK^-$ " Bound State.  
*Phys. Lett.*, B742:242–248, 2015.  
(Cited on pages 11, 14, 22, 69, and 82)
- [AB<sup>+</sup>10] M. Abdel-Bary et al.  
Production of  $\Lambda$  and  $\Sigma^0$  hyperons in proton-proton collisions.  
*Eur. Phys. J.*, A46:27–44, 2010.  
(Cited on pages 14, 89, 99, and 104)
- [AB<sup>+</sup>12] M. Abdel-Bary et al.  
The  $pK^0\Sigma^+$  final state in proton-proton collisions.  
*Eur. Phys. J.*, A48:23, 2012.  
(Cited on pages 38, 39, 40, 55, 58, 69, 82, 83, 88, 92, 99, and 102)
- [ABB<sup>+</sup>14] G. Agakishiev, A. Balanda, D. Belver, A. Belyaev, J.C. Berger-Chen, et al.  
Baryon resonance production and dielectron decays in proton-proton collisions at 3.5 GeV.  
*Eur. Phys. J.*, A50:82, 2014.  
(Cited on page 21)
- [AEF<sup>+</sup>06] Y. Aoki, G. Endrodi, Z. Fodor, S.D. Katz, and K.K. Szabo.  
The Order of the quantum chromodynamics transition predicted by the standard

- model of particle physics.  
*Nature*, 443:675–678, 2006.  
(Cited on page 4)
- [AFW<sup>+</sup>13] John Antoniadis, Paulo C.C. Freire, Norbert Wex, Thomas M. Tauris, Ryan S. Lynch, et al.  
A Massive Pulsar in a Compact Relativistic Binary.  
*Science*, 340:6131, 2013.  
(Cited on pages 5 and 101)
- [AGP93] Bo Andersson, G. Gustafson, and Hong Pi.  
The FRITIOF model for very high-energy hadronic collisions.  
*Z. Phys.*, C57:485–494, 1993.  
(Cited on pages 16, 60, and 103)
- [AP<sup>+</sup>04] H. Alvarez-Pol et al.  
A large area timing RPC prototype for ion collisions in the HADES spectrometer.  
*Nucl. Instrum. Meth.*, A535:277–282, 2004.  
(Cited on page 25)
- [AY02] Yoshinori Akaishi and Toshimitsu Yamazaki.  
Nuclear  $\bar{K}$  bound states in light nuclei.  
*Phys. Rev.*, C65:044005, 2002.  
(Cited on page 11)
- [B<sup>+</sup>97] D. Best et al.  
 $K^+$  production in the reaction  $^{58}\text{Ni}+^{58}\text{Ni}$  at incident energies from 1 to 2 AGeV.  
*Nucl. Phys.*, A625:307–324, 1997.  
(Cited on page 12)
- [B<sup>+</sup>98] S.A. Bass et al.  
Microscopic models for ultrarelativistic heavy ion collisions.  
*Prog. Part. Nucl. Phys.*, 41:255–369, 1998.  
(Cited on pages i, ii, 16, 18, 43, 60, 62, 63, 67, 69, and 103)
- [B<sup>+</sup>04] Markus Buescher et al.  
Inclusive  $K^+$  meson production in proton nucleus interactions.  
*Eur. Phys. J.*, A22:301–317, 2004.  
(Cited on pages i, ii, 13, 67, 102, and 103)
- [B<sup>+</sup>05] G. Beer et al.  
Measurement of the kaonic hydrogen X-ray spectrum.  
*Phys. Rev. Lett.*, 94:212302, 2005.  
(Cited on page 10)
- [B<sup>+</sup>09] M.L. Benabderrahmane et al.  
Measurement of the in-medium  $K^0$  inclusive cross section in  $\pi^-$ -induced reactions at 1.15 GeV/c.  
*Phys. Rev. Lett.*, 102:182501, 2009.  
(Cited on pages i, ii, 13, 60, 67, 102, 103, and 105)
- [B<sup>+</sup>11] M. Bazzi et al.  
First measurement of kaonic helium-3 X-rays.  
*Phys. Lett.*, B697:199–202, 2011.  
(Cited on page 10)

- [B<sup>+</sup>12] O. Buss et al.  
 Transport-theoretical Description of Nuclear Reactions.  
*Phys. Rept.*, 512:1–124, 2012.  
 (Cited on pages i, ii, 16, 43, 57, 60, 62, 65, 66, 67, 69, 95, 96, 97, 99, 102, and 103)
- [BBB<sup>+</sup>11] M. Bazzi, G. Beer, L. Bombelli, A.M. Bragadireanu, M. Cargnelli, et al.  
 A New Measurement of Kaonic Hydrogen X rays.  
*Phys. Lett.*, B704:113–117, 2011.  
 (Cited on page 10)
- [BCC11] Pedro Bicudo, Nuno Cardoso, and Marco Cardoso.  
 The Chiral crossover, static-light and light-light meson spectra, and the deconfinement crossover.  
*PoS*, BORMIO2011:062, 2011.  
 (Cited on page 3)
- [BCN66] E. Bierman, A.P. Colleraine, and U. Nauenberg.  
 Search for Dibaryon Resonant States.  
*Phys. Rev.*, 147:922–931, 1966.  
 (Cited on page 14)
- [BDG88] G.F. Bertsch and S. Das Gupta.  
 A Guide to microscopic models for intermediate-energy heavy ion collisions.  
*Phys. Rept.*, 160:189–233, 1988.  
 (Cited on pages 17 and 18)
- [BEF<sup>+</sup>14] N. Brambilla, S. Eidelman, P. Foka, S. Gardner, A.S. Kronfeld, et al.  
 QCD and Strongly Coupled Gauge Theories: Challenges and Perspectives.  
*Eur. Phys. J.*, C74(10):2981, 2014.  
 (Cited on pages 11 and 12)
- [Bet30] H. Bethe.  
 Theory of the passage of fast corpuscular rays through matter.  
*Annalen Phys.*, 5:325–400, 1930.  
 (Cited on page 27)
- [BFG<sup>+</sup>13] A. Blanco, P. Fonte, J.A. Garzon, W. Koenig, G. Kornakov, et al.  
 Performance of the HADES-TOF RPC wall in a Au + Au beam at 1.25 AGeV.  
*JINST*, 8:P01004, 2013.  
 (Cited on page 25)
- [Bir96] Michael C. Birse.  
 What does a change in the quark condensate say about restoration of chiral symmetry in matter?  
*Phys. Rev.*, C53:2048–2051, 1996.  
 (Cited on page 8)
- [Bor05] B. Borasoy.  
 SU(3) chiral effective field theories: A Status report.  
*Nucl. Phys.*, A754:191–201, 2005.  
 (Cited on page 7)
- [BR91] G.E. Brown and Mannque Rho.  
 Scaling effective Lagrangians in a dense medium.  
*Phys. Rev. Lett.*, 66:2720–2723, 1991.

- (Cited on pages 8 and 102)
- [BZS<sup>+</sup>99] M. Bleicher, E. Zabrodin, C. Spieles, S.A. Bass, C. Ernst, et al.  
Relativistic hadron hadron collisions in the ultrarelativistic quantum molecular dynamics model.  
*J. Phys.*, G25:1859–1896, 1999.
- (Cited on pages 16 and 17)
- [C<sup>+</sup>12] Serguei Chatrchyan et al.  
Observation of a new boson at a mass of 125 GeV with the CMS experiment at the LHC.  
*Phys. Lett.*, B716:30–61, 2012.
- (Cited on page 6)
- [CB99] W. Cassing and E.L. Bratkovskaya.  
Hadronic and electromagnetic probes of hot and dense nuclear matter.  
*Phys. Rept.*, 308:65–233, 1999.
- (Cited on pages i, ii, 16, 43, 60, 61, 67, 69, and 103)
- [CBM<sup>+</sup>97] W. Cassing, E.L. Bratkovskaya, U. Mosel, S. Teis, and A. Sibirtsev.  
Kaon versus anti-kaon production at SIS energies.  
*Nucl. Phys.*, A614:415–432, 1997.
- (Cited on page 17)
- [CER95] CERN.  
Detector Description and Simulation Tool - Geant3, 1995.  
[http://wwwasdoc.web.cern.ch/wwwasdoc/geant\\_html3/geantall.html](http://wwwasdoc.web.cern.ch/wwwasdoc/geant_html3/geantall.html);  
accessed on 12-December-2014.
- (Cited on page 36)
- [Dah08] Torsten Dahms.  
Dilepton spectra in p+p and Au+Au collisions at RHIC.  
*arXiv*, nucl-ex/0810.3040, 2008.
- (Cited on page 7)
- [Dan01] Pawel Danielewicz.  
Nuclear equation of state.  
*arXiv*, nucl-th/0112006:24–42, 2001.
- (Cited on page 4)
- [Daw94] S. Dawson.  
Introduction to the physics of Higgs bosons.  
*arXiv*, hep-ph/9411325, 1994.
- (Cited on page 6)
- [DHW08] Akinobu Dote, Tetsuo Hyodo, and Wolfram Weise.  
 $K^-pp$  system with chiral SU(3) effective interaction.  
*Nucl. Phys.*, A804:197–206, 2008.
- (Cited on page 11)
- [DHW09] Akinobu Dote, Tetsuo Hyodo, and Wolfram Weise.  
Variational calculation of the  $ppK^-$  system based on chiral SU(3) dynamics.  
*Phys. Rev.*, C79:014003, 2009.
- (Cited on page 11)
- [DMR09] A. Datta, B. Mukhopadhyaya, and A. Raychaudhuri.

- Physics at the Large Hadron Collider.*  
Springer, 2009.  
(Cited on page 5)
- [DPR<sup>+</sup>10] Paul Demorest, Tim Pennucci, Scott Ransom, Mallory Roberts, and Jason Hessels.  
Shapiro Delay Measurement of A Two Solar Mass Neutron Star.  
*Nature*, 467:1081–1083, 2010.  
(Cited on pages 5 and 101)
- [EC96] W. Ehehalt and W. Cassing.  
Relativistic transport approach for nucleus nucleus collisions from SIS to SPS energies.  
*Nucl. Phys.*, A602:449–486, 1996.  
(Cited on page 16)
- [EF12] E. Epple and L. Fabbietti.  
Determination of the  $\Sigma(\mathbf{1385})^0/\Lambda(\mathbf{1405})$  ratio in p+p collisions at 3.5 GeV.  
*Hyperfine Interact.*, 210:45–51, 2012.  
(Cited on page 26)
- [EKP95] Paul J. Ellis, Roland Knorren, and Madappa Prakash.  
Kaon condensation in neutron star matter with hyperons.  
*Phys. Lett.*, B349:11–17, 1995.  
(Cited on page 5)
- [Epp14] Eliane Epple.  
*Measurable Consequences of an Attractive anti-KN Interaction.*  
Dissertation, Technische Universität München, München, 2014.  
(Cited on pages 69 and 82)
- [F<sup>+</sup>07] I. Fröhlich et al.  
Pluto: A Monte Carlo Simulation Tool for Hadronic Physics.  
*PoS*, ACAT2007:076, 2007.  
(Cited on pages 35, 78, and 99)
- [F<sup>+</sup>11] Bengt Friman et al.  
The CBM physics book: Compressed baryonic matter in laboratory experiments.  
*Lect. Notes Phys.*, 814:1–980, 2011.  
(Cited on pages i, ii, 8, and 105)
- [F<sup>+</sup>13] L. Fabbietti et al.  
 $pK^+\Lambda$  final state: Towards the extraction of the  $ppK^-$  contribution.  
*Nucl. Phys.*, A914:60–68, 2013.  
(Cited on pages 14, 22, and 69)
- [FAG<sup>+</sup>68] M. Firebaugh, G. Ascoli, E.L. Goldwasser, R.D. Sard, and J. Wray.  
Strange-particle production in 8 BeV/c proton-proton interactions.  
*Phys. Rev.*, 172:1354–1369, 1968.  
(Cited on page 14)
- [FGH<sup>+</sup>10] I. Fröhlich, T. Galatyuk, R. Holzmann, J. Markert, B. Ramstein, et al.  
Design of the Pluto Event Generator.  
*J. Phys. Conf. Ser.*, 219:032039, 2010.  
(Cited on page 35)

- [FH11] Kenji Fukushima and Tetsuo Hatsuda.  
The phase diagram of dense QCD.  
*Rept. Prog. Phys.*, 74:014001, 2011.  
(Cited on page 4)
- [FSS12] Vladimir E. Fortov, Boris Yu. Sharkov, and H. Stoker.  
European facility for antiproton and ion research (FAIR): The new international center for fundamental physics and its research program.  
*Phys. Usp.*, 55:582–602, 2012.  
(Cited on pages i, ii, and 105)
- [FUB<sup>+</sup>07] A. Forster, F. Uhlig, I. Bottcher, D. Brill, M. Debowski, et al.  
Production of  $K^+$  and of  $K^-$  Mesons in Heavy-Ion Collisions from 0.6 to 2.0 A GeV Incident Energy.  
*Phys. Rev.*, C75:024906, 2007.  
(Cited on pages 10 and 12)
- [Fuc06] Christian Fuchs.  
Kaon production in heavy ion reactions at intermediate energies.  
*Prog. Part. Nucl. Phys.*, 56:1–103, 2006.  
(Cited on pages 4, 8, 9, 10, 12, 14, and 102)
- [GA12] Neha Gupta and P. Arumugam.  
Role of higher order couplings in the presence of kaons in relativistic mean field description of neutron stars.  
*Phys. Rev.*, C85:015804, 2012.  
(Cited on pages 6 and 101)
- [Gal14] Tetyana Galatyuk.  
HADES overview.  
*Nucl. Phys.*, A931:41–51, 2014.  
(Cited on pages 4 and 21)
- [GCG98] J. Geiss, W. Cassing, and C. Greiner.  
Strangeness production in the hsd transport approach from SIS to SPS energies.  
*Nucl. Phys.*, A644:107–138, 1998.  
(Cited on pages 16 and 17)
- [GMOR68] Murray Gell-Mann, R.J. Oakes, and B. Renner.  
Behavior of current divergences under  $SU(3) \times SU(3)$ .  
*Phys. Rev.*, 175:2195–2199, 1968.  
(Cited on page 7)
- [HAD12] HADES.  
The HADES simulation package HGeant, 2012.  
<https://hades-wiki.gsi.de/cgi-bin/view/SimAna/HadesGeant>; accessed on 12-December-2014.  
(Cited on page 36)
- [HOL<sup>+</sup>12] Christoph Hartnack, Helmut Oeschler, Yvonne Leifels, Elena L. Bratkovskaya, and Jörg Aichelin.  
Strangeness Production close to Threshold in Proton-Nucleus and Heavy-Ion Collisions.  
*Phys. Rept.*, 510:119–200, 2012.

- (Cited on pages 8, 9, 14, and 15)
- [IHI+97] M. Iwasaki, R.S. Hayano, T.M. Ito, S.N. Nakamura, T.P. Terada, et al.  
Observation of Kaonic Hydrogen  $K_{\alpha}$  X Rays.  
*Phys. Rev. Lett.*, 78:3067–3069, 1997.
- (Cited on page 10)
- [IHN+98] T.M. Ito, R.S. Hayano, S.N. Nakamura, T.P. Terada, M. Iwasaki, et al.  
Observation of kaonic hydrogen atom x rays.  
*Phys. Rev.*, C58:2366–2382, 1998.
- (Cited on pages 10 and 11)
- [isg14] isgwt.  
Go on a particle quest at the first cern hackfest, 2014.  
<http://www.isgtw.org/spotlight/go-particle-quest-first-cern-hackfest>;  
accessed on 14-October-2014.
- (Cited on page 1)
- [K+70] S. Klein et al.  
Four-body strange-particle production in p p collisions at 6 BeV/c.  
*Phys. Rev.*, D1:3019–3030, 1970.
- (Cited on page 15)
- [K+11] A.K. Kurilkin et al.  
Single and double pion production in np collisions at 1.25 GeV with HADES.  
*arXiv*, nucl-ex/1102.1843, 2011.
- (Cited on page 26)
- [KK99] S. Kubis and M. Kutschera.  
Kaon condensation in neutron stars and high density behavior of nuclear  
symmetry energy.  
*Acta Phys. Polon.*, B30:2747–2758, 1999.
- (Cited on page 5)
- [KLW90] S. Kliment, Matthias F.M. Lutz, and W. Weise.  
Chiral phase transition in the SU(3) Nambu and Jona-Lasinio model.  
*Phys. Lett.*, B249:386–390, 1990.
- (Cited on pages 7 and 8)
- [KN86] D.B. Kaplan and A.E. Nelson.  
Strange Goings on in Dense Nucleonic Matter.  
*Phys. Lett.*, B175:57–63, 1986.
- (Cited on pages 5, 8, 9, and 101)
- [Koc95] Volker Koch.  
Introduction to chiral symmetry.  
*arXiv*, nucl-th/9512029, 1995.
- (Cited on page 7)
- [Kum13] Lokesh Kumar.  
Review of Recent Results from the RHIC Beam Energy Scan.  
*Mod. Phys. Lett.*, A28:1330033, 2013.
- (Cited on page 4)
- [L+09] K. Lapidus et al.  
Dielectron production in pp and dp collisions at 1.25 GeV/u with HADES.

- arXiv*, nucl-ex/0904.1128, 2009.  
(Cited on pages 21 and 26)
- [Lei13] Yvonne Leifels.  
Strangeness production in heavy ion collisions: Constraining the KN-potential in medium.  
*J. Phys. Conf. Ser.*, 420:012019, 2013.  
(Cited on page 4)
- [LLB97] Guo-Qiang Li, C.H. Lee, and G.E. Brown.  
Kaons in dense matter, kaon production in heavy ion collisions, and kaon condensation in neutron stars.  
*Nucl. Phys.*, A625:372–434, 1997.  
(Cited on pages 5, 8, and 9)
- [M<sup>+</sup>00] M. Menzel et al.  
First measurement of anti-kaon phase space distributions in nucleus - nucleus collisions at subthreshold beam energies.  
*Phys. Lett.*, B495:26–32, 2000.  
(Cited on page 12)
- [MCS13] Tsuyoshi Miyatsu, Myung-Ki Cheoun, and Koichi Saito.  
Equation of state for neutron stars in SU(3) flavor symmetry.  
*Phys. Rev.*, C88(1):015802, 2013.  
(Cited on pages 6 and 101)
- [Mis13] André Mischke.  
Studying hot QCD matter at the CERN-LHC with heavy quarks.  
*PoS*, DIS2013:199, 2013.  
(Cited on page 5)
- [MS86] T. Matsui and H. Satz.  
 $J/\psi$  Suppression by Quark-Gluon Plasma Formation.  
*Phys. Lett.*, B178:416, 1986.  
(Cited on page 5)
- [MS88] O. Madelung and H. Schopper.  
*Landolt-Börnstein: Numerical data and functional relationships in science and technology. New series, Gr. 1, Nuclear and particle physics, Vol. 12b, Total cross-sections for reactions of high energy particles.*  
Springer, 1988.  
(Cited on pages 38, 39, 69, and 92)
- [MS92] D. M. Manley and E. M. Saleski.  
Multichannel resonance parametrization of  $\pi N$  scattering amplitudes.  
*Phys. Rev. D*, 45:4002–4033, Jun 1992.  
(Cited on page 64)
- [Mün14] Robert Helmut Münzer.  
*Search for the kaonic bound state  $ppK^-$ .*  
Dissertation, Technische Universität München, München, 2014.  
(Cited on page 11)
- [N<sup>+</sup>07] M. Nikipelov et al.  
Investigation of the reaction  $pp \rightarrow pK^0\pi^+\Lambda$  in search of the pentaquark.

- J. Phys.*, G34:627, 2007.  
(Cited on pages 15, 38, 39, 69, and 92)
- [Nam09] Yoichiro Nambu.  
Nobel Lecture: Spontaneous symmetry breaking in particle physics: A case of cross fertilization.  
*Int. J. Mod. Phys.*, A24:2371–2377, 2009.  
(Cited on page 7)
- [NK87] Ann E. Nelson and David B. Kaplan.  
Strange Condensate Realignment in Relativistic Heavy Ion Collisions.  
*Phys. Lett.*, B192:193, 1987.  
(Cited on pages 5, 8, 9, and 101)
- [O<sup>+</sup>14] K.A. Olive et al.  
Review of Particle Physics.  
*Chin. Phys.*, C38:090001, 2014.  
(Cited on pages 6, 14, 75, and 80)
- [O’B13] Edward O’Brien.  
Recent PHENIX results from the RHIC energy scan.  
*Nucl. Phys.*, A904-905:264c–269c, 2013.  
(Cited on page 4)
- [RBW05] Th. Roth, M. Buballa, and J. Wambach.  
Medium modifications of antikaons in dense matter.  
*arXiv*, nucl-th/0504056, 2005.  
(Cited on page 11)
- [Rus10] Anar Rustamov.  
Inclusive meson production in 3.5 GeV p p collisions studied with the HADES spectrometer.  
*AIP Conf. Proc.*, 1257:736–740, 2010.  
(Cited on pages 34, 81, 90, and 91)
- [RW00] R. Rapp and J. Wambach.  
Chiral symmetry restoration and dileptons in relativistic heavy ion collisions.  
*Adv. Nucl. Phys.*, 25:1, 2000.  
(Cited on pages 7, 8, and 102)
- [S<sup>+</sup>01] Christian Thomas Sturm et al.  
Evidence for a soft nuclear equation of state from kaon production in heavy ion collisions.  
*Phys. Rev. Lett.*, 86:39–42, 2001.  
(Cited on page 4)
- [Sah14] Nihar Ranjan Sahoo.  
Recent results on event-by-event fluctuations from the RHIC Beam Energy Scan program in the STAR experiment.  
*J. Phys. Conf. Ser.*, 535:012007, 2014.  
(Cited on page 4)
- [SB08] Jürgen Schaffner-Bielich.  
Hypernuclear Physics for Neutron Stars.  
*Nucl. Phys.*, A804:309–321, 2008.

- (Cited on pages 5, 6, and 101)
- [SBM97] Jürgen Schaffner, Jakob Bondorf, and Igor N. Mishustin.  
In-medium production of kaons at the mean field level.  
*Nucl. Phys.*, A625:325–346, 1997.  
(Cited on pages 9, 10, 11, and 12)
- [SC98] A. Sibirtsev and W. Cassing.  
Strangeness production in proton proton collisions.  
*arXiv*, nucl-th/9802019, 1998.  
(Cited on pages 37, 38, 80, 81, and 91)
- [Sch03] Stefan Scherer.  
Introduction to chiral perturbation theory.  
*Adv. Nucl. Phys.*, 27:277, 2003.  
(Cited on pages 3 and 7)
- [Sch13] Alexander Schmah.  
Recent results from RHIC.  
*PoS*, Bormio2013:072, 2013.  
(Cited on page 4)
- [Sco13] Enrico Scomparin.  
ALICE results on quarkonia.  
*Nucl. Phys.*, A904-905:202c–209c, 2013.  
(Cited on page 5)
- [Shu14] Prashant Shukla.  
Overview of quarkonia and heavy flavour measurements by CMS.  
*arXiv*, nucl-ex/1405.3810, 2014.  
(Cited on page 5)
- [SMS06] Torbjorn Sjostrand, Stephen Mrenna, and Peter Z. Skands.  
PYTHIA 6.4 Physics and Manual.  
*JHEP*, 0605:026, 2006.  
(Cited on pages 16, 60, and 103)
- [Spo13] Martin Spousta.  
Jet Quenching at LHC.  
*Mod. Phys. Lett.*, A28:1330017, 2013.  
(Cited on page 5)
- [T<sup>+</sup>14] A.O. Tokiyasu et al.  
Search for  $K^-pp$  bound state via  $\gamma d \rightarrow K^+\pi^-X$  reaction at  $E_\gamma = 1.5 - 2.4$  GeV.  
*Phys. Lett.*, B728:616–621, 2014.  
(Cited on page 11)
- [THF94] K. Tsushima, S.W. Huang, and Amand Faessler.  
The Role of the  $\Delta(1920)$  resonance for kaon production in heavy ion collisions.  
*Phys. Lett.*, B337:245–253, 1994.  
(Cited on page 17)
- [THF95] K. Tsushima, S.W. Huang, and Amand Faessler.  
Resonance model of  $\pi\Delta \rightarrow YK$  for kaon production in heavy-ion collisions.  
*J. Phys.*, G21:33–42, 1995.  
(Cited on page 17)

- [TST99] Kazuo Tsushima, Alexander Sibirtsev, and Anthony William Thomas. Resonance model study of kaon production in baryon baryon reactions for heavy ion collisions. *Phys. Rev.*, C59:369–387, 1999.  
(Cited on pages 14, 17, 64, 66, 69, 95, 96, 97, and 99)
- [WCSB12] S. Weissenborn, D. Chatterjee, and J. Schaffner-Bielich. Hyperons and massive neutron stars: the role of hyperon potentials. *Nucl. Phys.*, A881:62–77, 2012.  
(Cited on pages 6 and 101)
- [Wik14] Wikipedia. Eightfold way, 2014.  
[http://de.wikipedia.org/wiki/Eightfold\\_Way](http://de.wikipedia.org/wiki/Eightfold_Way); accessed on 11-November-2014.  
(Cited on page 6)
- [WvHM12] Janus Weil, Hendrik van Hees, and Ulrich Mosel. Dilepton production in proton-induced reactions at SIS energies with the GiBUU transport model. *Eur. Phys. J.*, A48:111, 2012.  
(Cited on pages 16, 17, and 62)
- [YA02] T. Yamazaki and Y. Akaishi. ( $K^-, \pi^-$ ) production of nuclear  $\bar{K}$  bound states in proton-rich systems via  $\Lambda^*$  doorways. *Phys. Lett.*, B535:70–76, 2002.  
(Cited on page 11)
- [YMK<sup>+</sup>10] T. Yamazaki, M. Maggiora, P. Kienle, K. Suzuki, A. Amoroso, et al. Indication of a deeply bound compact  $K^-pp$  state formed in the  $pp \rightarrow p\Lambda K^+$  reaction at 2.85 GeV. *Phys. Rev. Lett.*, 104:132502, 2010.  
(Cited on page 11)
- [Zme08] Johann Zmeskal. From kaonic atoms to kaonic nuclei: A search for antikaon-mediated bound nuclear systems. *Prog. Part. Nucl. Phys.*, 61:512–550, 2008.  
(Cited on page 11)

# Danksagung

Während meiner Doktorarbeitszeit konnte ich stets auf ein hilfsbereites, offenes Umfeld zählen und so möchte ich meine abschließenden Worte diesen Personen widmen. Mein herzlicher Dank gilt vor allem Prof. Laura Fabbietti, die mich nach meinem fachfremden Studium (Maschinenwesen) in ihrer Gruppe aufnahm und mir sogar ermöglichte eine Doktorarbeit anzufertigen. Durch sie habe ich nicht nur die physikalischen Zusammenhänge gelernt, sondern auch wie man Vorträge mit einem roten Faden durchzieht und allgemein verständlich aufbereitet. Sie hat mich immer gefördert und unterstützt, sei es indem sie mich auf Konferenzen und Physics Schools schickte oder Treffen mit Fachleuten organisierte. Weiterhin hat sie mir auch ermöglicht, Erfahrung in Sachen Studentenbetreuung zu sammeln. Vielen Dank für dieses Vertrauen! Natürlich gab es auch stressige Zeiten, aber letztendlich war das wichtigste Gefühl, das sie mir vermittelte, dass sie immer hinter mir stand und steht.

Auch die Gruppe spielte eine wichtige Rolle für mich, die nicht nur Kollegen waren, sondern Freunde geworden sind. Dabei gilt ein großer Dank meinem Mentor, Kirill Lapidus, mit dem ich immer über meine Analyse reden konnte und der auch jeden Text, den ich während der Doktorarbeitszeit geschrieben habe, korrigiert hat. Er hat stets (auch ungefragt) mitgedacht und Begeisterung für meine Ergebnisse gezeigt, was mich sehr gefreut hat. Ein offenes Ohr bei physikalischen und analysetechnischen Fragen fand ich auch immer bei meinen ehemaligen Kollegen Dominik Soliman, Johannes Siebenson und Eliane Epple. Ihnen gebürt insbesondere auch ein Dank für die lustige, singende und freudige Zeit. Außerdem bedanke ich mich bei Dominik für sein Mitgefühl, als ich monatelang Spektren gefittet habe. Des Weiteren möchte ich Robert Münzer danken, mit dem ich über alles reden konnte und der mir bei allen möglichen bürokratischen Angelegenheiten weiterhalf. Ebenso danke ich Joana Wirth, meiner Seelenverwandten und treuen Hotelzimmergenossin, für ihren Beistand vor meinen Vorträgen und für ihren hilfsbereiten und lockeren Umgang. Meinem Bürogenossen, Oliver Arnold, danke ich für seine angenehme Gesellschaft und die physikalischen Gespräche und Rafal Lalik für die schöne Zeit in Japan bei der SNP School und bei unseren Erkundungen von Tokyo. Nicht zu vergessen, Verena Walbrecht, mit der ich sehr viel Spaß beim TUMlab hatte und mit der man immer gut lachen, aber auch ernsthafte Gespräche führen kann. Ich habe mich sehr wohl in der Gruppe gefühlt und hoffe, dieser Rückhalt und diese produktive Atmosphäre bleibt auch weiterhin bestehen.

Der allergrößte Dank gilt natürlich meinem Mann, Martin Berger, der eigentlich auch Teil der Gruppe ist. Er hat meine Arbeit exzellent und vor allem kritisch korrigiert. Aber insbesondere war er immer für mich da und hat alle schweren Zeiten abgefedert. Durch sein Verständnis und den Rückhalt, den er mir gab, konnte ich mich voll auf meine Doktorarbeit konzentrieren. Ohne ihn wäre ich nicht soweit gekommen.

Letztendlich möchte ich mich bei meiner Familie bedanken und damit meine auch die Familie von meinem Mann. Bei meinen Eltern und meinem Bruder, Shyh-Horng Chen, wusste ich immer, dass ich auf sie zählen kann und dass sie stolz auf mich sind, egal wie ich mich anstelle, hauptsächlich ich bemühe mich. Und Christine Bradler, meine Schwiegermutter, war auch eine unglaubliche Stütze, nicht nur da sie uns immer lecker Essen gekocht hat, sondern auch seelisch!